Search for Neutrino-Induced Cascades with the AMANDA-II Detector

DISSERTATION

zur Erlangung des akademischen Grades
doctor rerum naturalium
(Dr. rer. nat.)
im Fach Physik

eingereicht an der
Mathematisch-Naturwissenschaftlichen Fakultät I
Humboldt-Universität zu Berlin

von
Dipl.-Phys. Marek Paul Kowalski
geboren am 23.5.1974 in Bonn

Präsident der Humboldt-Universität zu Berlin:
Prof. Dr. Jürgen Mlynek

Dekan der Mathematisch-Naturwissenschaftlichen Fakultät I:
Prof. Dr. Michael Linscheid

Gutachter:

1. Prof. Dr. Thomas Lohse
2. Prof. Dr. Lutz Köpke
3. Prof. Dr. Douglas Cowen

eingereicht am: 15. Oktober 2003
Tag der mündlichen Prüfung: 13. Januar 2004

Zusammenfassung

Diese Arbeit enthält die Ergebnisse der Suche nach Neutrino-induzierten kaskadenartigen Ereignissen mit dem AMANDA-II Detektor. Die Signatur von Elektron- und Tauonneutrinowechselwirkungen sind elektromagnetische sowie hadronische Teilchenschauer, sogenannte Kaskaden. Zusätzlich können Neutrinos aller Arten, die über neutrale Ströme wechselwirken, durch hadronische Kaskaden nachgewiesen werden.

Es wurden Methoden zur Orts- und Energierekonstruktion von Kaskadenereignissen verbessert sowie neuentwickelt. Sowohl Orts- und Energieauflösung konnten mit Hilfe von künstlichen Lichtquellen verifiziert werden. Außerdem wurde ein Neutrinogenerator entwickelt, der es erlaubt bis zu den höchsten Energien Neutrino-induzierte Ereignisse zu simulieren. Ein Filter zur Trennung Neutrino-induzierter Kaskaden vom Untergrund atmosphärischer Myonereignisse wurde entwickelt.

Der erste Datensatz des AMANDA-II Detektors aus dem Jahr 2000 wurde auf die Signatur von hochenergetischen Neutrino-induzierten Kaskaden untersucht. Ein einzelnes Ereignis passierte alle Selektionsschnitte. Diese Beobachtung ist mit der erwarteten Anzahl Ereignisse von $0.96^{+0.70}_{-0.43}$ durch atmosphärische Neutrinos und Myonen verträglich. Es wurden obere Grenzen auf den zusätzlichen Beitrag astrophysikalischer Neutrinos bestimmt. Unter der Annahme eines Neutrinoflußes von $\phi(E) \propto E^{-2}$ kann eine obere Grenze von $E^2\phi(E) = 9 \times 10^{-7}$ GeV s^{-1} sr^{-1} cm^{-2} auf den Fluss von Neutrinos aller Arten angegeben werden (90% CL). Die obere Grenze stellt zur Zeit die restriktivste Einschränkung des Neutrinoflusses in einem Energiebereich von circa 50 TeV bis 5 PeV dar. Einige der untersuchten Modellvorhersagen sind nicht mit der Beobachtung verträglich und können somit ausgeschlossen werden.

Abstract

The first generation of large open water/ice Cherenkov telescopes has recently started operation. The goal of these instruments is the detection of an astrophysical high-energy neutrino flux which, if detected would add crucial information to the puzzle of the origin of the high-energy cosmic rays. AMANDA (Antarctic Muon And Neutrino Detector Array) is located at the geographical South Pole and uses the thick polar ice cap as both detection and target material for the rare neutrino-induced events. Here we present a search for electro-magnetic and/or hadronic showers (cascades) induced by a diffuse flux of high energy neutrinos. Such a signature is characteristic for electron and tau neutrinos, and to a less extend for muon neutrinos.

The first year of data collected with the AMANDA-II detector has been analyzed. The observed event rates are consistent with the expected rate of neutrinos and muons produce by cosmic ray interaction in the Earth atmosphere. Upper limits on a diffuse flux of extraterrestrial electron, tau and muon neutrinos are presented. A flux of neutrinos following an E^{-2} spectrum and consisting of an equal mix of all flavors is limited to $E^2\phi(E) \leq 9 \times 10^{-7}$ GeV s^{-1} sr^{-1} cm^{-2} (at 90 % CL) for a neutrino energy range 50 TeV to 5 PeV. In this energy range the limits are currently the most stringent available and rule out several existing flux predictions for extraterrestrial neutrinos.

Contents

List of Figures

List of Tables

Chapter 1

Introduction

The Nobel Prize for Physics of the year 2002 has been awarded to three pioneers in experimental astroparticle physics: Ray Davis and Masatoshi Koshiba share half the prize for "pioneering contributions to astrophysics, in particular for the detection of cosmic neutrinos". Riccardo Giacconi receives the other half of the prize for contributions which have led to the discovery of cosmic X-ray sources. This reward can be viewed as a landmark in an exciting and successful campaign of gaining new insights into the Universe by exploring new paths.

Within the last few decades photon astronomy extended to new wavelengths, and spectacular discoveries have been made in all wavelength ranging from radio through microwaves up to X-rays and gamma rays. To name a few: we now know about the cosmic microwave background, active galactic nuclei or most intense gamma ray bursts. Nevertheless, important astrophysical questions remain. One of it is the origin of the highest energy cosmic rays, a question which might not be answered conclusively by observation of photons alone. Production of cosmic rays is accompanied both by production of high energy gamma rays and neutrinos. At higher energies, gamma rays are absorbed by the radiation and matter encountered along the path from the sources to the detectors. Hence, the universe is opaque to very high-energy gamma rays. Neutrinos offer an alternative. Interacting only weakly, they escape dense environments and reach the observer unscattered.

So far, low energy MeV neutrino astronomy has been established by the observation of solar neutrinos and neutrinos from the supernova SN1997A. The goal of large scale open Cherenkov telescopes is to extend the window to neutrinos with energies of GeV to PeV. Two of such first generation telescopes, AMANDA [17] and BAIKAL [26], are currently being operated, and further ones are in the development or prototyping stage [122,157,85]. These instruments are commonly optimized for largest sensitivity to neutrino-induced muons with TeV energies. As it turns out, they have large sensitivity in other detection channels as well.

The topic of this dissertation is a search for neutrino-induced electro-magnetic and hadronic showers (cascades) with the AMANDA-II detector. Neutrinos of all flavor contribute to this class of events, hence the analysis extends the sensitivity of the instrument to electron and tau neutrinos.

This work is organized as follows: Chapter 2 briefly summarizes the motivation for the existence of astrophysical high energy neutrinos. The detection principles and specific issues related to simulation of neutrino-induced cascade events are discussed in chapter 3. The AMANDA-II detector is introduced in chapter 4. Existing algorithms for reconstructing vertex position and energy of cascades are reviewed in chapter 5. The experimental and simulated data samples used in the analysis are introduced in chapter 6. Chapter 7 explains the analysis of the first year of data taken with the AMANDA-II detector. The detector efficiency for detecting neutrino-induced events is described in chapter 8. The results of the analysis, which include upper limits on the flux of high energy neutrinos are summarized in chapter 9. The final chapters 10 and 11 are devoted to a summary and an outlook.

Chapter 2

Flux of High Energy Neutrinos

The existence of a flux of high energy neutrinos is motivated by the observation of charged relativistic particles of cosmic origin, so called *cosmic rays*. After briefly reviewing the current knowledge about cosmic rays, the connection between neutrinos and cosmic rays is discussed. Terrestrial and extraterrestrial neutrino flux predictions are reviewed. Emphasis is put on the expected ratio of fluxes of various neutrino flavors.

2.1 High Energy Cosmic Rays

The energies at which cosmic rays have been observed range over more than 10 orders in magnitude, and reach up to extraordinary high energies of 3×10^{20} eV. A large number of experiments have contributed to the available knowledge about the cosmic ray energy spectrum. At energies below 10^{13} eV, the steeply falling flux of cosmic rays is still large enough to be measured by balloon and satellite experiments with high precision. The upper end of the spectrum is measured indirectly by the observation of secondary particle showers, induced through the interactions of cosmic rays with molecules of the atmosphere (for a review see [125]). At the highest energies, the smallness of the flux requires the detectors to cover areas as large as $\gtrsim 100$ km^2.

Figure 2.1.1 shows a compilation of the available data. The spectrum is well described by a broken power-law, $\frac{\mathrm{d}N}{\mathrm{d}E} \propto E^{-\gamma}$, with $\gamma \approx 2.7$ up to energies of $E_{\mathrm{knee}} = 10^{15.5}$ eV. At E_{knee} the slope changes to $\gamma \approx 3.0$, a phenomenom called *spectral knee* (see [74] for a recent evaluation of the available data). At energies of 10^{19} eV, the slope of the spectrum changes back to $\gamma \approx 2.7$. This change in slope is called *spectral ankle*.

An acceleration mechanism which is capable of explaining the observed power-law spectrum is the *Fermi* mechanism [53,54]. In this mechanism charged cosmic rays are elastically scattered on magnetic fields back and forth across a shock front and are thereby accelerated. In the generic case Fermi acceleration yields a spectral index close to 2, however for most realistic calculations the resulting spectrum is steeper, with $\gamma = 2.1 - 2.4$ [110, 58]. The observed spectrum, due to propagation effects, will be steeper than that at the source [119, 66]. The average time that cosmic rays are confined to our galaxy decreases with energy, leading to a reduction of the local flux of energetic cosmic rays.

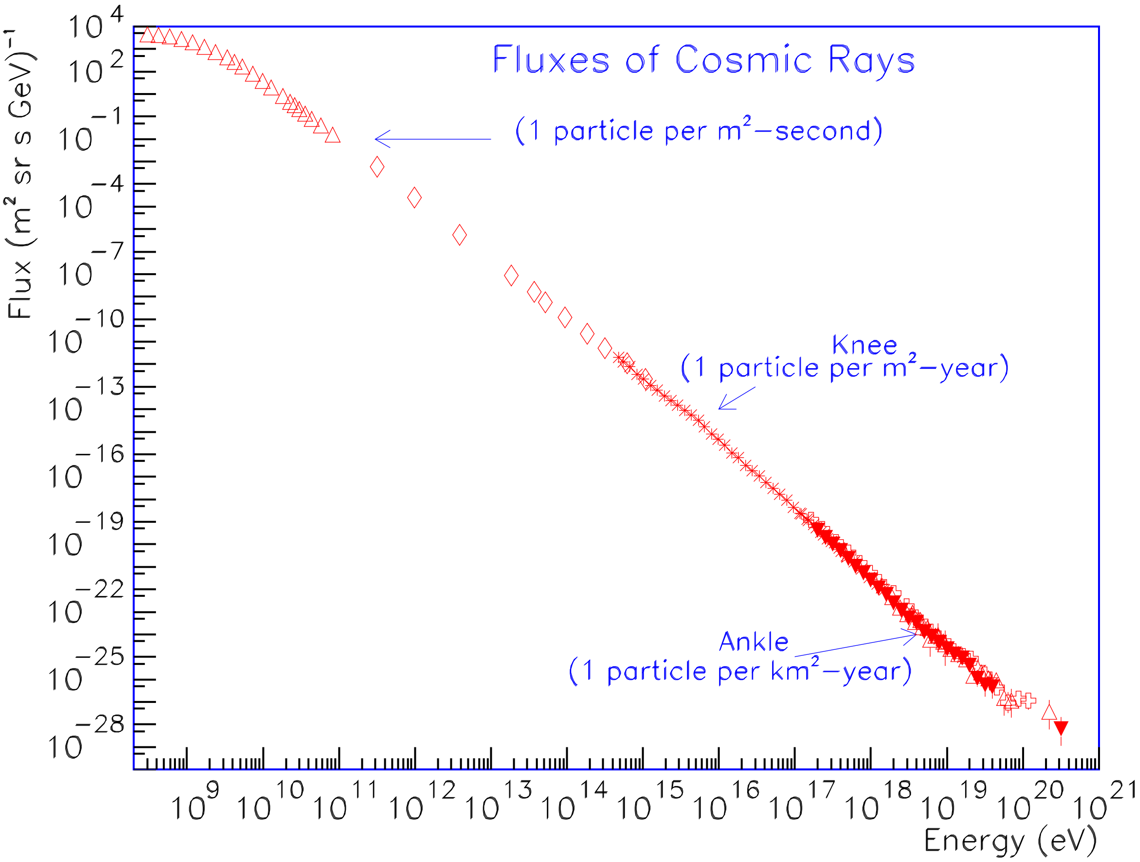

Figure 2.1.1: Observed energy spectrum of cosmic rays (figure adopted from [158]). The spectrum can be represented by a power law with a change of slopes at energies corresponding to the *knee* and *ankle*.

There is evidence that galactic supernova remnants are responsible for acceleration of cosmic rays in the energy region of the knee [46, 153]. However, due to their limited size they have reduced efficiency for acceleration of cosmic rays above E_{knee}. The change in slope of the spectrum around 10^{19} eV is generally attributed to the transition of dominating cosmic ray sources, namely from galactic to extragalactic ones.

The existence of cosmic rays at energies $\gtrsim 10^{20}$ eV is remarkable for a number of reasons. General arguments show that any astrophysical sources capable of accelerating particles (e.g. protons) to such high energies must store extraordinary large amounts of energy in the form of magnetic fields [37]. Moreover these sources should be relatively close by, as protons interact through photo-pion production with the microwave background during propagation from the source to the observer. For a cosmic distribution of sources one expects a cutoff in the spectrum at about 6×10^{19} eV. This effect was predicted by Greisen [71], Zatsepin and Kuz'min [178] and has become known as the GZK cut-off. In particular the absence of this cut-off would have important implications for the potential sources of highest energies. It is still an open and much debated question, whether the GZK cutoff has already been discovered [25].

There is a number of potential sources for the highest energy cosmic rays. The large class of the so called *bottom-up* models assume cosmic rays to be accelerated. Possible extragalactic acceleration sites are Active Galactic Nuclei (see section 2.4.1) and Gamma Ray Bursts (see section 2.4.2). The maximum energy reached by bottom-up accelerators depends on the size of the object as well as its magnetic field strength. For known extragalactic sources an optimistic upper bound is $E_{\mathrm{max}} \sim 10^{21}$ eV [143].

The other class of models are the *top-down* models, where cosmic rays result from the decay of super-heavy particles (for a review see [143, 32]). These models have the advantage of explaining cosmic rays with energies well above 10^{21} eV. However, *top-down* models are more speculative than *bottom-up* models, since they require the presence of new and very heavy particles ($M_X \gg 10^{21}$ eV). There are a number of generation mechanisms imaginable. One of the scenarios assumes, that super-heavy particles are more or less continously released from Topological Defects (TDs), which would be topologically stable configurations of space left over from Grand Unified Theory (GUT) symmetry breaking phase transition of the early universe [31]. In most models, the cosmic ray spectrum at the highest energies is assumed to emerge from the decay or annihilation of these particles.

Charged cosmic rays are deflected by the galactic and intergalactic magnetic fields, so they do not reveal the position of their sources. This missing information is the driving argument for the desire to detect a corresponding neutrino signal. As will be discussed in the next section, neutrinos, for which the arrival directions point back to the sources, are tightly connected with the production of the highest energy cosmic rays.

2.2 Neutrino Production

Most models for cosmic ray accelerators predict a significant flux of high energy neutrinos, because a fraction of the cosmic rays will interact at the acceleration site with either ambient matter or photon fields.

In this picture, neutrinos are generated in the so called *beam dump* scenario, where energetic cosmic rays interact with target matter or photons within the source, to produce among the resulting particles short lived mesons:

$$\begin{aligned}
p + X &\rightarrow \pi^{\pm} + Y \\
&\qquad \hookrightarrow \mu^{\pm} + \nu_\mu(\bar{\nu}_\mu) \\
&\qquad\qquad \hookrightarrow e^{\pm} + \nu_e(\bar{\nu}_e) + \bar{\nu}_\mu(\nu_\mu) \\
p + X &\rightarrow K^{\pm} + Y \\
&\qquad \hookrightarrow \mu^{\pm} + \nu_\mu(\bar{\nu}_\mu) \\
&\qquad\qquad \hookrightarrow e^{\pm} + \nu_e(\bar{\nu}_e) + \bar{\nu}_\mu(\nu_\mu) \\
p + \gamma &\rightarrow \pi^{+} + n \\
&\qquad \hookrightarrow \mu^{+} + \nu_\mu \\
&\qquad\qquad \hookrightarrow e^{+} + \nu_e + \bar{\nu}_\mu
\end{aligned} \tag{2.2.1}$$

Within the source, the target material can consist of an UV or X-ray photon field (e.g. from synchrotron radiation of electrons) or a gas of hadrons.

Among the emerging mesons mainly pions and to a lesser extent kaons are created. It is the decay of charged pions and kaons which leads to the flux of neutrinos. The neutral pions decay electromagnetically into two γ quanta, and therefore contribute to the high energy γ spectrum from the source. This qualifies the emitters of high energy γ rays as potential sources of high energy neutrinos.

2.3 The Ratio of Neutrino Flavors

The expected flux ratio for different neutrino flavors is tightly related to the mechanism of production and propagation of neutrinos. While the absolute flux depends on many largely unknown properties of their sources, the ratio of the expected neutrino flavors can be predicted with only small uncertainties. The presence of neutrino oscillations will modify the expected flavor ratio during the propagation from the point of origin to the location of the detector. Effects expected from neutrino oscillations are discussed in section 2.3.2. Consequences of more exotic phenomena, such as neutrino decay and WIMP annihilation are discussed in sections 2.3.3 and 2.3.4.

2.3.1 The Ratio at the Astrophysical Neutrino Source

In the following, the standard astrophysical beam dump scenario is considered. The main interaction and decay chains were schematically displayed in equation 2.2.1. One assumes that the interaction length for the mesons and muons are significantly larger than their decay length. By counting the number of emerging neutrinos, one finds a ratio of $N_{\nu_e} : N_{\nu_\mu} : N_{\nu_\tau} = 1 : 2 : 0$. However, in order to get the ratio of neutrino flavors for a specified energy, i.e. the ratio of the neutrino fluxes ($\phi = \frac{\mathrm{d}N}{\mathrm{d}E}$), one also needs to include the kinematics of the decays as well as the flux of the parent particles. As will be explained below, it is a remarkable coincidence that the ratio of neutrino flavors at all energies does not change much from $\phi_{\nu_e} : \phi_{\nu_\mu} : \phi_{\nu_\tau} = 1 : 2 : 0$ for a large range of different parent flux spectra.

In a first step we focus on the production rate of mesons from the interaction of high energy primary particles with ambient protons and photons. Throughout this section a power law spectrum for the differential flux of primary nuclei (N) is assumed: $\phi_{\mathrm{N}}^{\gamma}(E_{\mathrm{N}}) \propto E_{\mathrm{N}}^{-\gamma}$. Further, the absence of scaling violations of the inclusive cross-sections for production of mesons of type j $(= \pi, K)$ is assumed, namely that $\frac{\mathrm{d}n_j(E_{\mathrm{N}},E_j)}{\mathrm{d}E_j} \approx \frac{\mathrm{d}n_j(y)}{\mathrm{d}y}\frac{1}{E_{\mathrm{N}}}$ with $y = E_j/E_{\mathrm{N}}$. It follows, that the flux of mesons[1] is a constant fraction of the flux of primary particles:

$$\phi_j(E) = \phi_{\mathrm{N}}(E) Z_{\mathrm{N}j}^{\gamma}.$$

Note that the constant $Z_{\mathrm{N}j}^{\gamma}$ has a spectral slope dependency. For pion production one gets $Z_{\mathrm{N}\pi}^{\gamma} \approx 0.3(0.04)$ for $\gamma = 2(3)$ [58]. For kaon production, Z_{NK} is only about 10-15 % of $Z_{\mathrm{N}\pi}$.

---

[1] The flux of mesons is defined as if mesons where stable.

The flux of neutrinos of flavor α is then obtained by folding the flux spectrum of parent mesons with their decay spectrum:

$$\begin{aligned}\phi_\alpha(E_\nu) = \quad & \sum_{j=\pi,K} \int_{E_\nu}^{\infty} \mathrm{d}E_j\ \phi_j(E_j) \frac{\mathrm{d}n_{j\alpha}(E_j, E_\nu)}{\mathrm{d}E_\nu} \\ & + \int_{E_\nu}^{\infty} \mathrm{d}E_j \int_{E_\mathrm{min}}^{E_j} \mathrm{d}E_\mu\ \phi_j(E_j) \frac{\mathrm{d}n_{j\mu}(E_j, E_\mu)}{\mathrm{d}E_\mu} \frac{\mathrm{d}n_{\mu\alpha}(E_\mu, E_\nu)}{\mathrm{d}E_\nu}\end{aligned} \tag{2.3.1}$$

with

$$E_\mathrm{min} = \min(r_j E_j, E_\nu);\ r_j = (m_\mu/m_j)^2.$$

Here, $\frac{\mathrm{d}n_{j\alpha}(E_j,E_\nu)}{\mathrm{d}E_\nu}$ represents the decay spectrum from a parent meson of type j and energy E_j into a neutrino of type α ($=\nu_e, \nu_\mu$) and energy E_ν. If α is replaced by μ it represents the decay spectrum of the meson into a muon instead of a neutrino. Finally $\frac{\mathrm{d}n_{\mu\alpha}(E_\mu,E_\nu)}{\mathrm{d}E_\nu}$ represents the decay spectrum from a muon into a neutrino of type α.

The first term in the sum represents the direct two body decay, e.g. $\pi \to \nu$ while the second term represents the decay through an intermediate muon, $\pi \to \mu \to \nu$. The first part of the sum in (2.3.1) can easily be evaluated, since the 2-body decay spectrum for relativistic mesons is constant between the kinematic boundaries, $(1 - r_j) \cdot E_j > E_\nu > 0$. The full solution to the integrals in equations (2.3.1) for an energy spectrum following a power law, $E^{-\gamma}$, can be found in [58]. Note that the muon neutrino from the charged pion decay carries away on average nearly 1/4 of the pion energy (since $r_\pi = 0.57$), while the three particles from the decay of the muon share on average about 3/4 of the pion energy. Thus in a first approximation, all neutrinos from the decay of the pion and subsequent decay of the muon have a similar energy spectrum and contribute equally to the total flux of neutrinos. In case of decaying kaons, because of the small r_K, the directly emerging neutrino carries away on average nearly half of the energy. For a steeply falling spectrum, it therefore contributes the larger fraction to the overall neutrino flux. Figure 2.3.1 shows the ratio of electron and muon neutrinos as a function of the slope of the neutrino spectrum, γ, for a pure $\pi^\pm$ and $K^\pm$ primary flux as well as for a realistic composition of pions and kaons ($Z^\gamma_\mathrm{NK}/Z^\gamma_\mathrm{N\pi} \approx 11$ %). Indeed, the approximation $\phi_{\nu_e} : \phi_{\nu_\mu} : \phi_{\nu_\tau} \approx 1 : 2 : 0$ is valid over a large range of spectral slopes.

2.3.2 Neutrino Oscillations

The possibility of neutrino oscillations has been discussed for the first time as early as 1957 [132] and was used as an explanation of the solar neutrino deficit [72]. However because of a lack of further experimental evidence the hypothesis of neutrino oscillations could not be confirmed for a long time.

By now, the interpretation of atmospheric and solar neutrino data from the Super-Kamiokande and SNO experiments clearly favors the neutrino flavor oscillation hypothesis [56,5]. The most favored solutions of neutrino oscillation parameters recently obtained confirmation from experiments with "laboratory"neutrino sources. The Kamland experiment detected anti-electron neutrinos, which where generated by nuclear-reactors. The observed rate of neutrinos is consistent with the oscillation parameters obtained from the

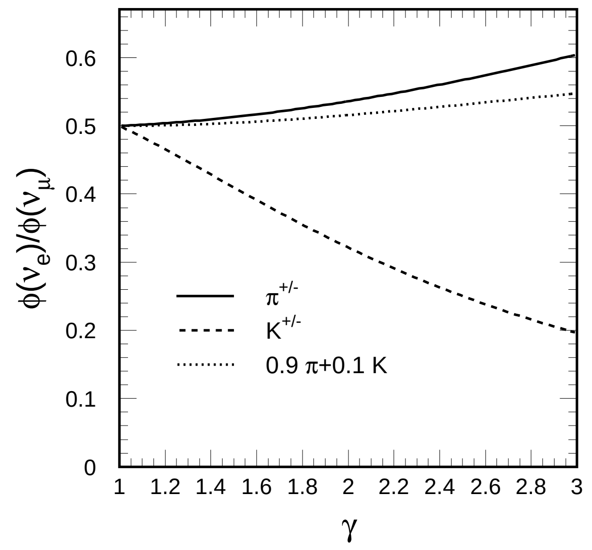

Figure 2.3.1: The ratio of electron- to muon-neutrino flux, $\phi(\nu_e)/\phi(\nu_\mu)$, as a function of the spectral slope of the primary flux of protons, γ ($\phi \propto E^{-\gamma}$). The ratio is shown for individual contributions from pions and kaons as well as for a realistic composition.

solar neutrino data [48]. Similarly, the K2K experiment has observed a reduced rate of muon neutrinos from a neutrino beam generated at a distance of 250 km, confirming the conclusions drawn from atmospheric neutrino data [6].

Neutrino oscillations are a consequence of the flavor eigenstates being different from the mass eigenstates. In the case of three neutrinos[2], the flavor eigenstates and the mass eigenstates are related by the unitary MNS (Maki-Nakagawa-Sakata) matrix:

$$U_{\mathrm{MNS}} = \begin{pmatrix} U_{e1} & U_{e2} & U_{e3} \\ U_{\mu 1} & U_{\mu 2} & U_{\mu 3} \\ U_{\tau 1} & U_{\tau 2} & U_{\tau 3} \end{pmatrix}. \tag{2.3.2}$$

Only some of the entries of the MNS matrix are currently constrained and important properties of the mixing matrix, as for example those possibly responsible for CP violation in the lepton sector, are yet unrevealed. A full review of the existing constraints and their significance is beyond the scope of this work. The interested reader is referred to the many existing review articles [51, 23].

Here, we focus on the impact of neutrino mixing on the observable flux of neutrinos from astronomical distance. If the neutrino sources are sufficiently separated or extended the distance-dependent oscillation amplitudes average out. The observable flux of neutrinos of flavor α is then obtained from the flux at the source, $\phi_\nu^{\mathrm{source}}$, by:

$$\phi_{\nu_\alpha} = \sum_\beta \sum_i |U_{\beta i}|^2 |U_{\alpha i}|^2 \phi_{\nu_\beta}^{\mathrm{source}}. \tag{2.3.3}$$

---

[2] Here, the case of additional sterile neutrino flavors is not discussed. More than 3 neutrino flavors are necessary to consistently explain the observations of the LSND experiment [21] which however was not yet confirmed by other experiments.

From the atmospheric neutrino data one can conclude that $U_{\mu 3} \approx U_{\tau 3}$ [56]. It can be shown that by combining this information with the result from the CHOOZ reactor experiment [18], $U_{e3} < 0.2$, a flavor ratio of $\phi_{\nu_e} : \phi_{\nu_\mu} : \phi_{\nu_\tau} \approx 1 : 2 : 0$ becomes $1 : 1 : 1$ at the detector site [22], i.e. the observable flux of neutrinos becomes comparable for all flavors.

2.3.3 Neutrino Decay

In case of unstable neutrinos, with non-radiative decay of one neutrino into another and a mass-less particle (e.g. a majoron), one expects a considerable change in the ratio of flavors [27,51]. For illustration, we assume that only the lightest neutrino mass eigenstate, ν_1, is stable and that neutrinos generated in the decay contribute negligibly to the final flux. The flux reaching the Earth is then given by the projection: $\phi_{\nu_\alpha} = \sum_\beta \phi_\beta^{\mathrm{source}} |U_{\alpha 1}|^2 |U_{\beta 1}|^2$. The observable flavor ratio at the Earth becomes $|U_{e1}|^2 : |U_{\mu 1}|^2 : |U_{\tau 1}|^2 \approx 6 : 1 : 1$ for a range of realistic mixing parameters [27]. Note that in case of inverted hierarchy, namely that the lightest neutrino mass eigenstate is ν_3, one typically expects a ratio close to $0 : 1 : 1$.

2.3.4 Other Exotic Phenomena

The ratio of neutrino flavors can deviate from the cases discussed above. Possible causes would typically be connected with particle physics extending beyond the standard model. An example for this are neutrinos from WIMP[3] annihilation. The primary WIMP dark matter candidate might be the lightest stable supersymmetric particle, i.e. the neutralino. Neutralinos would be trapped by the Earth and Sun as well as other massive objects through gravitational interaction. A flux of neutrinos from neutralino annihilation in the center of the Earth and Sun would emerge through decay of the annihilation products consisting of heavy leptons, quarks and gauge-bosons [60,92]. The neutrino flavor composition of the emerging flux is intimately connected with the properties of the neutralino itself. It was shown in [102] that for neutralino annihilation into taus one expects a ratio of fluxes for $\phi_{\nu_e} : \phi_{\nu_\mu} : \phi_{\nu_\tau} \approx 1 : 1 : 5$. Such a scenario is realized for Higgsino-like neutralinos with a mass smaller than the mass of the top-quark.

2.4 Sources of Neutrinos

This section summarizes various expected and known sources of high energy neutrinos. A brief review of the main candidates of astrophysical source is followed by a discussion of atmospheric neutrinos. The flux predictions are summarized in section 2.4.4.

2.4.1 Active Galactic Nuclei

Active Galactic Nuclei (AGN) are very bright centers of galaxies, having a bolometric luminosity comparable to that of entire galaxies. AGNs emit photons at all frequencies, ranging from radio waves to TeV gamma rays. The emitting region must be very compact,

---

[3] WIMP: Weakly Interacting Massive Particle

to allow for the observed strong luminosity variations on time scales of days, hours and less [4].

The general belief is that an AGN consists of a super-massive black hole at its center ($M \sim 10^8 M_\odot$) surrounded by an accretion disc. The energy needed to account for the large observed bolometric luminosity is obtained from matter of the accretion disc, spiraling into the black hole. Most of the energy is released through jets, pointing away from the core and parallel to the rotation axis of the AGN system. The appearance of an AGN changes significantly, depending on the angle of the jet relative to the line of sight as well as on the distance [31, 159]. The highest energy neutrinos and gammas are expected for an observer located along the direction of the jet. AGNs with jets pointing towards the Earth are called *Blazars.* Two rather close-by Blazars are Mrk 421 and Mrk 501. For these AGNs, gammas of up to 20 TeV have been observed [136, 107, 99]. Typically high energy gammas and possibly hadrons and neutrinos are believed to originate from relativistic regions within the jet. So-called *leptonic* or *hadronic* models are proposed to explain the observed electromagnetic spectrum of AGNs. In the leptonic models, low energy synchrotron radiation from electrons is up-scattered to higher energies through the inverse Compton effect (see for example [88]). While such models can explain the high energy component of the observed electromagnetic spectrum, they can not answer the question of the origin of the cosmic ray spectrum. This is different for hadronic models, where the high energy part of the spectrum stems from accelerated hadrons (e.g. protons) [115]. To accelerate protons to high energies strong magnetic fields are required in the source. High energy gammas and neutrinos are produced through photo-pion production. Such a pure *hadronic* model has difficulties explaining the time correlations observed in multi-wavelength observations of some TeV Blazars [141].

A recently proposed model for AGNs assumes a mixture of a proton synchrotron radiation and photo-pion production, to explain the energy spectrum of electromagnetic radiation of a large number of AGNs [124].

2.4.2 Gamma Ray Bursts

Gamma Ray Bursts (GRBs) are extremely bright sources of light, emitting gamma rays mainly during a short time-window. An average GRB lasts for about 0.1-10 s. During this time span, GRBs are the brightest sources in the Universe. GRBs are detected with an isotropic distribution in the sky, a fact indicating their extragalactic origin [131]. A likely cause for GRBs are radiating ultra-relativistic electrons and protons which have been accelerated in a relativistic expanding fireball [120]. The source for such a fireball has not yet been resolved. However, for a few GRBs, a connection with an underlying supernova explosion was established.

Because GRBs radiate hard gamma rays, they are good candidates for high energy neutrino sources. Based on the relativistic fireball model, an estimate of the total neutrino flux of all GRBs has been performed [164] which can be detected by large neutrino telescopes of km^3 size. Additionally, burst-to-burst fluctuations can lead to large fluxes of neutrinos from individual close-by GRBs [10, 73].

2.4.3 Atmospheric Neutrinos

The so called *atmospheric* neutrinos are of particular importance, as they constitute the only class of neutrinos which has been detected by high energy neutrino telescopes so far. Atmospheric neutrinos are generated through interaction of cosmic ray hadrons with molecules in the atmosphere. In fact, the flux of atmospheric neutrinos can be predicted with such accuracy, that their detection provides a tool to verify and possibly calibrate the performance of the detector. Hence, the observation of atmospheric neutrinos was the topic of one of the first AMANDA publications [7].

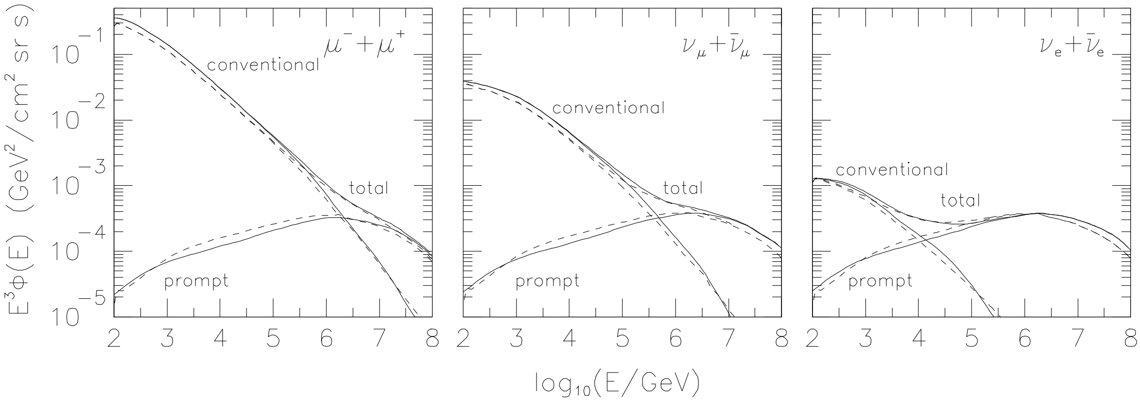

Figure 2.4.1: Shown is the flux of muons, muon neutrinos and electron neutrinos, weighted with E^3, due to cosmic ray interaction in the Earth's atmosphere (figure taken from [69]). The conventional component from π and K decays and the prompt component from charmed meson decay is shown separately. The full line is a detailed simulation, while the dashed line corresponds to an analytic calculation.

The production of atmospheric neutrinos is related to the beam dump scenario discussed in section 2.2. The crucial difference is that the density of matter in the atmosphere is significantly larger than in typical astrophysical environments of interest. High energy mesons produced in the atmosphere are more likely to interact than to decay, resulting in large air showers. Neutrinos are produced through decay of mesons and muons. For increasing energies, the decay probability is reduced due to the relativistic time dilatation of the decay time. For meson energies $\gtrsim 100$ GeV, the energy dependent reduction of the decay probability leads to a steepening of the spectrum of emerging neutrinos by one power compared to the primary spectrum of cosmic ray hadrons: $\mathrm{d}N_\nu/\mathrm{d}E_\nu \sim E^{-3.7}$. The main contribution to the flux of atmospheric neutrinos is from π and K meson decay. The flux of electron neutrinos is suppressed by more than one order of magnitude compared to that of muon neutrinos, due to the fact that electron neutrinos are nearly exclusively produced through the decay of K_L^0 mesons. Various calculations of this flux of atmospheric neutrinos from π and K decay have been performed [113, 3, 126]. Semi-analytic calculations agree with full Monte Carlo simulations within the expected uncertainties given by the different assumptions for the primary flux and the cross-sections for π and K production. Gaisser and Honda [59] have recently evaluated the uncertainties to 10-20 %, depending on the neutrino energy.

The spectrum of atmospheric neutrinos flattens again, once the contribution from charmed particles becomes large enough. Charmed particles have only a short lifetime and hence mostly decay instead of interacting. Therefore this contribution is often called *prompt charm* flux. The spectral form of the emerging neutrinos follows that of the primary cosmic rays (at slightly higher energies), and hence starts to dominate the softer *conventional* atmospheric neutrino flux from π and K decay at a certain *crossing* energy. This energy is not well known, since the uncertainties in the cross-sections for charm production are rather large. Various groups have calculated the flux due to charmed meson decay and the predictions range over more than one order of magnitude [36, 161, 69] (for a review of the various calculations, see [42]).

The flux of leptons produced in the atmosphere is shown in figure 2.4.1 for muon, muon-neutrinos and electron-neutrinos separately [69]. The conventional flux as well as one model for prompt charm production are shown. The predicted flux from prompt charm is based on a perturbative QCD calculation [69], and represents one of the lowest existing flux prediction.

2.4.4 Predictions for the Diffuse Flux of Neutrinos

One speaks of a diffuse flux of neutrinos, if the directions of the sources generating the flux are not resolvable. This can either be due to a limited resolution of the detector, or due to an isotropic distribution of sources in the sky.

A large number of predictions for the diffuse flux from astrophysical sources exist. A review of these can be found in [110]. Here, we restrict the discussion to generic upper bounds, which are applicable to a large range of sources. A model for neutrino production should be consistent with observed diffuse fluxes of gamma rays and cosmic rays. The diffuse flux of gamma rays above an energy of 30 MeV, as measured with the EGRET satellite, follows [147]:

$$\phi_\gamma(E) = (1.37 \pm 0.06) \times 10^{-6} E^{-2.1\pm0.03}\ \mathrm{GeV}^{-1}\mathrm{cm}^{-2}\mathrm{s}^{-1}\mathrm{sr}^{-1}. \tag{2.4.1}$$

Above energies of about 100 GeV the spectral flux becomes rather uncertain. However, its bolometric intensity is restricted by observations, since most higher energy gammas cascade electro-magnetically through interactions with the intergalactic infra-red photon background into the energy band between 1 MeV and 100 GeV. In order to derive an upper bound for the total luminosity of the neutrino flux, one assumes that the flux of gamma rays is due to $p\gamma \rightarrow p\pi^0 \rightarrow p\gamma\gamma$. This process is accompanied by π^+ production which leads to a flux of neutrinos. The total bolometric luminosity of neutrinos is related to that of gamma rays by:

$$\int E_\gamma \phi_\gamma \mathrm{d}E_\gamma \approx K \int E_\nu \phi_{\nu_\mu} \mathrm{d}E_{\nu_\mu} \tag{2.4.2}$$

with $K \approx 1-2$ being a factor incorporating the kinematics of the decay as well as properties of the spectrum of primary protons and target photons [137]. A similar range for K is obtained for proton-nucleon interaction [58]. Models for which neutrinos originate from a beam dump scenario should at most predict neutrino bolometric luminosities corresponding to equation (2.4.2) where one chooses K=1 according to the logic of an upper bound.

Tighter bounds on the neutrino flux can be derived, if one assumes that the sources are transparent to neutrons produced in the astrophysical beam dump. If neutrons would escape the source they eventually decay into protons which are then observed as cosmic rays. Interpreting the highest energy cosmic rays as originating from extra-galactic sources adds constraints to the flux of neutrinos from neutron transparent sources [165, 117].

Figure 2.4.2 shows a compilation of various known and hypothetical fluxes of muon neutrinos. It shows the predictions for muon neutrinos only, without taking into account effects due to neutrino oscillations, which where discussed in section 2.3.

The shaded area named *atmospheric* represents the flux of atmospheric neutrinos. The lower boundary is given by neutrinos from a vertical direction and the higher boundary by neutrinos coming from horizontal directions [69]. The shaded area named *galactic* represents the flux generated by cosmic rays interacting in our galaxy. The upper boundary is valid for neutrinos from the galactic center, while the lower boundary is given by neutrinos from the edges of the galactic disk [87].

Another relatively solid prediction is the flux of so called *cosmogenic* neutrinos. This flux of neutrinos is produced during propagation of the highest energy cosmic rays. As described in section 2.1, protons interact with the cosmic microwave background through photo-pion production leading to the GZK effect. Neutrino fluxes from the subsequent pion decay have first been considered in [30], and since then calculated again by a number of groups leading to consistent results [175, 135, 49].

The lines marked as upper bounds correspond to calculations for sources from which neutrons will not escape without previous interactions (optical depth: $\tau \gg 1$) [117, 29] and sources from which neutrons can escape freely ($\tau < 1$) [165, 117]. Examples for models of specific sources are also shown. The AGN core model [148] predicts cosmic ray acceleration and neutrino production in the core of AGNs. Also shown is a model for the maximum expected flux of neutrinos produced within AGN jets [117]. Finally a prediction for Gamma Ray Bursts as source of high energy neutrinos is shown [164].

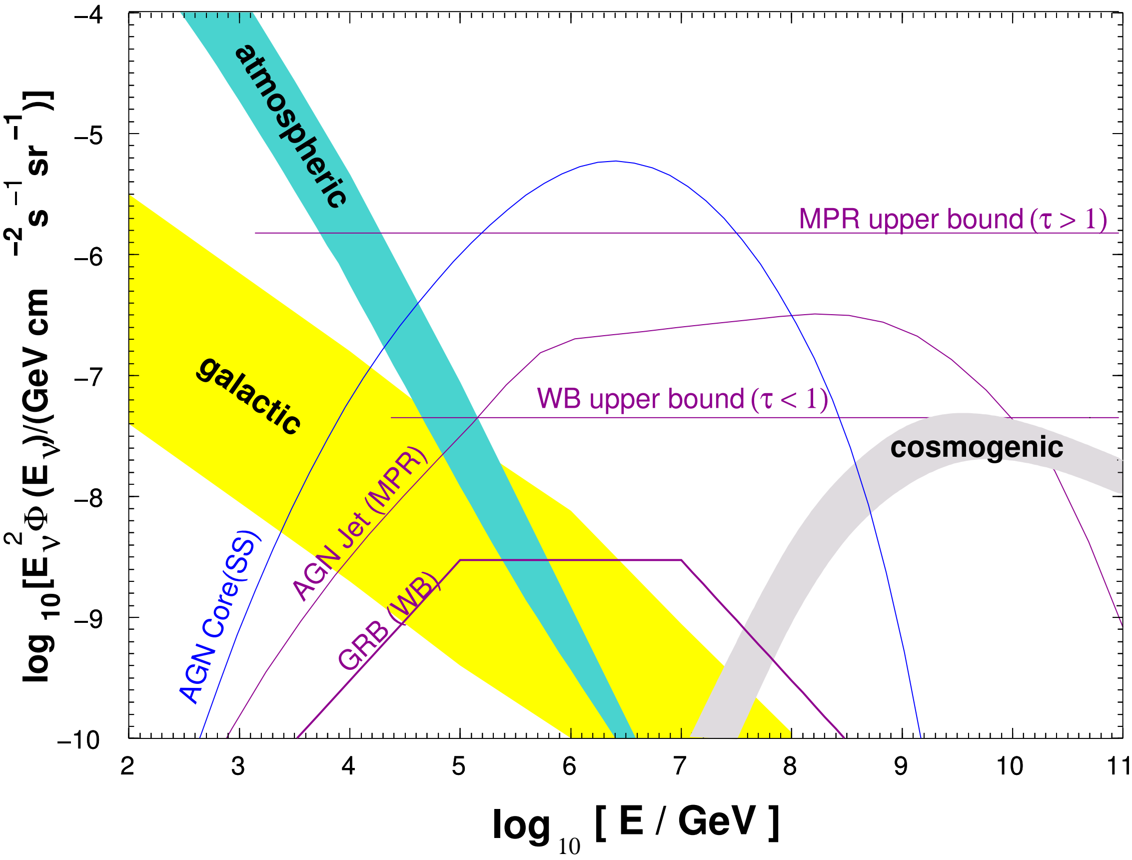

Figure 2.4.2: Summary of expected diffuse $\nu_\mu + \bar{\nu}_\mu$ fluxes. The lines marked as upper bounds correspond to calculations for sources which are optically thick [117] and optically thin sources [165] w.r.t. neutrons. The model labeled "AGN Core (SS)"predicts cosmic ray acceleration and neutrino production in the core of AGNs [148]. Also shown is a model ("AGN Jet (MPR)") for the maximum expected flux of neutrinos produced within jets of AGNs [117]. "GRB (WB)"is a prediction for Gamma Ray Bursts [164]. The atmospheric, galactic [87] and cosmogenic [49] neutrino fluxes are represented by the shaded areas and are further explained in the text. (Plot adapted from [110].)

Chapter 3

Neutrino Detection

High-energy neutrinos are detected by open water or ice Cherenkov telescopes through observation of Cherenkov light from charged particles produced in the interaction of the neutrino with the target material. Since neutrinos interact only through the weak force very large detection volumes are needed. For this reason one uses naturally available ice or ocean and lake water as target and detector medium. In this chapter, the basic ingredients for neutrino detection are reviewed.

3.1 Cross-Sections for Neutrino Reactions

3.1.1 Standard Model

Within the Standard Model of particle physics (SM), neutrinos interact only through the exchange of the Z and W-boson. Charged current (CC) and neutral current (NC) deep inelastic neutrino-nucleon reactions are of main importance:

$$\begin{array}{ll} \nu_l + N \to l + X & \text{(CC)} \\ \nu_l + N \to \nu_l + X & \text{(NC)} \end{array} \tag{3.1.1}$$

where l represents the lepton flavor $l = e, \mu, \tau$ and X the hadronic final state.

For neutrino interaction with an isoscalar nucleon, the CC differential cross-section can be written as [61]:

$$\frac{\mathrm{d}^2\sigma^{\mathrm{cc}}}{\mathrm{d}x\mathrm{d}y} = \frac{2G_F^2 M_N E_\nu}{\pi}\left(\frac{M_W^2}{Q^2+M_W^2}\right)^2\left[xq(x,Q^2) + x\overline{q}(x,Q^2)(1-y)^2\right], \tag{3.1.2}$$

where $-Q^2$ is the invariant square of the momentum transfer from the neutrino to the outgoing lepton, q and $\overline{q}$ are linear combinations of the quark and antiquark parton density functions of the nucleon, M_N and M_W are the mass of the nucleon and of the W-boson and G_F is the Fermi constant. Further, the variables x (the so called Bjorken x) and y are given by:

$$x = \frac{Q^2}{2M_N(E_\nu - E_l)} \qquad \text{and} \qquad y = 1 - \frac{E_l}{E_\nu}, \tag{3.1.3}$$

where E_ν and E_l are the energies of the incoming neutrino and outgoing lepton in the laboratory system.

The formula for the NC cross-section has the same form as (3.1.2), however with the replacement: $M_W \leftrightarrow M_Z$ and another linear combination of the parton density functions.

CC and NC cross-sections are displayed in figure 3.1.1 as a function of neutrino energy. The rise in cross-section is linear up to energies of a few TeV. Above that energy, the propagator term of (3.1.2) severely suppresses a large fraction of the kinematically allowed range of Q^2 and hence leads to a reduced growth of the total cross-section. At high energies the low x behavior of the parton density functions becomes important. For neutrino-nucleon scattering at PeV energies, the relevant parton density functions have not been measured. Instead, the parton density functions are often extrapolated to low x and large Q by power-laws [61, 62]. Alternatively, other extrapolation schemes exist [64, 108]. A prediction for *hard pomeron* enhancement [63] is included in figure 3.1.1. The variations of the total cross-sections due to this extrapolation at 10^9 GeV energies are only a few percent but become uncertain within a factor of 2 at about 10^{12} GeV.

Due to the small mass of the electron, $M_e \ll M_N$, practically all νe^--cross-sections are negligible at high-energies, with the only exception of resonant $\bar{\nu}_e e^-$ scattering at energies $E_{\bar{\nu}_e} \approx M_W^2/2M_e = 6.3$ PeV [67]. The total cross-section for this so called *Glashow* resonance is given by:

$$\sigma \approx \frac{2G_F^2 M_e E_\nu}{(M_W^2 - 2M_e E_\nu)^2 + \Gamma_W^2} \frac{\Gamma(W \to anything)}{\Gamma(W \to e\overline{\nu}_e)}. \tag{3.1.4}$$

Here, $\Gamma_W = 2.12$ GeV [130] is the width of the W-boson and $\Gamma(W \to i)$ is the inclusive decay width into the final state i. At the resonant energy, the cross-section for W production is about 300 times larger than that for CC neutrino-nucleon reactions. This process is dominant for energies of about 3 to 10 PeV.

3.1.2 Beyond the Standard Model

It has been recognized for a long time, that an existing flux of very high energy neutrinos would allow to search for processes, which have not been observed by laboratory experiments. An early example is the Glashow resonance, which was proposed in 1960 [67], as a mean to detect and study the W-boson.

The general argument for using neutrino interactions for the search for new physics is that the known SM reactions, due to their small cross-sections, provide only a small background. Additionally, the available energy in the center of mass system (CMS) of the colliding neutrino and nucleon can significantly exceed the available energies of existing and planned particle colliders. For example CMS energies around one TeV, as proposed for the next generation linear colliders, are reached in neutrino-nucleon reactions with $E_\nu \sim$ PeV. At these energies (and above), the flux of neutrinos is still quite uncertain. However, a lower bound is given by the flux of atmospheric neutrinos for lower neutrino energies, and the flux of GZK neutrinos for higher energies (see section 2.4.4).

A full review of possible effects due to new physics is beyond the scope of this work, and hence we list only a few ideas. Possible effects going beyond the SM include sphaleron and leptoquark production [123], as well as resonant isotriplet scalar production [33].

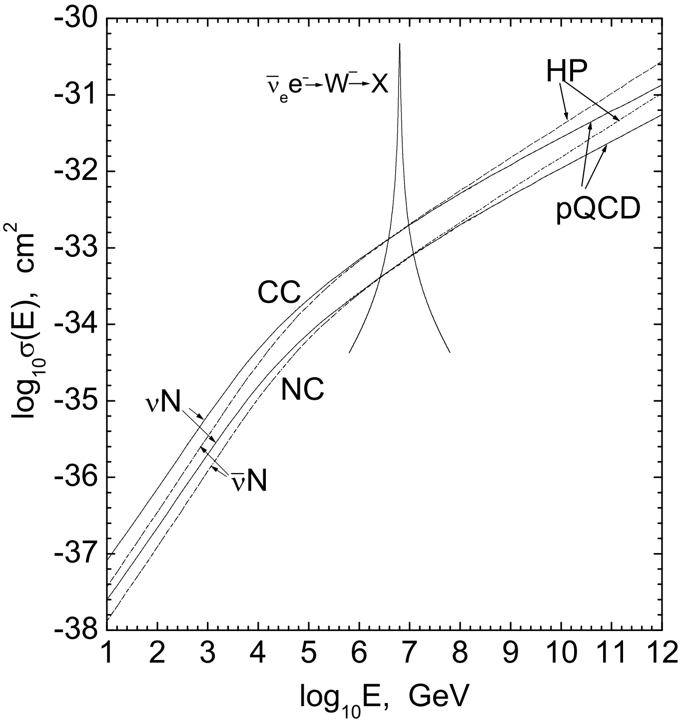

Figure 3.1.1: Standard Model neutrino cross-sections as a function of the neutrino energy. Cross-sections for neutrino nucleon interactions are shown for a smooth power-law extrapolation in x and Q^2 (pQCD) as well as *hard pomeron* enhanced extrapolations (HP) [63]. Also shown is the cross-section for resonant $\bar{\nu}_e e^-$ interaction (Glashow resonance).

And only recently it was found, that in theories of quantum-gravity with low fundamental mass scales of about TeV [19], one is left with a rich phenomenology of observable effects: starting for neutrino energies of around 1 PeV, one obtains a large increase in cross-section through graviton exchange [55]. About an order of magnitude higher in energy an even more spectacular phenomenom can be realized, namely that of Black Hole production [45, 65]. These microscopic black holes would decay immediately through Hawking radiation, into a large number of observable particles. Event rates and possible signatures are discussed in [105].

Any observation of an additional contribution to the total cross-section will rely on previous detection of the neutrino flux. Hence this adds motivation to the eminent goal of detecting the potential flux of high-energy astrophysical neutrinos, which is the topic of this thesis.

3.2 Neutrino Event Signatures

Various particles produced in the interaction of neutrinos of different flavors lead to distinct detection channels.

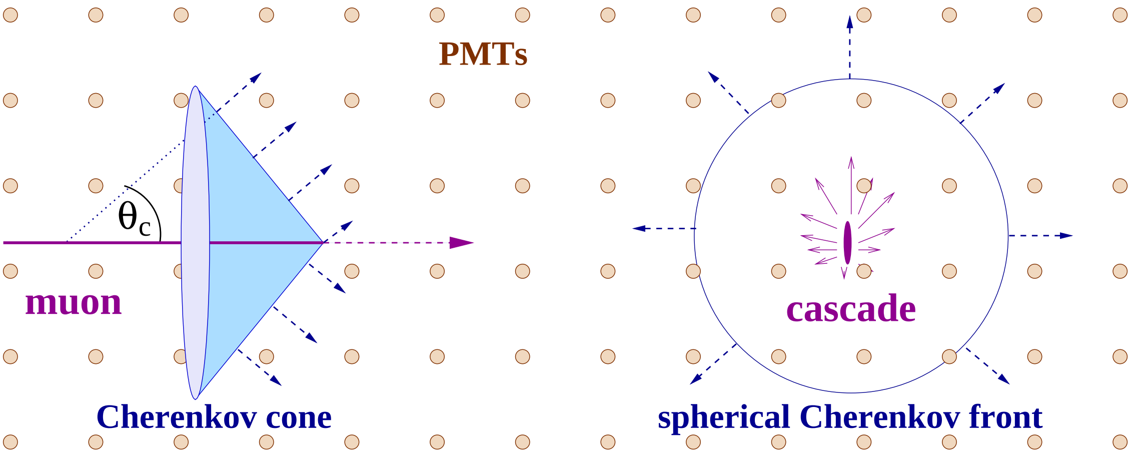

Figure 3.2.1: Illustration of event topologies of a muon track (left) and of a cascade (right). The thin dashed arrows represent Cherenkov photons, which in case of the cascade are emitted more isotropically. The circles represent the Optical Modules of the detector (see section 4).

- In case of a CC reaction of a muon-neutrino, a muon is produced which can travel large distances. For sufficiently high energies, a muon neutrino interaction can be detected, even if the interaction vertex is located many kilometers away from the detector. Due to the distinct muon track, this class of events is called *track-like*.

- Electron-neutrinos have a considerably different appearance. Through a charged current reaction, an electron is produced, which leads to an electromagnetic cascade as well as a hadronic cascade from the interaction vertex. The extension of such an electromagnetic and hadronic cascade is small (see section 3.4.1) compared to the spacing of Optical Modules within a typical Cherenkov telescope (see chapter 4). An interaction of an electron-neutrino with a nucleus is only detectable if the vertex is located within or close to the detector.

- In the case of CC reaction of a tau-neutrino, a tau is emerging which, due to its short lifetime, decays while still being highly energetic. At an energy of 1 PeV, the average decay length is 49 meters [130]. The average decay length is growing linearly with energies up to about 100 PeV. At higher energies, the energy loss of the tau lepton has to be taken into account. Events are called *double-bang* if the two cascades from the interaction vertex and from the decay of the tau are resolvable [111].

- Neutrinos of all flavors react in a similar way by a NC reaction. In such a reaction only the hadronic cascade from the interaction vertex is visible since the neutrino escapes unobserved.

Current Cherenkov neutrino telescopes are not able to separate hadronic from electromagnetic cascades. Hence the separation of a CC electron-neutrino reaction from a NC induced hadronic cascade is not possible. And unless tau-neutrinos appear as double-bang events, they will not be separable from electron-neutrino events as well. Therefore one classifies the events which are detected through an electromagnetic or hadronic cascade as *cascade-like events*. Figure 3.2.1 illustrates the topology of both track-like and cascade-like events inside a Cherenkov telescope. A muon neutrino will be detected through the characteristic light profile from Cherenkov radiation along the track. Cascades will appear distinctly different, due to the compactness of the emitting region as well as the more isotropic radiation pattern.

3.3 Cherenkov Light

Ice or water are relatively dense optical media, with an index of refraction of $n \approx 1.33$. Charged particles moving through a medium with a speed $v = \beta c$ faster than the speed of light in that medium, c/n, produce Cherenkov light. The majority of the photons are emitted under an Cherenkov angle, $\theta_C = \arccos\left(\frac{1}{\beta n}\right)$ relative to the motion of the emitting particle. In case of ice and $\beta = 1$ the emittance angle is $\theta_C \approx 41°$.

For a particle of unit charge the number of photons emitted per unit track length, x, and wavelength, λ, is given by the Franck-Tamm formula [90]:

$$\frac{\mathrm{d}^2 N}{\mathrm{d}x \mathrm{d}\lambda} = 2\pi\alpha \frac{1}{\lambda^2}\left(1 - \frac{1}{(\beta n)^2}\right), \tag{3.3.1}$$

where α is the fine structure constant. While the total energy loss through Cherenkov radiation is considerably smaller than that due to ionization, Cherenkov emission is important because of the large number of photons with detectable wavelengths. Between a wavelength of 500 nm, below which the ice becomes transparent, and 300 nm, above which the glass of the Optical Module is most transparent, one expects about 200 photons per centimeter track length for a particle traveling with $\beta = 1$.

3.4 The Physics of Cascades

In this section basic characteristics of electromagnetic and hadronic cascades are reviewed. We focus on the properties relevant for large water or ice neutrino Cherenkov telescopes, such as the Cherenkov light yield and longitudinal development of a cascade. At the beginning, the simpler case of electromagnetic cascades is discussed, which is well suitable to explain the basic principles of cascade development.

3.4.1 Electromagnetic Cascades

An energetic electron passing through matter initiates an electromagnetic cascade. The electron radiates a hard γ quantum through bremsstrahlung, which in turn produces an electron and positron pair in interaction with matter. This process is iteratively repeated and hence leads to the cascade development. The average distance after which the energy of an energetic electron is reduced to $1/e$ is called the radiation length, X_0. A simplistic model of a cascade assumes, that for each radiation length, two electrons are produced sharing part of the energy of the original electron. This process is repeated, until the energy of all electrons reach the critical energy, E_c, for which the energy loss of the electrons begins to be dominated by ionization. Further cascade development is then suppressed. In this model the length of the cascade initiated by an electron of energy E is described by:

$$X = X_0 \ln \frac{E}{E_c}. \tag{3.4.1}$$

In ice, characteristic values for the critical energy and radiation length are $E_c \sim 80$ MeV and $X_0 \sim 40$ cm. This simple model has a few important properties which are shared with the more realistic Monte Carlo simulations discussed below: The longitudinal dimension of a cascade is only logarithmically dependent on the energy and generally does not exceed a few meters. The number of electrons produced in a cascade, and hence the total track length is proportional to the energy of the cascade.

To estimate the Cherenkov light yield of a cascade, the total track length of all electrons in a cascade is an important quantity. The largest contribution to the track length is from electrons below the critical energy. Hence in a good approximation the total track length, T, scales linearly with the cascade energy, E:

$$T(E) = \text{const} \cdot E \approx (\mathrm{d}E/\mathrm{d}x)^{-1}_{\text{ion}} \cdot E$$

with $(\mathrm{d}E/\mathrm{d}x)^{-1}_{\text{ion}}$ being the energy loss of electrons due to ionization. Many detailed simulations of the exact proportionality constant for water have been performed, where the results vary as much as ±20 % [176,168,11]. Hence the calculation was repeated for ice as detector medium using the GEANT4 simulation package [2]. The value found for the total track length above a cut-off energy of 0.1 MeV is 5.9 m/GeV, which agrees within 5 % with the latest calculation of [11].

Once one includes the effect that electrons slow down and thereby produce less Cherenkov light (see formula (3.3.1)), one obtains a reduced *effective* track length of 5.2 m/GeV. It is this effective track length, which is used for calculating the number of Cherenkov photons from an electromagnetic cascade. For a more detailed discussion the reader is referred to [103].

The longitudinal energy deposition of a cascade as a function of depth (in units of radiation length), $t = x/X_0$, can be approximately described by:

$$\frac{\mathrm{d}E}{\mathrm{d}t} = E_0 \, b \, \frac{(tb)^{a-1} e^{-tb}}{\Gamma(a)}, \tag{3.4.2}$$

with Γ being the gamma function and E_0 the energy of the cascade. The parameters a and b were obtained for water by fitting the parameterization (3.4.2) to the data of a GEANT 3.21 Monte Carlo simulation [168]:

$$a = 2.03 + 0.604 \cdot \ln(E_0/\text{GeV}); \; b = 0.633. \tag{3.4.3}$$

The cascade maximum energy loss occurs at $t_{\max} = (a-1)/b$, and hence one obtains a logarithmic growth of the longitudinal size of a cascade for linearly increasing energy. The maximum of a 100 TeV electromagnetic cascade occurs at 5 m.

The angular distribution of Cherenkov light is peaked at the Cherenkov angle with parameterizations for the angular distribution provided in [168].

3.4.2 Hadronic Cascades

The correct treatment of hadronic cascades is not a simple task. A variety of different physics processes take place within the cascade and result in a non-linear scaling of the total track length with energy as well as significant fluctuations around the average value[1].

Hadronic cascades produce less Cherenkov light than electromagnetic cascades for several reasons: A large number of slow (invisible) neutrons are produced within the cascade. The visible energy is reduced by large losses due to the needed binding energies involved in hadronic processes. And finally, the energy threshold for Cherenkov radiation of charged hadrons is higher than for electrons. The ratio of track length from a hadronic and electromagnetic cascade of the same energy,

$$F = \frac{T_{\mathrm{hadron}}}{T_{\mathrm{em}}}, \tag{3.4.4}$$

is therefore always smaller than one. However, F increases with energy. In each secondary interaction a substantial fraction of produced particles are π^0, which decay electromagnetically. π^0 production represents a "one way street" [57], meaning that for every generated π^0 one gets an increase of electromagnetic activity within the cascade. With increasing cascade energy, the number of π^0 increases and the cascade becomes more electromagnetic-like. The ratio, F, can be represented as a function of the electromagnetic fraction, F_{em}, of the cascade:

$$F = F_{\mathrm{em}} + (1 - F_{\mathrm{em}}) \cdot f_0 \tag{3.4.5}$$

where f_0 represents the relative Cherenkov activity of the pure hadronic part of the cascade. In [57], a simple phenomenological model of the energy dependence of F_{em} was introduced and it was shown to describe both experimental and simulated data:

$$F_{\mathrm{em}} = 1 - (E/E_0)^{-m}. \tag{3.4.6}$$

E is the energy of the hadron while E_0 and m are parameters of the model which depend on the injected hadron and the detector material. Since m is positive, the cascade indeed becomes more electromagnetic-like with increasing cascade energy. Such a parameterization is useful because it allows extrapolation into an energy region, $E \gg 1$ TeV, where no reliable Monte Carlo programs are available.

Figure 3.4.1 shows a GEANT4 simulation of F up to energies of 3 TeV for a number of different injected hadrons into a large block of ice. The above model for F was fitted for each of the hadron types. The resulting parameters of the fit are summarized and further discussed in [103]. With the exception of the p^-, the χ^2 of the fits are reasonable small with $\chi^2/5 = 0.7 - 1.9$. The p^- has to be treated separately, as the additional large annihilation cross-section is not foreseen within the model leading to equation 3.4.6.

Figure 3.4.2 shows the root mean square (RMS) of the distributions of F. The event to event fluctuations are particularly large for small hadron energies and then decrease with energy. It has been noted before [171] , that the width decreases slower with energy than

---

[1] Previously AMANDA simulation has treated hadronic cascades as electromagnetic cascades with a reduced light yield of 80 %.

$1/\sqrt{E}$ and is better described by $1/\log E$. The parameterizations shown in the figure have been obtained by fitting:

$$\mathrm{RMS} = \mathrm{RMS}_0 \cdot (\log E)^{-\gamma}, \tag{3.4.7}$$

to Monte Carlo data. The resulting parameters for m, E_0, f_0, γ and RMS_0 can be found in [103].

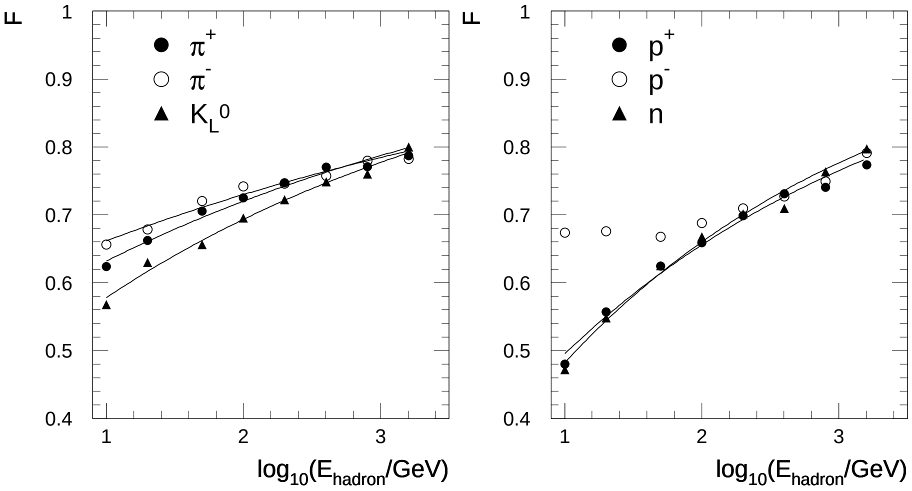

Figure 3.4.1: Ratio of light yield of hadronic and electromagnetic cascades for different energies and particle types. The full lines are the fitted parameterization (3.4.6).

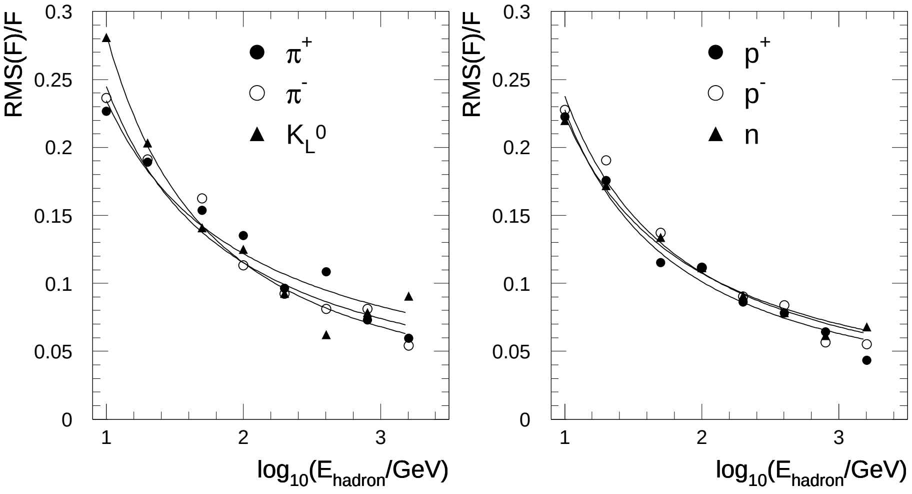

Figure 3.4.2: The relative width (RMS) of the F-distributions as a function of energy and injected particle type.

A hadronic vertex cascade is initiated by fragmented particles of the final state. The visible fraction, F_X, of the energy, $E_X = yE_\nu$ depends strongly on the distribution of fragmented particles within the final state. The largest fraction of the energy is carried by a few leading particles. Realistic final states from neutral current neutrino nucleon reactions have been generated with PYTHIA 6.2 [144] and the light yield from the fragmented particles has been superimposed, to obtain the light yield of the full vertex cascade. In analogy to (3.4.4) F_X is introduced as:

$$F_X = \frac{\sum E_i F_i(E_i)}{E_X}. \tag{3.4.8}$$

The index i represents the fragmented particles species. Figure 3.4.3 displays F_X over a large range of hadronic energies, E_X. The parameterization obtained from fitting the functions (3.4.5) and (3.4.6) generally describes the simulated data well, with the exception of the lowest energies. But since these low energies are currently not relevant for the bulk of the AMANDA events, the simple parameterization is sufficient.

The fluctuations of F_X can be estimated by adding the uncorrelated fluctuations from the shower development, RMS1, and that from the fragmentation, RMS2:

$$\mathrm{RMS1} = \frac{\sum (E_i F_i \mathrm{RMS_i(E_i)})^2}{\sum (E_i F_i)^2}, \tag{3.4.9}$$

$$\mathrm{RMS2} = \frac{\mathrm{RMS}(F_X E_X)}{F_X E_X}, \tag{3.4.10}$$

$$\mathrm{RMS_X} = \sqrt{\mathrm{RMS1}^2 + \mathrm{RMS2}^2}. \tag{3.4.11}$$

Here, RMS_i refers to the parameterization (3.4.7) and $\mathrm{RMS}(F_X E_X)$ refers to the RMS of the distribution of $F_X E_X$. Both contributions as well as their quadratic sums are shown in the right plot of figure 3.4.3.

	E_0	m	f_0	RMS_0	γ
X	0.399	0.130	0.467	0.379	1.160

Table 3.4.1: Fitted parameters for hadronic final states induced by neutral current neutrino-nucleon reactions.

3.5 Expected Event Rates

In this section, the expected rates of neutrino-induced cascades are discussed. The background in the search for neutrino-induced cascades consists of atmospheric muons with energies large enough to propagate down to the depth of the detector. The rate of neutrino-induced cascade events is compared to the rate of cascade events due to energetic secondaries particles radiated by atmospheric muons.

3.5.1 Neutrino-induced Cascades

The expected rates of neutrino-induced events can be calculated with the help of the ANIS MC generator (see section 6.2.3). For calculating event rates we focus on ν_e events, since

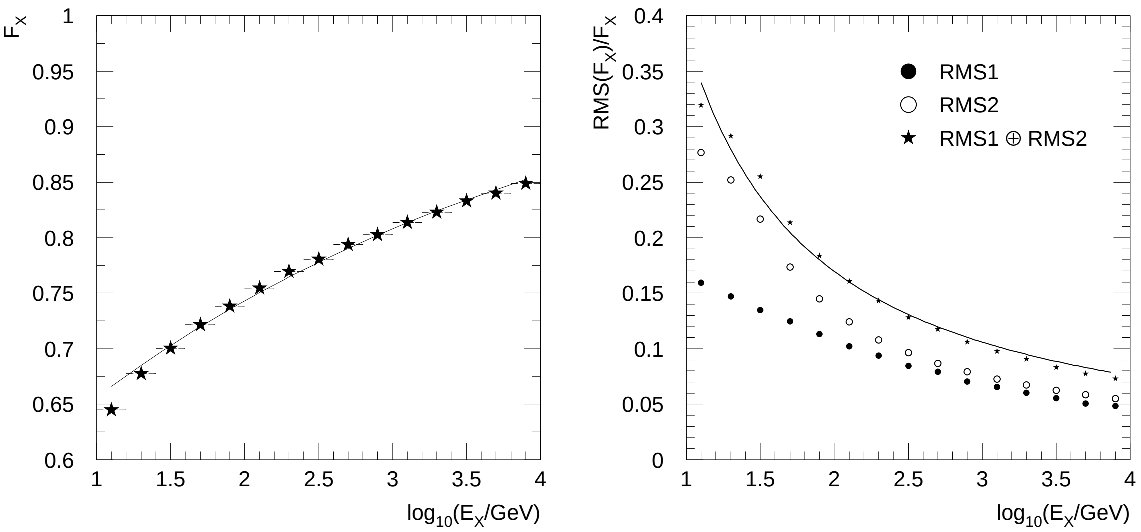

Figure 3.4.3: *Left*: The fraction of visible energy of the hadronic final state energy E_X is displayed as a function of E_X. Neutral current neutrino-nucleon interactions at $2^n\cdot$ 30 GeV energies (n=1,2,..9) have been simulated. *Right:* The size of the fluctuations around the average value F_X. The two independent contributions are shown separately.

their signature are cascades with visible energies which mostly match the energies of the neutrinos. Additionally, for the analysis presented in this dissertation the sensitivity for ν_e is generally larger than for ν_μ and ν_τ.

The resulting energy distributions of $\nu_e + \bar{\nu}_e$ events for an atmospheric spectrum and a hypothetical astrophysical diffuse flux (labeled agn) of strength $\phi_\nu(E) = 1 \times 10^{-6} E^{-2}$ GeV^{-1} cm^{-2} s^{-1} sr^{-1} are shown in figure 3.5.1. The intensity of the flux was chosen roughly in accordance with current existing experimental upper limits. The spectral shape represents that expected from Fermi acceleration. In order to illustrate the effects of neutrino absorption in the earth, the contributions from the upper and lower hemisphere are shown separately. It is evident, that when searching for high energy neutrinos above $\gtrsim$ 100 TeV, there is a substantial gain from looking upward.

This is different for ν_τ, which do not get absorbed in the Earth. The τ generated in a CC ν_τ reaction decays while still being very energetic, thereby giving rise to a secondary ν_τ. This chain of processes is called *regeneration.* Because of regeneration the total flux of ν_τ is preserved. However the mean energy of the regenerated neutrinos is reduced to energies at which the Earth becomes transparent to neutrinos. Figure 3.5.2 shows the effects of ν_τ regeneration on the flux of neutrinos. The ratio of neutrino fluxes at the detector to those injected at the surface of the Earth is shown as a function of the neutrino energy for both ν_τ and ν_e for two different angles of incidence. The spectrum of the injected neutrino flux is $\phi \propto E^{-\gamma}$ with $\gamma = 1$ (left figure) and $\gamma = 2$ (right figure). As can be seen, for the harder injected flux regeneration effects lead to a considerable increase in the flux of ν_τ at the detector when compared with the case of ν_e. For the softer spectrum, the differences between the flavors are smaller. However, since the energy of regenerated ν_τ is reduced,

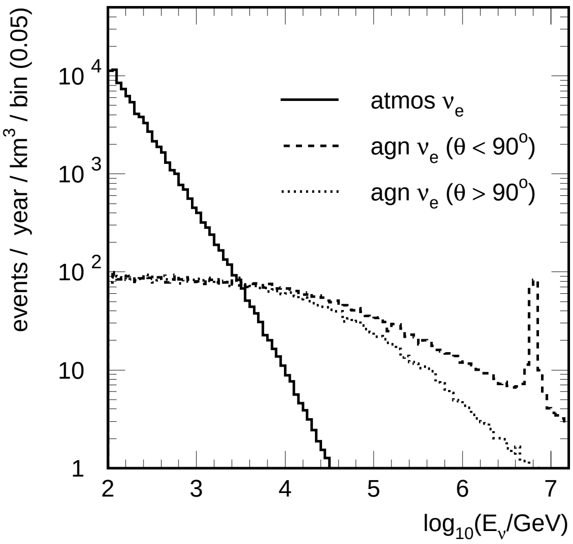

Figure 3.5.1: Number of $\nu_e + \bar{\nu}_e$ events per $(\mathrm{km}^3\ \mathrm{year})$ are shown as a function of energy. The rates expected for the flux of atmospheric neutrinos (labeled atmos) and for a hypothetical astrophysical flux ($\propto E^{-2}$, labeled agn) are presented. The event rates for the astrophysical flux are shown separately for neutrino directions from above and below the horizon.

its interaction probability is smaller as well. Hence, even when searching for ν_τ there is a gain from looking upward.

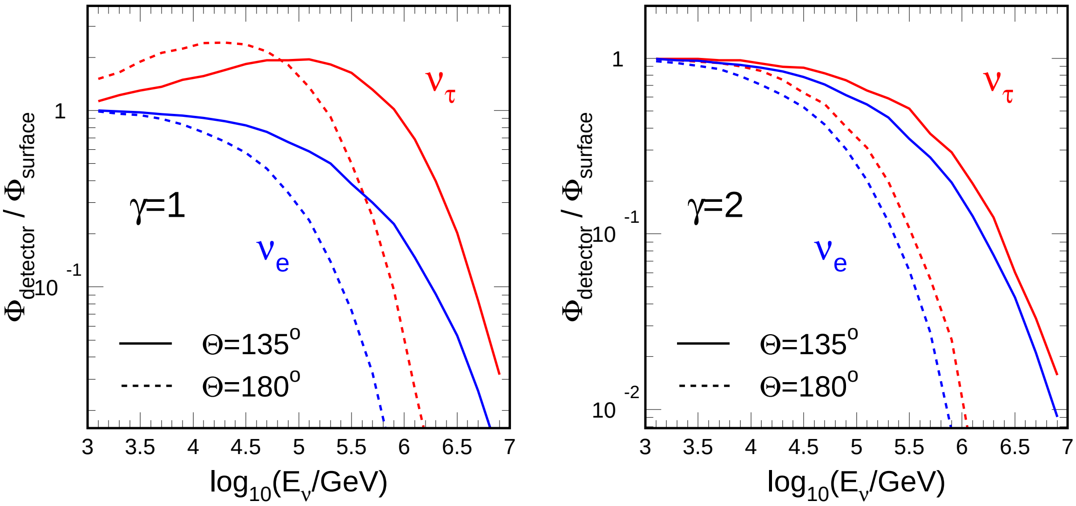

Figure 3.5.2: Ratio of the neutrino flux at the detector to that injected at the surface of the Earth as a function of the neutrino energy for both ν_τ (upper curves) and ν_e (lower curves) and two incidence angles $\theta = 135°$ (full line) and $\theta = 180°$ (dashed line). The spectral index of the flux at the surface is γ=1 (left plot) and γ=2 (right plot).

3.5.2 Background due to Atmospheric Muons

High energy atmospheric muons are generated in the same reactions as atmospheric neutrinos (see section 2.4.3). If these muons are of sufficiently high energy, they can propagate through large water or ice overburden to produce a visible muon track within the detector. The rate of such muon events in AMANDA is with approximately 10^9 events per year about 6 orders of magnitude higher than the rate of events due to atmospheric neutrinos. The background of atmospheric muons is easily reducible, since the topology of a muon track is distinctly different from that of a cascade. However, if a muon radiates a large fraction of its energy into a single secondary particle, the chance of mis-identification rises. As will be shown in later chapters, the reconstructed energy of such an event corresponds to the energy of the most energetic secondary particle radiated in the near environment of the AMANDA detector. After a brief discussion of the muon energy loss processes, the background due to secondaries is estimated.

Muons propagating through matter suffer from various types of energy losses. At muon energies $\gtrsim$ 500 GeV, radiative energy losses dominate over continuous energy loss due to ionization. Radiative processes consist of bremsstrahlung, e^+e^- pair production and photo-nuclear interactions. Ionization also contributes to stochastic energy losses through knock-on δ electrons. Detailed reviews can be found in [138, 114, 130].

Radiative energy losses are characterized by the associated secondary particles leading to electromagnetic and (in the case of photo-nuclear interactions) hadronic showers. The radiative cross-sections can be expressed as a function of the fractional energy loss, $\nu = E_{\text{secondary}}/E_\mu$. Bremsstrahlung has the hardest radiation spectrum with a cross-section $\mathrm{d}\sigma/\mathrm{d}\nu$ roughly proportional to $1/\nu$ [160]. The cross-section $\mathrm{d}\sigma/\mathrm{d}\nu$ has only a weak dependency on the muon energy.

The spectra of radiated secondaries are shown in figure 3.5.3 for 10 TeV muons propagating through rock [39]. Note that the histogram has logarithmic energy bins, hence the spectrum of bremsstrahlung appears nearly flat.

Using the Monte Carlo programs available for simulation of atmospheric muons in AMANDA (see section 6.2), one can evaluate the energy spectrum due to radiation of secondary particles. Figure 3.5.4 shows the spectrum of the most energetic secondary particle per event within a cylindrical volume of 500 m height and 200 m radius located at the depth of the AMANDA detector. The dominant contributions from knock-on δ electrons (for low energies) and bremsstrahlung (for high energies) are shown separately. The spectral shape of muon energies at the detector depth, above 500 GeV, steepens to follow that at the surface $\phi \sim E^{-3.7}$ [58, 130]. Since $\mathrm{d}\sigma/\mathrm{d}\nu$ has only a weak energy dependence, the spectrum of secondaries can be described by a power-law as well. The data above E=3 TeV was fitted with a power-law ($\chi^2/\text{ndf} = 18.5/12$), resulting in the parameterization:

$$\frac{\mathrm{d}N}{\mathrm{d}E} = 8.2 \cdot 10^{13} \times (E/\text{GeV})^{-3.48} \left[\text{GeV}^{-1}\text{km}^{-3}\text{year}^{-1}\right] . \tag{3.5.1}$$

It is instructive to compare the rate of background events with that expected from ν_e signal events (see section 3.5.1). Figure 3.5.5 shows the event rates as a function of the threshold energy E_{thres} for background due to secondary particles, atmospheric ν_e

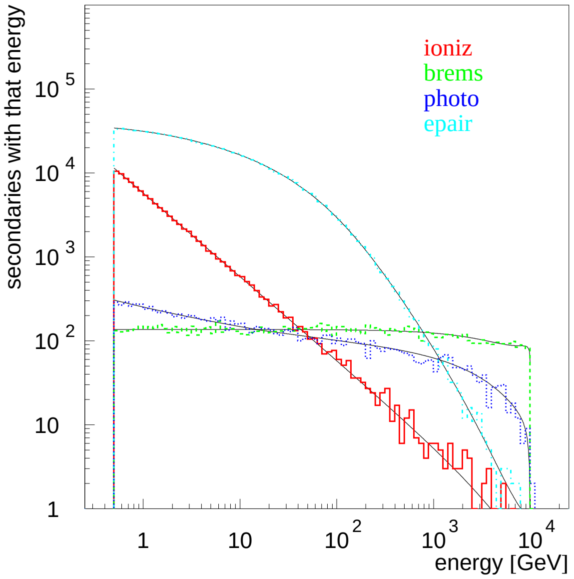

Figure 3.5.3: Distribution of secondary particles as a function of energy radiated by 10 TeV muons in rock. The processes are (from top to bottom at 1 GeV): Pair production, ionization, photo-nuclear interaction and bremsstrahlung. Figure taken from [39].

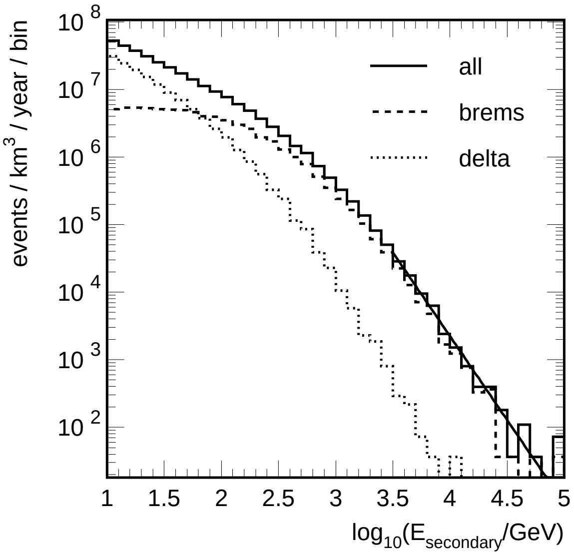

Figure 3.5.4: Spectrum of secondaries from atmospheric muons at AMANDA depth. Each entry consists of the most energetic secondary radiated by the muon. The dominating processes are at low energies δ electron production and at high energies bremsstrahlung. The smooth line represents the result of a fit (see text for details).

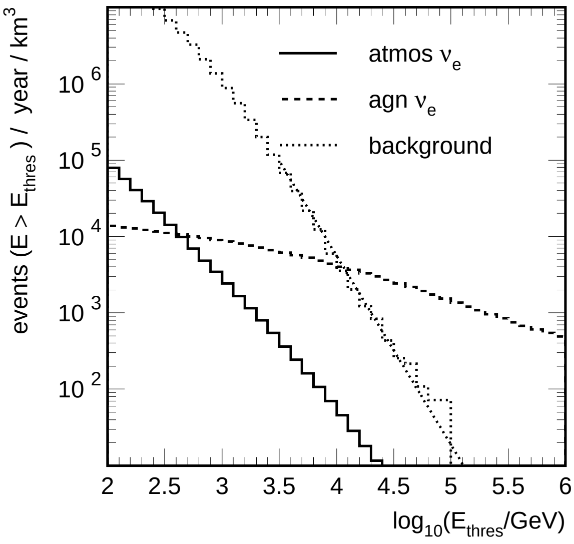

Figure 3.5.5: Rate of events above the energy threshold E_{thres}. Shown are distributions for the background due to secondary particles from atmospheric muons, atmospheric ν_e and a hypothetical flux of ν_e (labeled agn) given by $E^2\phi = 10^{-6} \times\ \mathrm{GeV\ s^{-1}\ sr^{-1}\ cm^{-2}}$.

and a hypothetical flux of ν_e given by: $E^2\phi(E) = 10^{-6} \times\ \mathrm{GeV\ s^{-1}\ sr^{-1}\ cm^{-2}}$. This hypothetical flux of ν_e exceeds the background for energies above 10 TeV. However, an efficient background suppression, as for example possible through a well reconstructed incidence angle, would lower this crossing energy.

Chapter 4

The AMANDA Detector

The AMANDA detector, located at the geographical South Pole, has been deployed in four campaigns between November 1995 and February 2000. The main building blocks of the AMANDA detector are the optical modules (OMs). An OM consists of a large Photo Multiplier Tube (PMT), housed by a pressure resistant glass sphere. The OMs are arranged on vertical strings deployed to large depths into the Antarctic Glacial ice. The main instrumented volume ranges from 1550 m-1950 m depth below the surface, and forms a cylinder of 200 m diameter (see figure 4). The deployment process consists of two parts. First, using a hot water drill, a hole of 60 cm diameter is melted into the ice. The drilling of the individual holes takes on average 72 hours. Then the strings holding the OMs are deployed into the hole. The actual deployment takes about 12 hours and must be completed before the hole starts freezing again. After 48 hours the hole is fully frozen.

The position of the 19 strings are arranged on three concentric circles around the central axis of the detector. The first four strings, deployed in 1995/96, are arranged on a circle of radius 35 m. One year later additional 6 strings were deployed on a second circle of radius 60 m. This intermediate detector-stage, consisting of 10 strings and 302 OMs is referred to as AMANDA-B10. In the campaign 1997/98, three longer strings were deployed on a circle of 100 m radius. The OMs on those strings are located between 1300 m-2400 m, and where used to extend the measurements of the ice properties to larger and smaller depth. In the campaign 1999/2000, the AMANDA-II detector was completed to its present form, consisting of 19 strings and 677 OMs. An irregularity in the drilled hole diameter did not allow to deploy string 17 below a depth of 1500 m. The analysis presented in this thesis is based on the data from the first year of operation with the completed AMANDA-II detector.

4.1 AMANDA Technology

The deployment of AMANDA-II went along with a stepwise improvement of PMT signal transmission techniques. Strings 1-10 use OMs with electrical analog signal transmission, while strings 11-19 are based on analog fiber transmission (see table 4.1.1). Analog anode signals from the PMTs are transmitted via electrical cables to the surface (coaxial cables for string 1-4, twisted pair for string 6-10). These cables also transmit the high voltage.

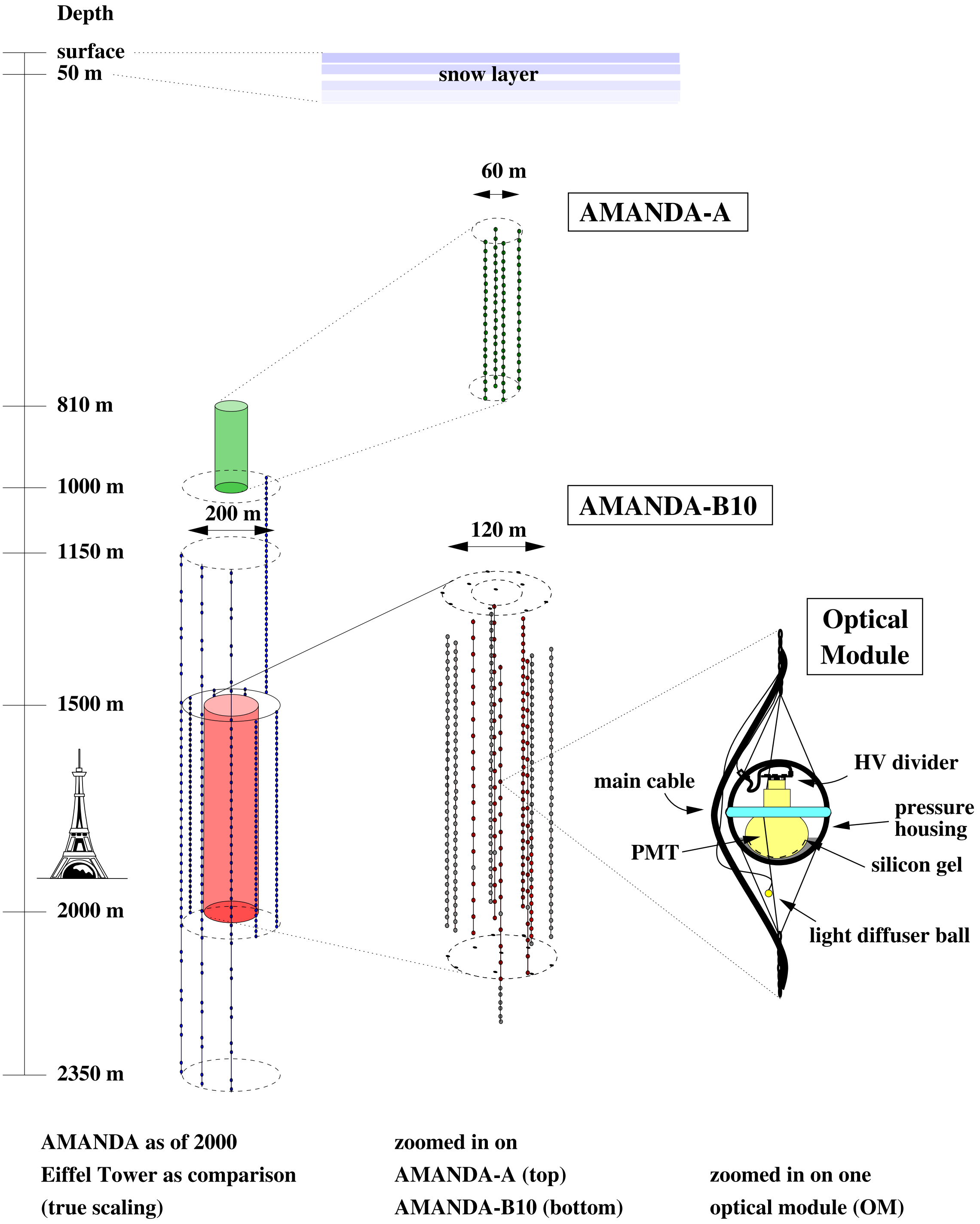

Figure 4.0.1: The AMANDA-II detector, as of 2000.

Hamamatsu R5912-2 PMTs (8 inch) with 14 dynodes are operated at a gain of 10^9 in order to drive the one photoelectron signal over 2 km of cable. In spite of a strong dispersion of the PMT signal along the cable, a time resolution of 5 nsec has been achieved. The majority of the 375 OMs on the outer strings 11-19, is based on analog fiber optic signal transmission without additional local electronics inside the OM. The 123 OMs on strings 11-13 (1997/98) first used this new technique with optical fibers, both for calibration and for analog transmission of the PMT pulses [97]. Electrical transmission was installed as backup. A LED converts the PMT anode current into a light signal which is transmitted to the surface essentially without dispersion (see figure 4.1.1, middle). This results in a high bandwidth, double pulse resolution of ~20 nsec and no need for amplitude-dependent time slewing corrections. The FWHM of pulses generated by a single photo-electron (p.e.) is 14 nsec. Figure 4.1.2 shows a single p.e. pulse as recorded with a twisted pair cable and with fiber-optic transmission. Drawback of the optical technique is a failure rate of about 10% during re-freezing of the ice, since optical connectors and fibers are more vulnerable to the high pressure. For strings 14-19 the analog fiber OMs are operated at a gain of $\approx 3 \cdot 10^8$, allowing enhanced dynamic range (by using a transformer to amplify the PMT anode current that drives the LED transmitter). All of the described OMs have in common that no active electronics have been deployed, and the high voltage for the PMT is provided directly from the surface. Two types of active OM have been deployed. They are provided with low voltage and generate the HV locally using a Cockroft-Walton generator.

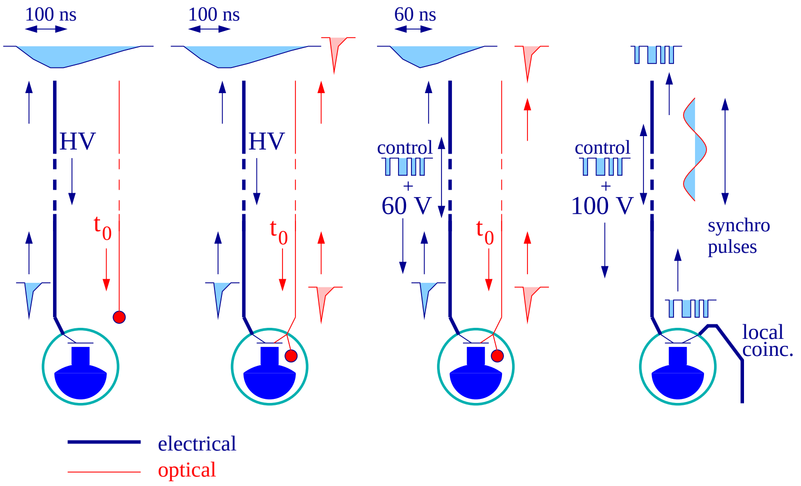

Figure 4.1.1: Electrical (left) and fiber (second from left) readout analog OM (AOM). Digitally controlled module (dAOM, second from right) and digital OM (DOM, right).

23 OMs are based on advanced analog fiber optic signal transmission (dAOM, see figure 4.1.1) [142]. A converter (DC/DC) in the OM converts the 60 V-supply voltage to the low voltage required to operate a microprocessor and other integrated circuits. Thus one can operate the LED (13 OMs) or the Laser diodes (LD, on 10 OMs) with adjustable bias current, and amplify the anode signal in the OM, which allows for lower gain of the

PMT and a higher dynamic range. Finally, another 41 OMs are built as digital optical modules (DOM), the prototype OM for the IceCube detector [68]. In this approach the PMT pulses are digitized in the OM and transmitted to the surface via an electrical cable. These OMs provide fiber-optic analog signals, to allow for integration into the standard data acquisition system (DAQ).

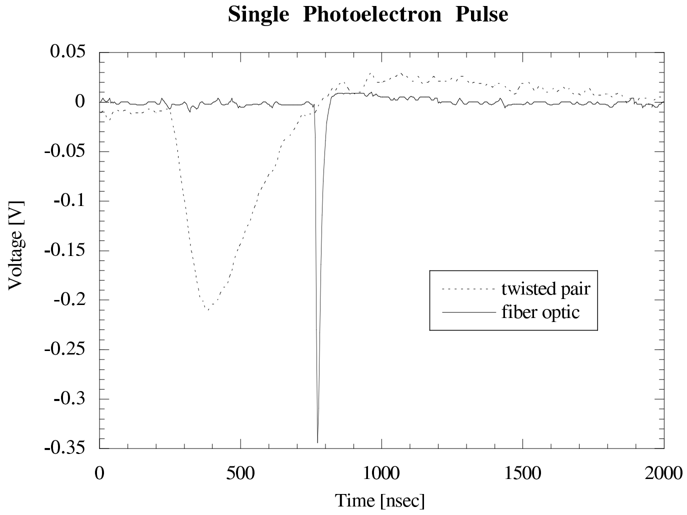

Figure 4.1.2: Single p.e. pulse recorded with twisted pair cable and optical fiber transmission.

4.2 Data Acquisition and Trigger

The arrival times of pulses are recorded with a multi-hit TDC, measuring the leading and trailing edges of up to 8 pulses. The current Data Acquisition System (DAQ) reads out the PMT pulse amplitudes by using peak sensing ADC. The dynamic range of the PMT is limited to about 15 p.e./10 nsec. The integrated dynamic range of an OM can be much larger, since e.g. multi-photon pulses from distant muon tracks (or cascades) are dispersed in time due to scattering. In the season 2002/2003 large parts of the DAQ were upgraded with Flash ADCs. This allows to record more complex waveforms that are generated by

Type	Technology	Number of OMs	Strings
AOM	Coax	80	1-4
AOM	Twisted pair	222	4,5-10
AOM	Fiber optic, LED, twisted pair backup	311	11-17,19
dAOM	Fiber optic, LED/LD, local HV	23	14-19
DOM	Local HV (Fiber optic LED)	41	18

Table 4.1.1: AMANDA-II: Overview of analog (AOM) and digital (DOM) optical modules deployed.

muons and cascades of energies greater than ∼ 10 TeV and will enhance the physics potential for higher energetic events [162].

The AMANDA-II detector has been commissioned in February 2000. The muon and cascade event trigger is based on a a majority trigger logic, requiring a minimal number of 24 OMs hit in a fixed coincidence time window of 2.5 μs. The trigger threshold of the detector for muon or cascade events is about 50-100 GeV. Since February 2001, an additional local coincidence trigger is in operation which aims at increasing the trigger efficiency of low energy muons.

With a data rate of ∼80kB/s, within ∼250 calendar days about 1.3 TB raw data are produced per season. At the South Pole, the data is written to magnetic tapes, and shipped out once per year. The high bandwidth TDRS satellite allows to send out a substantial fraction of raw and filtered data to the northern hemisphere. Additionally, data is provided for online monitoring of the detector performance.

4.3 In-Situ Light Sources

Different light sources are being used for calibration and ice measurements. Additionally, these light sources are used to verify the detector response and reconstruction performance of cascade-like events (see chapter 5). In a first approximation a cascade in AMANDA will appear as a point-like light emitter and hence can be approximated by existing light sources. The angular emittance profile from existing in-situ light sources does not resemble that of a cascade. However, for distances considerably larger than the effective scattering length in ice (see section 4.5) the angular dependence becomes less important and one can approximate the light emission of a cascade with that of in-situ light sources. The wavelength of in-situ light sources is discrete, in contrast to the rather broad spectrum of Cherenkov light. Nevertheless, there are light sources with wavelengths in the relevant spectral range available.

With the exception of the YAG-laser, all of the other pulsed light sources are deployed along with the OMs. The YAG-laser is operated at the surface, and the laser light is transmitted through optical fibers ending in a diffuser ball close to or inside an OM. Table 4.3.1 summarizes the main properties of the different available pulsed light sources.

Type	Location	Wavelength	Intensity per pulse
pulsed YAG-laser	every other OM	532 nm	up to 10^{10} photons
Nitrogen Laser	at 4 locations	337 nm	up to 10^{12} photons
LED (UV)	string 18/19	370 nm	up to 10^9 photons

Table 4.3.1: Overview of pulsed in-situ light sources available in AMANDA.

4.4 Calibration of Time and Amplitude of Hits

The time and amplitude of a recorded hit has to be calibrated, before it can be used for reconstruction. To obtain calibrated hit times, a time offset, called t_0, is subtracted to account for the different cable lengths and delays in the surface electronics. Furthermore, an amplitude dependent correction is applied (called α-correction), to correct for time slewing effects from pulse form dispersion. This is particularly necessary for electrical analog transmitted pulses, where due to the slow rise time (see 4.1.2), large pulses pass the discriminator threshold earlier than small ones.

The calibration constants t_0 and α are obtained from an analysis of YAG laser runs. Light of a pulsed YAG laser is generated at the surface and transmitted through a light fiber to an OM. The length of the fiber is precisely known through a measurement with an OTDR (Optical Time Domain Refractometry). From the time difference between injected laser light and received PMT response, one subtracts the time the laser light needs to reach the OM. The distribution of these time differences is well described (within the resolution of the PMT and DAQ system) by a constant (t_0) and an amplitude dependent part (α). The resulting calibration constants are stored in a data base [12]. After calibration, the time resolution of a PMT pulse becomes better than 5 ns.

An independent approach for obtaining the time calibration constants is to use atmospheric muon events [44]. In an iterative procedure, the timing calibration constants are modified to produce optimal fit results. Both methods lead to consistent results.

The calibration of amplitudes of the pulse height of an OM pulse is a rather simple procedure. One uses atmospheric muon data, to obtain for each OM a spectrum of registered amplitudes (in mV). Since the average light intensity from atmospheric muons is low, the registered spectrum is dominated by single photo-electrons (p.e.). The mean amplitude of a single p.e. pulse is then determined from a fit to the spectrum of uncalibrated amplitudes [142]. To obtain an estimate for the amplitude of a hit in units of registered photons, one divides the registered amplitude by the mean single p.e. amplitude. The resolution of the amplitude is given by the width of the single p.e. peak and is about 35 %. The linearity of the amplitude response is only valid for pulse heights of $\lesssim 5$ p.e..

4.5 Optical Properties of the Ice

The optical properties of the ice surrounding AMANDA are of crucial importance for the performance of the detector. Scattering and absorption of photons in ice affect the arrival times and probability of photons at an OM. Hence the AMANDA collaboration has performed detailed measurements of the optical properties of the surrounding ice [174].

The most important optical properties of the ice can be characterized by three variables, namely the scattering length, λ_{scatt}, the absorption length, λ_{absorb}, and the mean scattering angle of the photons, $\langle\cos\theta\rangle$. It is useful to introduce an effective scattering length, $\lambda_{\text{scatt}}^{\text{eff}}$, which combines scattering length and average scattering angle to:

$$\lambda_{\text{scatt}}^{\text{eff}} = \lambda_{\text{scatt}}/(1 - \langle\cos\theta\rangle).$$

The average scattering angle for photons from dust is $\langle\cos\theta\rangle \approx 0.95$.

The ice properties as a function of wavelength and depth are obtained by observation of light from in-situ light sources in the ice. For a large set of different emitter and receiver positions, the distributions of arrival time and amplitude of hits are recorded. The optical parameters are then inferred from a comparison of the observation to the various outcome of a detailed photon propagation Monte Carlo generated for a large range of parameters.

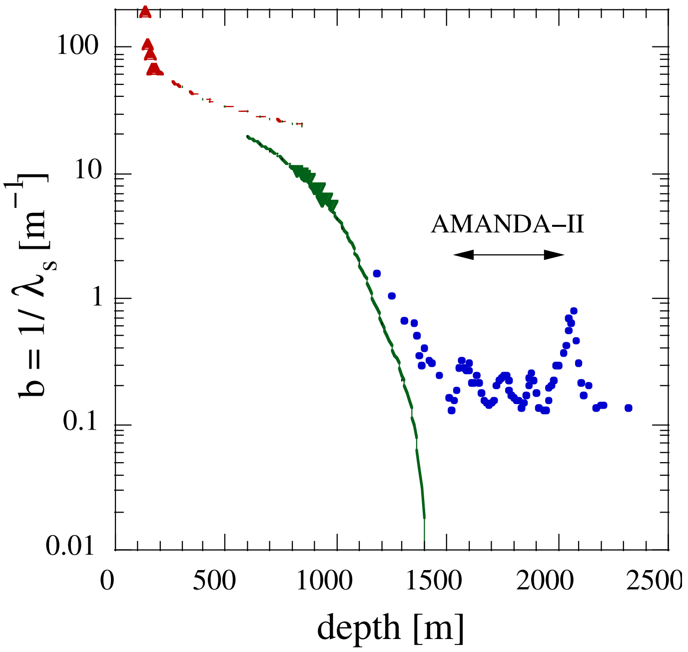

Figure 4.5.1: The depth dependence of the scattering coefficient [174]. The dashed line corresponds to the expected decrease of scattering due to a compression effect of air bubbles of constant concentration. The solid line is a prediction of a model for the transition of air bubbles to air hydrate crystals [133]. Below 1300 m, dust impurities start to dominate.

The optical properties are a result of the intrinsic molecular and crystalline properties of ice as well as the amount of air bubbles and dust concentration within the ice. The depth dependence of the scattering coefficient which is the reciprocal of the scattering length ($= 1/\lambda_{\mathrm{scatt}}$), is shown in figure 4.5.1. Down to a depth of about 1300 m, the residual air bubbles dominate the scattering. For larger depth the large pressure leads to a transformation of the air bubbles into air hydrate crystals. Air hydrate crystals do not contribute significantly to photon scattering anymore, and instead scattering of dust starts to dominate. Due to historic climatological variations, the dust concentration varies as a function of depth leading to the observed distinct peaks in the scattering coefficient.

The concentration of impurities in the ice of the Antarctic glacier is low, leading to a large absorption length. However, the absorption length is wavelength dependent. The measured wavelength dependence of the absorption coefficient ($= 1/\lambda_{\mathrm{absorb}}$) of the ice at two different depths is shown in figure 4.5.2. The lower curves are a prediction for the absorption coefficient using a model for the optical properties of ice [76]. Also shown is the weaker wave length dependence of the scattering coefficient.

For $\lambda \gtrsim 500$ nm, the intrinsic properties of ice are responsible for a loss in transparency leading to a natural infrared cut-off. For small wavelengths the relevant lower bound ($\lambda \lesssim 320$ nm) is currently provided through the optical properties of the glass of the OM pressure housing [152]. For the wavelengths in between, the absorption length is $\lambda_{\mathrm{absorb}} \sim 75 - 200$ m in the depth range of AMANDA.

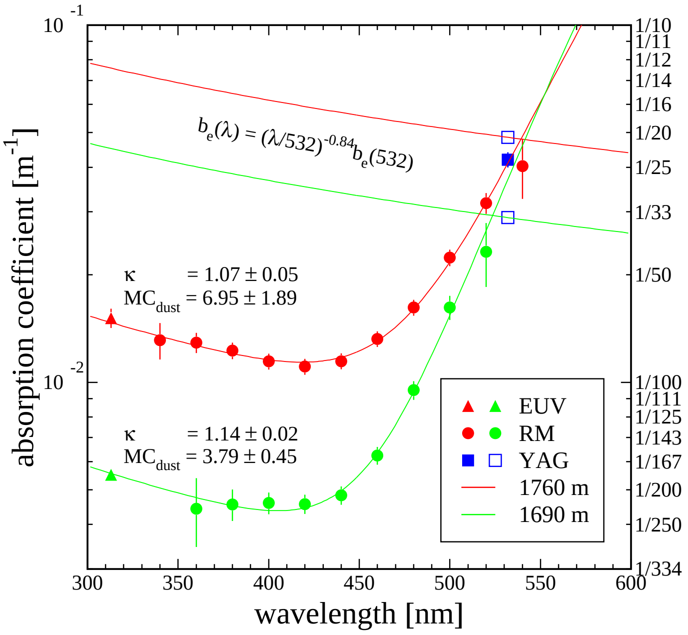

Figure 4.5.2: The measured wavelength dependence of the absorption coefficient is shown for two different depth. Data from light sources operated at different wavelength has been used. The curves are predictions from a model [76]. Also included in the figure is the weaker wavelength dependence of the scattering coefficient, $b_e(\lambda)$ [174].

Chapter 5

Reconstruction of Cascade-Like Events

A reconstructed cascade is characterized by a position, the energy and a direction. These parameters are calculated from the information of the hits, namely the time and the amplitude of the PMT pulse. In section 5.1 we introduce a fast algorithm for estimating the position and time of the vertex of the cascade. The result of this algorithm was used to seed the more complicated vertex reconstruction methods, described in section 5.2. Finally, the energy and direction reconstruction methods are described in section 5.3 and 5.4.

5.1 A First Guess Algorithm for Cascades

Fast reconstruction methods, returning only rough estimates of the position, direction and energy of a cascade are useful for different reasons. The results are used for construction of a low level event filter, necessary to allow application of more time consuming reconstruction methods. Additionally, they are used as a seed for a later fit, making the fit thereby more robust. Such methods are commonly referred to as *first guess* methods.

In this section, the so called *c_first* algorithm is described. While the vertex position and time resolution of the algorithm is not very good, it provides important filter variables. The algorithm works in two steps: first the vertex position is estimated and then the vertex time.

The vertex position is estimated using the *center of gravity* (COG) method. The mean of the OM location of all hits is used as the approximate vertex position, $\vec{r}_{\mathrm{casc}} = \langle w_i \vec{r}_i \rangle$, where each position is weighted by the amplitude w_i of the first hit. For cascades inside a fiducial volume of AMANDA-II (defined as a cylindrical volume of 100 m radius and 400 m height), the position resolution for each coordinate is about 15 m. While the disadvantage of such a simple method is obvious (the COG method can not represent correctly cascades outside of the detector) it serves sufficiently well as a seed for the more complex likelihood methods described in section 5.2.

In a next step, the vertex time is estimated. For that purpose one introduces the new variable,

$$t_{\mathrm{residual}} = t_i - t_v - \frac{d_i}{c_{\mathrm{ice}}}, \tag{5.1.1}$$

where t_i is the time of the hit, t_v the time of the vertex interaction and d_i the distance between the hit OM and the COG. The time residual, t_{residual}, is hence defined as the delay of the hit with respect to the shortest physically possible arrival time. In order to estimate t_v one calculates a shifted time residual for each hit: $t'_{\mathrm{residual}} = t_i - d_i/c_{\mathrm{ice}}$. For each hit within 100 m distance to the vertex position one opens a 200 ns gate, starting at t'_{residual}. The number of successive hits, $N_{\mathrm{dir}}^{0:200}$, is counted which have a t'_{residual} within the 200 ns time window. The estimated vertex time is then given by the smallest t'_{residual}, for which $N_{\mathrm{dir}}^{0:200}$ is larger than a minimum number of demanded hits , $N_{trigg} = 4$. This is illustrated in figure 5.1.1. If the trigger-condition is not met, a case which is very unlikely for a cascade signal, the vertex time is estimated to be the time of the first hit within a 30 m sphere around the vertex. The resolution of the vertex time obtained with the *c_first* algorithm is of the order of 100 ns.

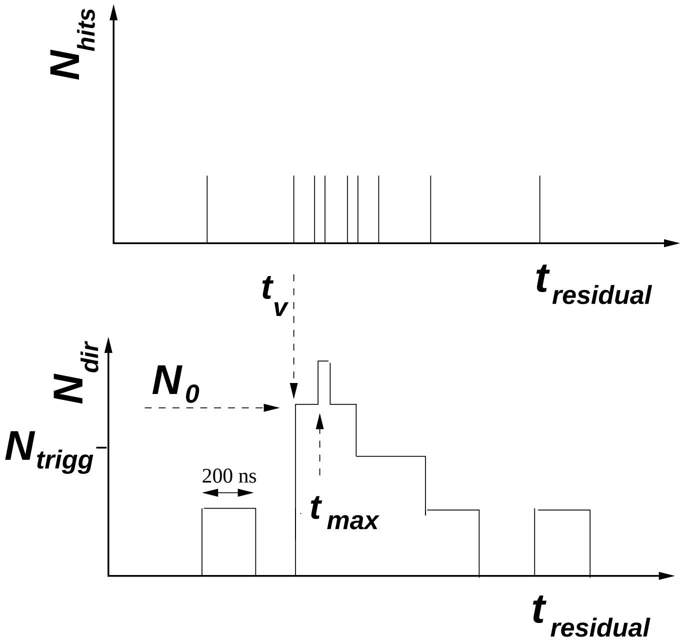

Figure 5.1.1: An illustration of the vertex time determination. Top figure: example of a distribution of hit-time residuals, $t'_{\mathrm{residual}} = t_i - d_i/c_{\mathrm{ice}}$. Bottom figure: corresponding distribution of $N_{\mathrm{dir}}^{0:200}$, the number of hits following within a time window of 200 ns (including the original hit).

Two variables, which are important for the construction of the first level cascade filter (see section 7.2), are calculated by *c_first* :

- N_{early}: The number of early hits is defined as the number of hits with a time: $t'_{\mathrm{residual}} - t_{\mathrm{max}} <$ -200 ns. The time t_{max} is the time-residual with the largest number of hits arriving within the next 200 ns (see figure 5.1.1). For a cascade one expects only a small number of early hits, as they are not consistent with the cascade hypothesis.

- $N_{\mathrm{dir}}^{0:200}$: The number of hits, $N_{\mathrm{dir}}^{0:200}$, in the 200 ns time-window after the estimated vertex time t_v is an efficient variable for separating background from signal.

5.2 Vertex Position Reconstruction

The position and time of a cascade vertex are reconstructed by maximizing a likelihood function which is based on the information of the time of the hits. The approach of using a likelihood reconstruction method has so far been the most successful, because it allows to include the multiple scattering probability of photons in ice in a rather natural way.

The effects of photon scattering on the arrival time distribution of the photons will be discussed first. Here the time residual (5.1.1) becomes important again. For distances shorter than the effective scattering length of photons in ice (see section 4.5), the most probable time residual is very close to zero. However, for distances considerably larger than the effective scattering length, the most probable time residual moves to later times. The distributions of the time residuals, as obtained from a photon propagation simulation [96], are shown in figure 5.2.1 for two different distances (d_i = 20 and 100 m).

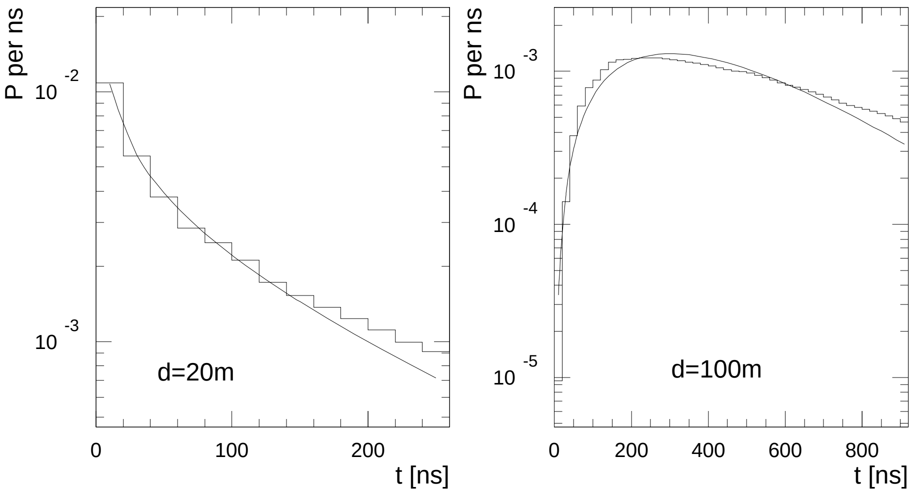

Figure 5.2.1: Arrival time probability density distribution as a function of the time residual, $p(d, t_{\mathrm{residual}})$, for 20 m (left) and 100 m (right). The histogram is obtained from the photon Monte Carlo simulation [96], while the smooth line is the parameterization (5.2.1) [100].

A convenient parameterization of the normalized probability density function (PDF) for observing a time residual t as a function of the distance, has been proposed in [129] and is since then called *Pandel* function:

$$p(d,t) = \frac{\tau^{-(d/\lambda)} t^{(d/\lambda - 1)} e^{-(t/\tau + c_{\mathrm{ice}} t / X_0 + d/X_0)}}{\Gamma(d/\lambda)}, \tag{5.2.1}$$

where the parameter X_0 can be interpreted as an absorption length, λ as a scattering length and τ as a scattering time. The values of these parameters are obtained by fitting equation (5.2.1) to a full photon Monte Carlo simulation [96] and they are: $\lambda = 47$ m, $\tau = 98$ ns, $X_0 = 450$ m. A similar parameterization, however with different values for λ, τ and X_0 is also used for the reconstruction of muons in AMANDA [169]. Equation (5.2.1) neglects the dependence on the direction of the cascade and orientation of the OM (see [100] for further discussion of this approximation). The parameterization (5.2.1) is compared to the Monte-Carlo simulation of the distribution of residual times in figure 5.2.1. As can be seen, the parameterization is only an approximate description of the MC distribution.

The parameterization (5.2.1) does not take into account the effects of PMT and electronic jitter. One assumes that they can be characterized by a Gaussian smearing with width σ_{jitter}. The analytical convolution of the parameterization (5.2.1) with a Gaussian distribution has only recently been achieved and was not available for this work. A numerical integration turns out to be too slow to be applicable in most of the realistic situations. Hence an approximate solution was proposed for the muon reconstruction in [169] and was also adopted for cascade reconstruction. One constructs a *patched* PDF, $p^{\text{patched}}(d,t)$:

$$p^{\text{patched}}(d,t) = \begin{cases} G(t) & \text{for} \quad t < 0 \\ P(t) & \text{for} \quad 0 < t < \sqrt{2\pi} \cdot \sigma_{\text{jitter}} \\ p(d,t) & \text{for} \quad t > \sqrt{2\pi} \cdot \sigma_{\text{jitter}} \end{cases} . \tag{5.2.2}$$

$G(t)$ represents a Gauss function with width σ_{jitter} and $P(t)$ is a polynomial function of order two. The parameters of P(t) as well as the normalization of $G(t)$ are chosen such that $p^{\text{patched}}(d,t)$ is continuous, differentiable and normalized to unity.

Having a parameterization of the PDF for observation of a time-residual as a function of distance available, a likelihood function can be constructed,

$$\mathcal{L} = \prod_{i=1}^{\text{all hits}} p^{\text{patched}}(d,t), \qquad L = \frac{-log(\mathcal{L})}{N_{\text{hits}} - N_{\text{free}}}. \tag{5.2.3}$$

L is defined in analogy to a reduced χ^2 as the function to be minimized. $N_{\text{free}} = 4$ is the number of free parameters (x, y, z and t).

One should note that by using (5.2.1) the explicit assumption is made, that each photo-electron can be resolved. Therefore this likelihood function is called the *1-p.e. time likelihood.* Alternatively, it is possible to construct a likelihood for the case where several photo-electrons contribute to a hit. Assuming that the number of contributing photo-electrons in a hit, n, can be measured, one can construct the PDF for time delays as a function of distance:

$$p_n(d,t) = np(d,t) \left(\int_t^{\infty} p(d,t')dt' \right)^{n-1} . \tag{5.2.4}$$

Here, the integral represents the probability, that one photo-electrons arrive with a time delay larger than t. In analogy to the 1-p.e. time likelihood a multi-p.e. (mpe) time-likelihood can be constructed through equation (5.2.3). As an estimate of the number of registered photo-electrons, the amplitude of the pulse is used.

The vertex position and time is reconstructed by minimizing the likelihood function L. This minimizing procedure requires as seed an estimate of the vertex location, for which the *c_first* algorithm is used.

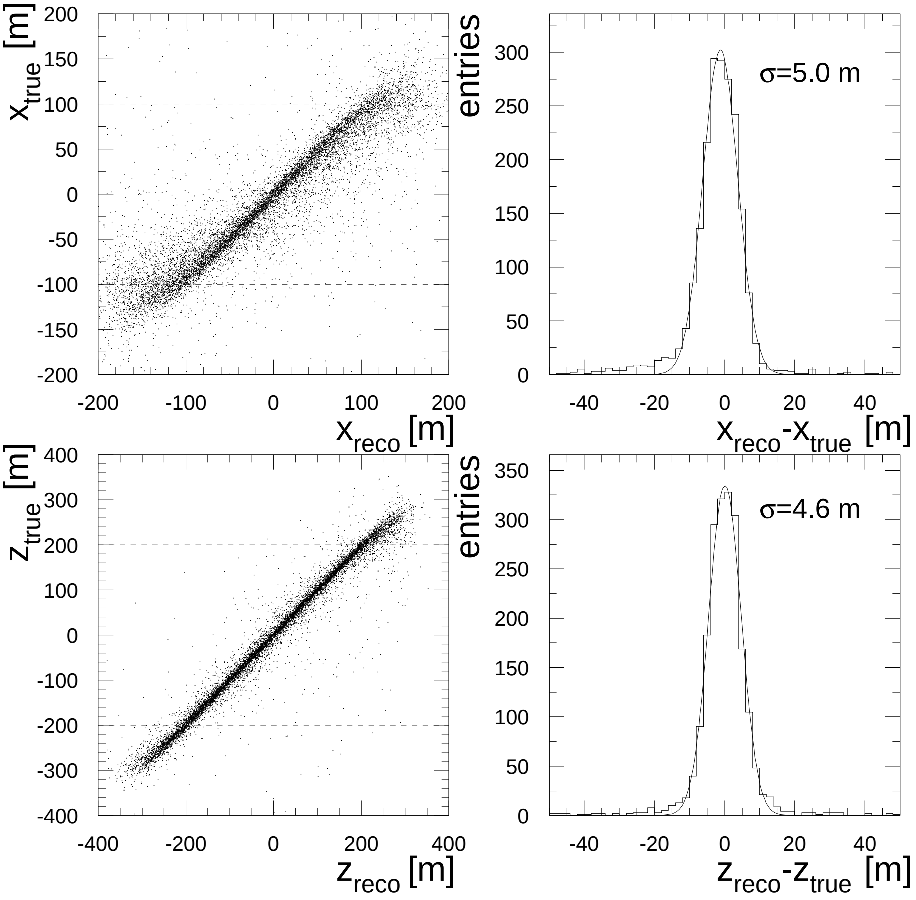

Figure 5.2.2: Left: reconstructed versus generated vertex coordinates for 1-TeV cascades as obtained for the mpe-likelihood method. The dotted lines indicate approximate borders of AMANDA-II. Right: Distribution of the difference between reconstructed and generated vertex coordinates, obtained for cascades inside a fiducial volume roughly of the same dimensions as AMANDA-II (a cylinder 100 m in radius and 400 m height) and fitted with a Gauss-function.

Figure 5.2.2 shows the result of the vertex reconstruction for 1 TeV cascades using the mpe-time likelihood method. The reconstructed y coordinate of the vertex behaves similar to the reconstructed x coordinate and is therefore not shown. The resolution for cascades inside the AMANDA-II detector is about 5 m for the x and y coordinate, and slightly better for the vertical z coordinate, due to the smaller OM spacing in the vertical direction. In general, the mpe-likelihood method produces slightly better position resolution than the 1-p.e. likelihood method.

The reconstruction performance, as obtained from Monte Carlo simulation can be verified with the help of *in-situ* light sources (see section 4.3). A YAG laser at the surface

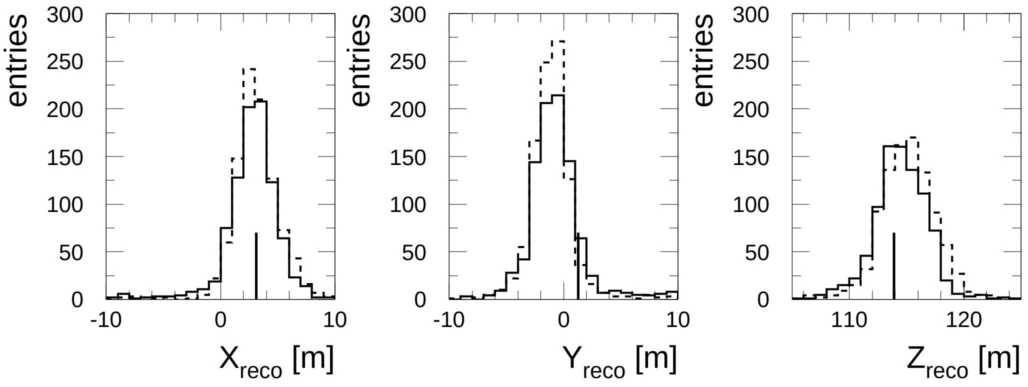

Figure 5.2.3: Reconstructed coordinates of a single YAG-laser light source in AMANDA-II. The full line represents the experimental data and the dashed line a Monte Carlo simulation of the corresponding light source. The vertical bar indicates the true position (which is known with 1 m accuracy). The 1-p.e. time likelihood-method has been used for reconstruction.

operating at 532 nm can be used to inject light pulses into optical fibers connected to nylon diffuser balls located in the close vicinity of most OMs in the detector. The position of the diffuser balls is known with approximately 1 m accuracy [17]. The light output of a diffuser ball is assumed to be isotropic.

The resulting distributions of the reconstructed x, y and z coordinates of a single diffuser ball are shown in figure 5.2.3. The agreement between experiment and the Monte Carlo simulation is reasonably good. The distributions are narrower than seen in figure 5.2.2, where the difference arises from different optical ice properties at 532 nm compared to Cherenkov light and due to the fact that the result of the reconstruction is shown for a single specific emitter location. Systematic shifts between the true and the reconstructed position are smaller than the vertex position resolution for 1-TeV cascades.

5.3 Energy Reconstruction

The energy reconstruction of cascade-like events is also based on a maximum likelihood method, where the likelihood is given by the probability of observing a certain hit-pattern.

In a first step one needs to find a parameterization for the hit-probability, which is the probability to observe a hit at a certain distance from the cascade of an assumed energy and direction. For an isotropically emitting point-like cascade, and distance larger than the effective scattering length, $d \gg \lambda_{\mathrm{scatt}}^{\mathrm{eff}}$ (see section 4.5), one finds a simple expression for the expected number of photo-electrons as a function of distance [20],

$$\mu \approx I_0 \frac{E}{d} e^{-d/\lambda_{\mathrm{attn}}}, \tag{5.3.1}$$

where $\lambda_{\mathrm{attn}} = \sqrt{\lambda_{\mathrm{scatt}}^{\mathrm{eff}} \lambda_{\mathrm{absorb}}/3}$ is the attenuation length (see section 4.5). At Cherenkov wavelengths the attenuation length is of the order of $\sim$ 29 m. Furthermore, the fact was used that the intensity scales linearly with the cascade energy. I_0 is a normalization constant which, in principle, is also dependent on the direction of the cascade and the orientation of the OM.

The expression for the average photon intensity at a given distance away from the cascade, allows to construct the probability for observing a hit, $P_{\text{hit}}^{\text{casc}}$:

$$P_{\text{hit}}^{\text{casc}} = 1 - P_{\text{nohit}}^{\text{casc}} \approx 1 - e^{-\mu}. \tag{5.3.2}$$

This expression was fitted to Monte Carlo simulations, averaging over angle and OM orientation. For the normalization constant one obtains $I_0 = 1.4\ \text{GeV}^{-1}\ \text{m}$. The functional dependence of equation (5.3.2) is illustrated in figure 5.3.1 (left) for energies ranging from 100 GeV to 1 PeV.

Basic characteristics of the energy reconstruction method are direct consequences of the exponential attenuation of the mean photo-electron expectation of (5.3.1). To see this, we define the radius R of the light field of a cascade with a given energy E, as the distance for which $\mu(R, E) = 1$. For $R \gg \lambda_{\text{attn}}$ one gets an approximate scaling law between the radius R and the energy E:

$$R \approx \lambda_{\text{attn}} \ln(E) + C_{\lambda_{\text{attn}}} \Longleftrightarrow \ln(E) \approx \lambda_{\text{attn}}^{-1}(R - C_{\lambda_{\text{attn}}}), \tag{5.3.3}$$

where $C_{\lambda_{\text{attn}}}$ is a constant depending on λ_{attn}. As illustrated in figure 5.3.1 (right), there is a partial ambiguity between the attenuation length and the energy of the cascade. The attenuation length was varied by ±4 m around its nominal value of 29 m, and the energy was adjusted such that $R(E', \lambda \pm 4\text{m}) = R(E, \lambda)$. The resulting hit probabilities are very similar and hence any uncertainties in the value for the attenuation length result in an uncertainty in the linear scale of the logarithm of the true energy.

In order to obtain a realistic hit probability, one needs to add the probability for observing a noise hit,

$$P_{\text{hit}} = 1 - P_{\text{nohit}} = P_{\text{hit}}^{\text{casc}} + P_{\text{noise}} - P_{\text{hit}}^{\text{casc}} P_{\text{noise}}. \tag{5.3.4}$$

A likelihood function can now be constructed as:

$$\mathcal{L} = \prod_{\text{all hit OMs}} P_{\text{hit}}(E, d) \prod_{\text{all un-hit OMs}} P_{\text{nohit}}(E, d);$$

$$L = \frac{-\mathcal{L}}{N_{\text{OM}} - N_{\text{free}}}. \tag{5.3.5}$$

Here, N_{OM} is the number of active OMs. Minimizing L provides an estimate of the energy. In principle, one can also use this likelihood to reconstruct the vertex. However the resulting vertex resolution is considerably worse than the one obtained from a time likelihood reconstruction. The energy reconstruction is therefore seeded by the output of the vertex reconstruction.

Figure 5.3.2 shows the performance of the energy reconstruction for cascades of five different generated energies ($10^2, 10^3, 10^4, 10^5$ and 10^6 GeV). The left plot shows the distribution of reconstructed energies. The energy resulting from the fit was rescaled with an empirical correction factor of $\log(E_{\text{reco}}/\text{GeV}) = 1.2 \cdot \log(E_{\text{fit}/\text{GeV}}) - 0.5$ to account for the fact that the simulation assumed a different attenuation length than implemented in

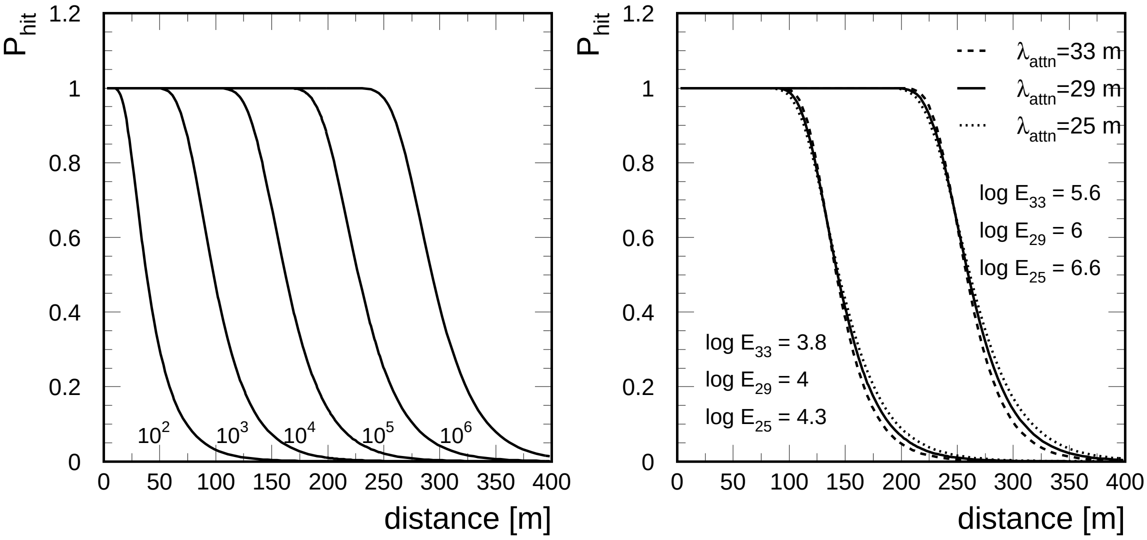

Figure 5.3.1: Hit probability, $P_{\rm hit}^{\rm casc}$, as a function of distance for cascade energies ranging from 100 GeV to 1 PeV (left). Influence of $\lambda_{\rm attn}$ on hit probability (right). Energy, $E_{\lambda'}$, was adjusted so that the 1pe radius, R, matches independent of the attenuation length $\lambda'_{\rm attn}$: $R(E_{\lambda'}, \lambda') = R(E_\lambda, \lambda)$

the reconstruction. The vertex is restricted to lie inside a fiducial volume, a cylinder of radius 100 m and height 400 m. The distributions where fitted with a Gauss function. The resulting width is used as a measure of the energy resolution. Figure 5.3.2 (right) shows the energy resolution as a function of the cascade energy for three cases: All cascades which trigger the detector, those which pass an additional cut on the value of the likelihood function of the vertex fit (the cut $L_{\rm vertex} < 7.1$ is also used during further analysis) and those which additionally have a position within the fiducial volume of AMANDA. As can be seen, application of the cuts improves the energy resolution in particular at higher energies. Without application of cuts the energy resolution mainly broadens due to events with miss-reconstructed vertices. For cascades of increasing energies the energy resolution becomes worse. This effect is related to the increasing size of the light field when compared to the limited size of the AMANDA-II detector.

The distribution $(\log E_{\rm reco} - \log E_{\rm true})$ can be described by a Gauss function, a fact which can be understood from equation 5.3.3. By minimizing $L_{\rm energy}$, one effectively measures the radius R, since hits from that distance region mainly determine the value of the likelihood function. Any uncertainty in R translates into an uncertainty in $\log E$. Assuming that the measurement of the radius R can only be known with the resolution of the vertex position, $\Delta R \approx 5$ m, one obtains a lower limit for the energy resolution: $\Delta \log E \approx \frac{\Delta R}{\lambda_{\rm attn} \cdot \ln 10} \approx 0.08$.

Again, one can use *in-situ* light sources to verify the performance of the reconstruction. The OMs on string 18 are equipped with ultraviolet LEDs, which can be operated at various intensities. LEDs working at 370 nm represent a Cherenkov light emitting point-like source fairly well. Figure 5.3.3 shows the distribution of reconstructed energies for an ultraviolet LED operated at two intensities, I_1 and I_2. The resolution of the corresponding

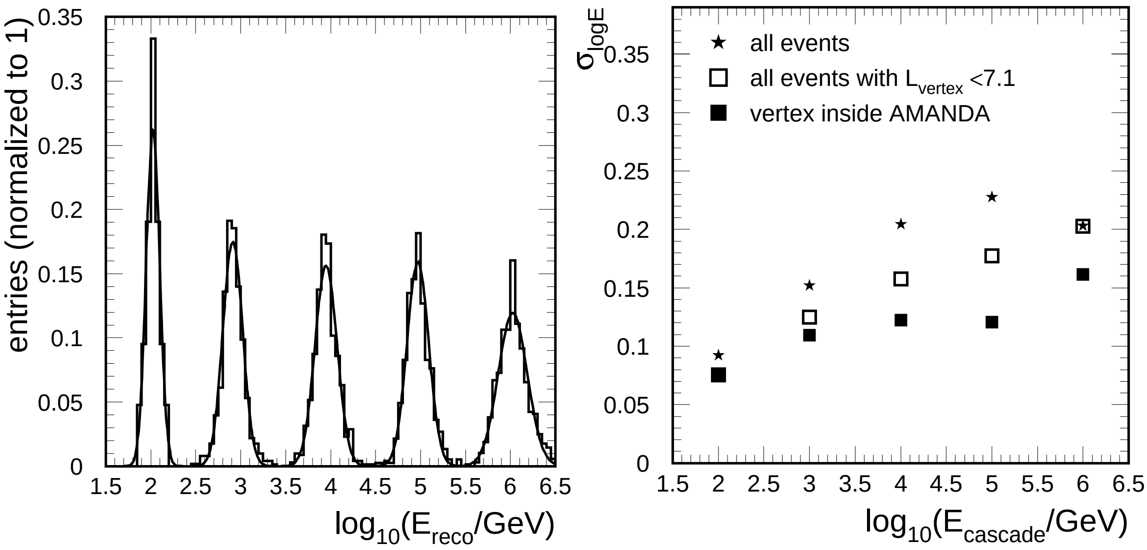

Figure 5.3.2: Left: distributions of reconstructed energies for mono-energetically simulated cascades of energies $10^2, 10^3, 10^4, 10^5$ and 10^6 GeV. The vertex is restricted to lie inside a fiducial volume, a cylinder of 100 m radius and 400 m height containing the instrumented volume of AMANDA-II. Right: resolution of the energy reconstruction as a function of the cascade energy. The resolution is shown separately for all cascades which trigger the detector, those passing an additional cut on the value of the likelihood function resulting from the vertex fit and those which have a position within the fiducial volume of AMANDA.

LED energies is better than for cascades of similar energies, since the spatial resolution of the LED due to its fixed location is better. Note also that here the energy scale is linear.

While the absolute intensities can only be estimated very vaguely, the relative intensities for a given LED can be estimated by counting the relative number of photo-electrons observed by the surrounding OMs. In order to reduce the systematic error of a non-linear ADC response, one uses OMs which are read out optically so that photo-electrons are likely to be resolved. Furthermore only OMs at intermediate distances from the LED are chosen such that the average hit multiplicity is low (around 1) but such that the hit rate is still significantly above the noise rate. With the method explained above one can estimate the relative intensities to, $I_2/I_1 = 2.4 \pm 0.4$, where the error comes from systematic limitations of the method. This estimate of the relative intensity is consistent with the ratio of reconstructed energies. An analysis for a set of LEDs at different locations has been performed, with a similar result [101]. The currently available LEDs, however, can only be operated with intensities equivalent to cascade energies of a few TeV.

5.4 Direction Reconstruction

For reconstruction of the direction of the cascade a parameterization of the average number of photon-electrons can be used, which is similar to equation (5.3.1) [155],

$$\mu \approx g(\cos\psi) I_0 \frac{E}{d} e^{-d/\lambda_{\rm attn}}, \tag{5.4.1}$$

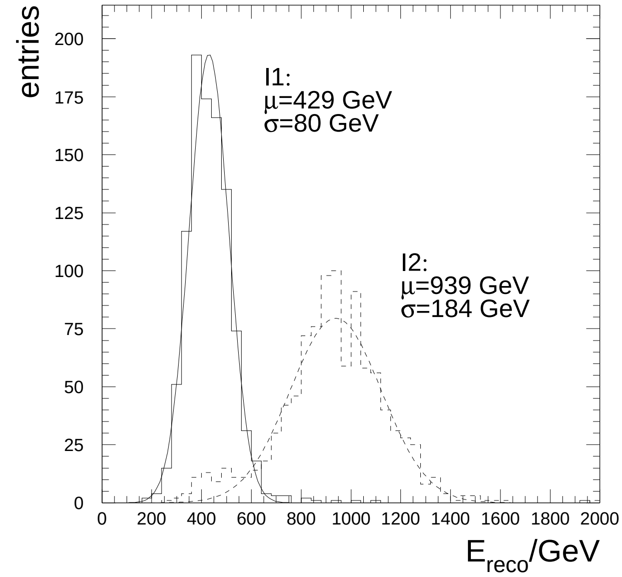

Figure 5.3.3: Distribution of reconstructed energies for two runs of different intensity of an ultraviolet LED. The smooth lines represent fitted Gauss-functions, with mean μ and width σ. The ratio of mean reconstructed energies is consistent with the ratio of relative LED intensities (see text for details).

where $g(\cos\psi)$ is a function of ψ, the angle between the cascade direction and the vector joining the cascade vertex and the OM. This function can be fitted to Monte Carlo simulations using Legendre polynomials. The resolution of the zenith angle obtained with this method is $30^\circ - 40^\circ$. Note that the direction reconstructed with this method is not used during this work.

Chapter 6

Data Samples

6.1 Experimental Data

The analysis presented in this work is based on the data obtained in the first year of operation of the completed AMANDA-II detector. The data used was collected between February and November 2000. A total of 1.3×10^9 events were recorded. After correcting for dead time (17 %), one is left with 197 days of lifetime. The timing calibration constants where released in February 2001, marking the starting date for analysis of the AMANDA-II data.

6.2 Simulation of Background and Signal Events

An overview of the simulation chain for signal and background events is given in figure 6.2.1. Various programs are involved in the simulation chain which will be described in this section. Common to all event classes is only the final detector simulation.

6.2.1 Generation of Atmospheric Muon Events

Muons produced in air showers were simulated using the CORSIKA (v6.020) program [77]. The model chosen for hadronic interactions within CORSIKA was QGSJET01. Primary cosmic rays where sampled according to a flux parameterization of Wiebel-Sooth [167].

In a next step, the air shower events were distributed over a large surface area using CORAMA [151]. To increase the simulation speed, the events were *over-sampled*. Each CORSIKA event was used 100 times, but randomly shifting the primary vertex coordinate of the interaction point in a horizontal plane, as well as randomly changing the azimuthal incident angle of the air shower. Because of the large data reduction involved in a typical AMANDA analysis, such an over-sampling does not lead to significant statistical correlation between events. Muons at the surface were then propagated through the ice using the program MMC [40]. All relevant energy losses were thereby taken into account. Secondary particles above a threshold of 0.5 GeV were added to the event record (see section 3.5.2).

The simulation of background is a computationally intensive task. Only 6.1 days of lifetime of regularly simulated background events were available at the beginning of this

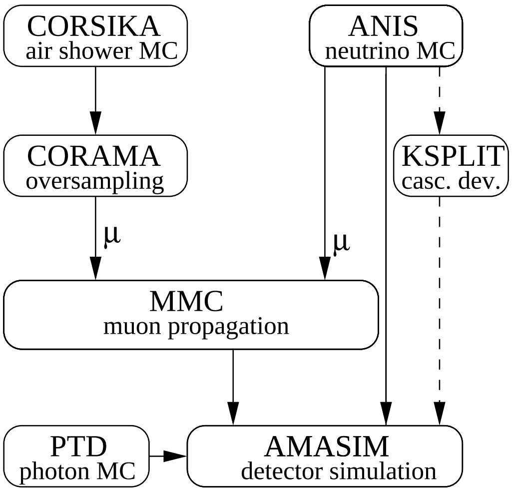

Figure 6.2.1: Overview of the simulation chain. See the text for details.

analysis. For this reason, a highly optimized simulation chain, which is described in the next section, has been used to simulate a significantly larger statistics of background events.

6.2.2 Optimized Simulation Chain for Atmospheric Muons

The rate of atmospheric muon background events decreases fast with increasing energies. Hence, in order to obtain a significant statistics of events at high energies, a large simulated lifetime is necessary. For this reason, an optimized MC simulation chain was developed, which allowed to generate a significantly larger lifetime of atmospheric muons, than the 197 days of experimental lifetime of the year 2000.

The optimized background MC simulation chain relies on the fact, that after application of a filter to select neutrino induced cascades, the background is dominated by energetic secondary particles radiated by atmospheric muons (see section 7.3.2). Hence only muon events with a large stochastic energy loss need to be simulated. Details of the simulation chain are described in appendix A. The validity of the resulting MC simulation is restricted by a lower energy bound. Two MC simulation samples exist, to be used only after application of the first level selection criteria (see section 7.2) and in connection with a cut on the reconstructed energy: $E_{\text{reco}} \geq 1.25$ TeV and $E_{\text{reco}} \geq 5$ TeV. The available lifetime of the first sample is about 120 days, while the sample with the higher threshold energy correspond to approximately 800 days of lifetime. The available statistics of the various samples will be summarized in more detail in section 7.6.1. The generation of the data samples represent about 12 years of CPU time (assuming GHz CPUs). Figure 6.2.2 shows the distributions of reconstructed energies of the optimized MC event samples and of the regular MC sample. The lower plot shows the distributions after normalization of event rates in the overlap regions of the optimized MC event samples to the regular MC.

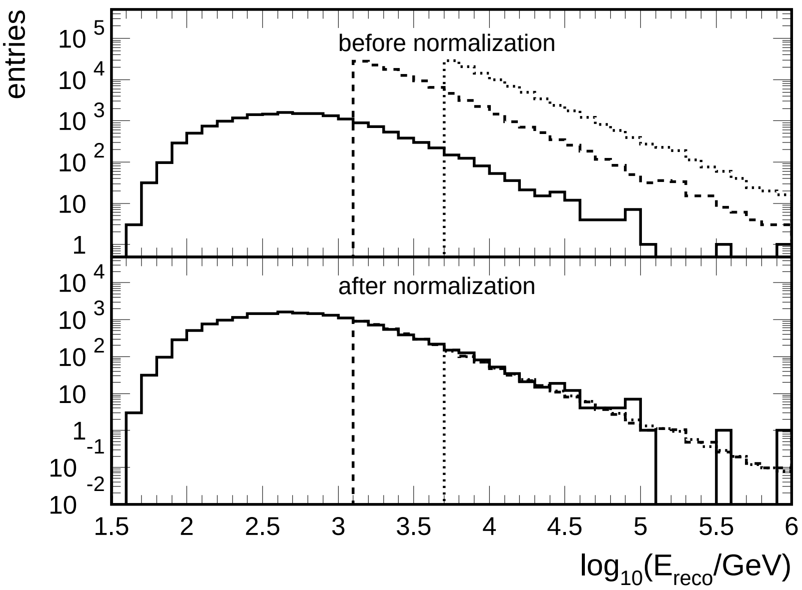

Figure 6.2.2: Reconstructed energies of the regular (full line) as well as the two optimized atmospheric muon background MC samples (dashed line: $E_{\text{reco}} \geq 1.25$ TeV, dotted line: $E_{\text{reco}} \geq 5$ TeV)

6.2.3 The Neutrino Event Generator ANIS

The ANIS (**A**ll **N**eutrino **I**nteraction **S**imulation) program was used for the simulation of neutrino induced events. ANIS is a Monte Carlo event generator, which generates neutrinos of all flavors, propagates them through the earth and in a last step simulates a neutrino interaction within a specified volume around the detector [104]. The aim of the program is to provide a tool for precise simulation of neutrino events of all flavors in the energy range of interest for high energy neutrino telescopes.

The currently implemented interaction channels include CC, NC as well as resonant $\bar{\nu}_e e^-$-scattering. The cross-section data for CC and NC reactions are provided through pre-calculated external tables. The total cross-section is obtained through interpolation. The final state depends on the flavor of the interacting neutrino, the type of the reaction as well as on the variables x and y of the interaction (see section 3.1.1). Large sets of x and y have been generated and are stored in tables, from which they are randomly sampled from during generation of neutrino events. The use of pre-calculated tables makes the program fast and independent of other packages. The cross-section data has been calculated up to 10^{12} GeV, using CTEQ5 structure functions [109]. The behavior of the total cross-section is shown in figure 3.1.1.

Primary neutrinos are randomly generated on the surface of the earth with an energy spectrum $\phi_\nu(E) \propto E^{-1}$ and are then propagated to the detector. In interactions with matter they are either absorbed (CC case) or regenerated at lower energies (NC case). In the special case of CC $\nu_\tau N$-interaction a short-living τ-lepton is produced. It propagates in matter, loosing part of its energy, and finally decays giving rise to secondary ν_τ and, in ~ 17 % of the cases, to secondary ν_μ or ν_e. The τ-decay in ANIS has been simulated using TAUOLA [91]. The practically 100 % polarization of high energy τ's was taken into account. Again, the previously generated decays of polarized τ-leptons are stored in tables, which are then sampled from by ANIS. Regenerated neutrinos are assumed to be emitted parallel to the direction of the primary neutrino. This is justified, since regeneration effects become significant only at very high energies, where the accumulated deflection angle is generally smaller than the telescope angular resolution. The density profile of the earth used for neutrino propagation is chosen according to the Preliminary Earth Model [47].

Once the detection volume is reached, a final vertex is sampled along the neutrino trajectory within the detection volume. In the case of a CC $\nu_\mu N$-interaction, ANIS correctly simulates the muon scattering angle. Along with the full event three weights are stored: a normalization constant, a weight for the atmospheric flux [113], as well as a weight proportional to the total cross-section of the neutrino interaction.

Event rates for atmospheric and various extraterrestrial neutrino spectra are obtained by applying the appropriate weights to the events. This last step is done by a user defined energy dependent weight function during analysis of the events in PAW [86], ROOT [34] or any other analysis programs.

The simulated events used for this thesis have vertex positions distributed in a cylindrical volume of 300 m radius and 600 m height. Neutrinos of all flavors (ν_e, ν_μ and ν_τ) have been simulated in an energy range from 100 GeV to 100 PeV. In case of ν_μ, all resulting muons are further propagated using MMC [40].

6.2.4 Detector Simulation

The final step is the simulation of the detector response using the program AMASIM [83]. The photon intensity and time distribution for each OM is sampled from pre-calculated tables, which where generated using the program PTD [96]. Then the hardware response is simulated, incorporating hardware artefacts such as individual PMT pulse shapes and discriminator thresholds effects.

Optical properties of the ice are included in the generation of the photon propagation tables. Throughout this work, two sets of tables have been used, which model the current knowledge of the optical ice properties. The KGM ice-model is based on direct measurements described in section 4.5. The other so called MAM ice-model is based on an iterative adjustment of the ice properties, until the distribution of time-residuals from well reconstructed muon tracks match the experimentally observed [79]. The MAM ice-model results on average in a 15 % shorter absorption length than implemented in the KGM ice-model. If not explicity mentioned otherwise, the simulation used in this work was done with the MAM ice-model.

The information about the ice structures are included in AMASIM. Depending on the position of the receiving OM, a particular photon propagation table is chosen. This is only a rough approximation, since the assumed ice properties for the photon propagation are those of the position of the receiving OM. However, photons emitted at large distances travel through ice layers with optical parameters different to the layer corresponding to the OM. Consequences of this approximation will be described in appendix B.

AMASIM treats all cascades as point-like light emitters. Further, the simulated light intensity is linearly dependent on the energy, thereby neglecting all fluctuations in the cascade development. To obtain a more realistic simulation of cascades, a program called *ksplit* has been developed. The energy of hadronic final states are rescaled according to the non-linear energy dependence of equation (3.4.6) using parameters of table 3.4.1. Fluctuations of the light yield are incorporated in a similar way, according to the parameterization (3.4.7). A realistic longitudinal cascade development is obtained by distributing the energy of the cascade longitudinally according to equation 3.4.2. Part of the available signal samples has been generated using *ksplit*.

Chapter 7

Data Analysis

The aim of this analysis is the detection of an astrophysical flux of high energy neutrinos through observation of neutrino-induced cascades. Table 7.0.1 summarizes the trigger rate of the experiment, the atmospheric muon background simulation, atmospheric ν_e[1] as well the trigger rate of a hypothetical flux of astrophysical ν_e given by $E^2\phi(E) = 10^{-6}$ GeV s^{-1} sr^{-1} cm^{-2}. The flux of astrophysical neutrinos was chosen in rough accordance with experimental upper limits. The rate of atmospheric muons is about 5×10^6 larger than that of the signal expectation. Clearly, to reach a high sensitivity for astrophysical neutrinos, a reduction of the background is essential. The various steps involved in data reduction will be described in this chapter.

experiment	background MC	atmospheric ν_e	E^{-2} signal ν_e
57 Hz	47 Hz	$1.2 \cdot 10^{-5}$	$1.1 \cdot 10^{-5}$

Table 7.0.1: Trigger rate of the experiment, the atmospheric muon background MC, atmospheric ν_e MC, and a hypothetical flux of ν_e following $E^2\phi(E) = 10^{-6}$ GeV s^{-1} sr^{-1} cm^{-2}.

The analysis chain is summarized in figure 7.0.1. Data analysis begins with a quality selection of files, OMs and hits, a procedure called preprocessing. All preprocessing steps are applied to both experimental and simulated data, with the exception of the file selection and the cross-talk filters which is only done for experimental data. Preprocessing is followed by a first level event filter, which is necessary to reduce the data set to allow further, more CPU intensive reconstructions and analysis. The first level filter consists of two cuts. A second level filter uses the results of the vertex and energy reconstructions to further reduce the data set. The main aim of the second level filter, which consists of four cuts, is to assure that only well reconstructed events pass the filter. The final selection criterion, described in section 7.4, is based on a cut on a Bayesian discriminator variable in connection with a cut on the reconstructed energy. It was optimized to yield optimal sensitivity to a hypothetical flux of astrophysical neutrinos. The programs and command options used for filtering and reconstruction of the data are summarized in appendix E.

All selection criteria were developed using simulated data. Additionally a 20 % subsample of the experimental data, consisting of every fifth data file, was used to verify

---

[1] Unless not otherwise mentioned, ν_e refers to the sum of neutrinos and antineutrinos.

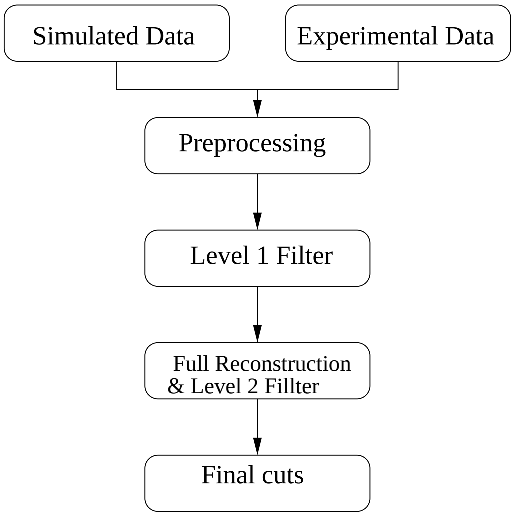

Figure 7.0.1: Illustration of processing and analysis chain.

properties of the filter. In accordance with the AMANDA collaboration rules, the remaining experimental data was left untouched until the analysis was finalized and approved by the collaboration. This procedure was introduced in order to minimize a possible bias from tuning the cuts to remove individual events near the signal region.

7.1 Preprocessing

A first step in the processing of the data was the application of a data filter, to assure that the data has the necessary quality for later analysis. This filter is not specific to the analysis presented here and consists of the following steps [140]:

File selection: A file (roughly 10 minutes long) is the smallest available data entity. The performance of all OMs in a file are monitored through their noise rate. A file is rejected from the analysis if the number of malfunctioning OMs in that file is larger than 170. About 8 % of the data is thereby rejected.

OM selection: OMs which were not working, or working very unstable throughout the year, were excluded from the analysis. A list of 121 OMs are excluded from the analysis. For three periods of the year, a shorter list of additional OMs had been excluded from the analysis.

Retriggering: After OM exclusion, the hardware multiplicity trigger was reinforced through application of a software trigger. This was done to allow a more accurate simulation of the trigger condition.

Further processing focused on the hits of events. Time and amplitude information of the hits were calibrated. Hits, which do not fulfill certain criteria, were not used during reconstruction. This process is called *hit-cleaning*. The following selection criteria where applied:

Timing and Amplitude: The leading edge of the hit had to be within a time window of 6.5 μs. The time over threshold of the TDC discriminator (TOT) is used to filter out hits due to electronic noise and cross-talk. For OMs read out through optical fibers (electrical cable), the TOT had to be between 5 ns (75 ns) and 2000 ns. The calibrated amplitude had to be larger than 0.1 p.e..

Isolation: Hits had to have at least one neighboring hit occurring within ±500 ns time and a distance not further than 100 m away. This isolation criterion is effective in removing noise hits.

Cross-Talk: OMs on strings 5-10, which use twisted quad cable for pulse transmission, where identified to suffer the strongest of electronic cross-talk. A dedicated filter was developed to remove such cross-talk hits [155]. The filter is based on TOT and amplitude information of the hits, as well as on a cross-talk probability map for pairs of cross-talk emitter and receiver amplitudes. The cross-talk filter was only applied after the first level filter, since it was not available before the raw data was processed. Hence, only the likelihood reconstructions are affected by this additional cleaning step.

7.2 A First Level Filter

The large amount of background makes early reduction of experimental data mandatory. The first level filter aims at reducing the experimental data set to about 2-3 % of its initial size. The desired passing rate is mainly determined by the computational requirements of further likelihood reconstructions. Additionally, the filter is also operated at the South Pole as the first level online filter of the cascade data stream [28]. Because of the limited bandwidth, only filtered data are transmitted via satellite to the northern hemisphere.

The *c_first* first-guess algorithm (described in section 5.1) returns two variables, $N_{\mathrm{dir}}^{0:200}$ and N_{early}, which are used for discriminating signal from background. N_{early} represents the number of hits with time-residuals too small to be consistent with hits from a cascade. Early hits in cascade events are either due to random noise, or arise from mis-reconstruction of the vertex time and position. The number of early hits is larger for track-like events, due to the relativistic motion of the underlying muon. Muons propagate faster than light in ice, so that early hits can originate from muons emitting photons either significantly earlier or later than the estimated vertex time.

The discriminating potential of the variable N_{early} can be increased, when dividing N_{early} by the number of hits observed, N_{hits}. The ratio $N_{\mathrm{early}}/N_{\mathrm{hits}}$ has the advantage that it is only weakly dependent on the cascade energy, while N_{early} generally increases for higher cascade energies.

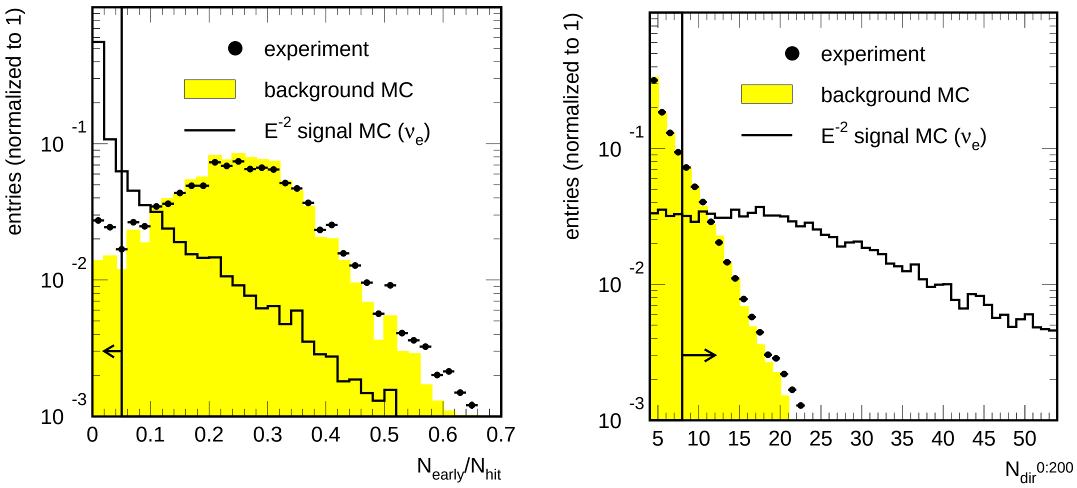

Figure 7.2.1: Normalized distribution of $N_{\text{early}}/N_{\text{hits}}$ (left) and $N_{\text{dir}}^{0:200}$ (right) used for the first level filter (for a definition see section 5.1). Shown are experimental data, atmospheric muon background MC and signal MC, assuming an AGN-like flux of ν_e falling as E^{-2}. No cuts have been applied. The line with the arrow indicates the position of the cuts.

Shown in figure 7.2.1 (left) are the distributions of $N_{\text{early}}/N_{\text{hits}}$ for experiment, atmospheric muon background MC and signal MC. The signal MC consists of a hypothetical flux of ν_e falling as E^{-2}. Due to the discrete nature of N_{early} and N_{hits}, the distribution of the ratio shows some specific structure common to experimental data and background MC simulation (for example at $N_{\text{early}}/N_{\text{hits}}$ =0.5). Only events fulfilling the condition $N_{\text{early}}/N_{\text{hits}} < 0.05$, pass the cut.

$N_{\text{dir}}^{0:200}$ represents the number of hits with a time-residual $0< t_{\text{resi}}<200$ ns. Since hits fulfilling this condition originate mainly from photons which have not or only slightly been scattered, they are often called *direct hits*. Figure 7.2.1 shows the distribution of $N_{\text{dir}}^{0:200}$ for experiment, atmospheric muon background MC and a flux of ν_e with an energy spectrum $\propto E^{-2}$. A cut $N_{\text{dir}}^{0:200} > 8$ is introduced.

Table 7.2.1 summarizes the fraction of triggered events, which pass the cuts of the first level filter. This fraction is larger for the atmospheric ν_e spectrum than for the harder energy spectrum falling as E^{-2}, since the filter is most effective for events inside or close to the detector. Because high energy events are able to trigger the detector even if the vertex position is located outside of AMANDA-II, the fraction of events passing the cuts is lower. If the vertex position is restricted to the fiducial volume of the detector (a cylinder of 100 m radius and 400 m height), the signal efficiency of the filter is 92 % and independent of the assumed energy spectrum.

7.3 A Second Level Filter

The data sample after application of cut # 1 and 2 of the first level filter is small enough to be fully reconstructed by likelihood minimization methods. The second level filter,

#	cut variable	experiment	background MC	atmospheric (ν_e)	E^{-2} signal (ν_e)
			Level 1		
1	N_{early}/N_{hit}	0.058	0.033	0.94	0.63
2	$N_{dir}^{0:200}$	0.030	0.016	0.89	0.57
			Level 2		
3	L_{vertex}	0.0027	0.0012	0.39	0.35
4	L_{energy}	0.0018	0.00077	0.35	0.26
5	z_{reco}	0.010	$5.9{\cdot}10^{-4}$	0.28	0.18
6	ρ_{reco}	$8.6{\cdot}10^{-4}$	$5.1{\cdot}10^{-4}$	0.26	0.15
			Final Level		
7	L_{s}	$9.7{\cdot}10^{-6}$	$4.8{\cdot}10^{-6}$	0.040	0.091

Table 7.2.1: Cumulative fraction of triggered events passing the cuts of this analysis. Values are given for experimental data, atmospheric muon background MC, atmospheric ν_e and a signal MC with an energy spectrum $\propto E^{-2}$. The cuts are grouped in levels which are described in this chapter.

consists of cuts (# 3-6), which mainly aim at improving the quality of the remaining events. As will be shown in section 7.3.2, the remaining atmospheric muon events, which pass cut # 3, become very cascade-like. It is this property which allows to optimize the background simulation chain for generation of a large statistics of simulated background events.

7.3.1 Vertex Position Reconstruction

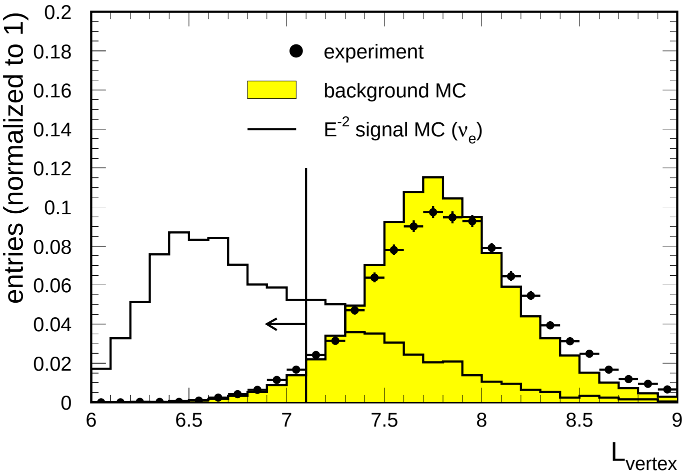

Figure 7.3.1: Normalized distribution of the value of the likelihood function of the vertex fit, L_{vertex}. Shown are experimental data, atmospheric muon background MC and signal MC, assuming an AGN-like flux of $\nu_e + \bar{\nu}_e$ falling as E^{-2}. Cut # 1 and 2 of the first level filter have been applied. The line with the arrow indicates the position of the cut.

Events passing the level 1 filter were reconstructed using the 1-p.e. likelihood reconstruction. The resulting vertex position was used as a seed for the multi-p.e. likelihood fit. Only the results of the multi-p.e. likelihood fit were used during further analysis.

A measure for the quality of the multi-p.e. likelihood reconstruction is the value of the likelihood function at its minimum, L_{vertex}. According to the definition (5.2.3), a well reconstructed position is represented by a small L_{vertex}. The distribution of L_{vertex} for experimental data, atmospheric muon background MC and ν_e signal MC is shown in figure 7.3.1. To reduce the background, a cut was introduced at $L_{\mathrm{vertex}} < 7.1$.

At this stage, this cut removes approximately 95 % of the experimental data, but also 32 % of the signal. The large fraction of removed signal events should not be a source of large concern, since the other high-level cuts remove a similar class of signal events, making the cut # 3 less severe (this can be seen from figure 7.4.2, where the distribution of L_{vertex} is shown after application of cut # 6). Since this cut variable will be used for further discrimination (see section 7.4), cut # 3 has a very small influence on the final result. The fraction of events passing this cut is given in table 7.2.1.

The vertex position resolution, after application of cut # 3, is about 4-5 m and nearly independent of the neutrino energy.

7.3.2 Energy Reconstruction

The energy of the remaining events are reconstructed according to the methods explained in section 5.3. As was shown there, the energy of a cascade can be reconstructed with a resolution, $\sigma_{\log E} \lesssim 0.2$.

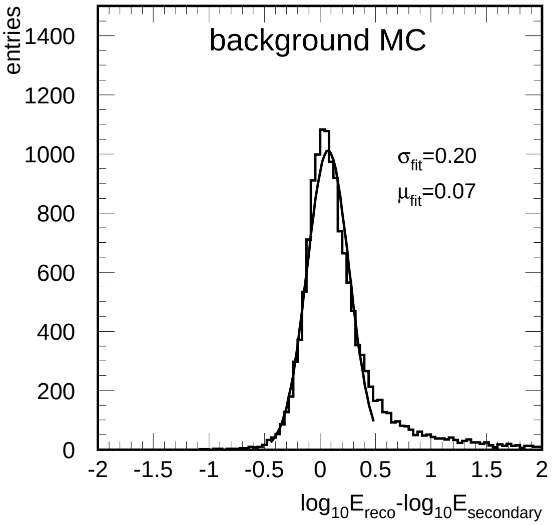

Figure 7.3.2: Energy resolution of the most energetic secondary cascade inside a cylindrical volume of 200 m radius and ± 250 m height. Shown is atmospheric muon background MC, which passed cut # 3.

One may wonder about the meaning of the reconstructed energy for the case of atmospheric muons. Atmospheric muon events, which pass cut # 3 have a very cascade-like appearance. The events are typically dominated by a single bright secondary cascade, being responsible for most of the hits in the event. For this reason, the reconstructed vertex position and energy of such events correspond to that of the brightest secondary particle. This is demonstrated in figure 7.3.2, showing the distribution of ($\log E_{\mathrm{reco}} - \log E_{\mathrm{secondary}}$), with $E_{\mathrm{secondary}}$ being the energy of the most energetic secondary particle inside a cylindrical volume (of 200 m radius and 500 m height) around the detector. The central peak of the distribution has been fitted with a Gauss function. For 90 % of the events the energy of the most energetic secondary particle can be well reconstructed (fulfilling $0.5 > \log E_{\mathrm{reco}} - \log E_{\mathrm{secondary}} > -0.5$). Note that the right tail of the distribution is not well described by the Gauss function. It corresponds to muon events without a clearly identified single energetic secondary particle.

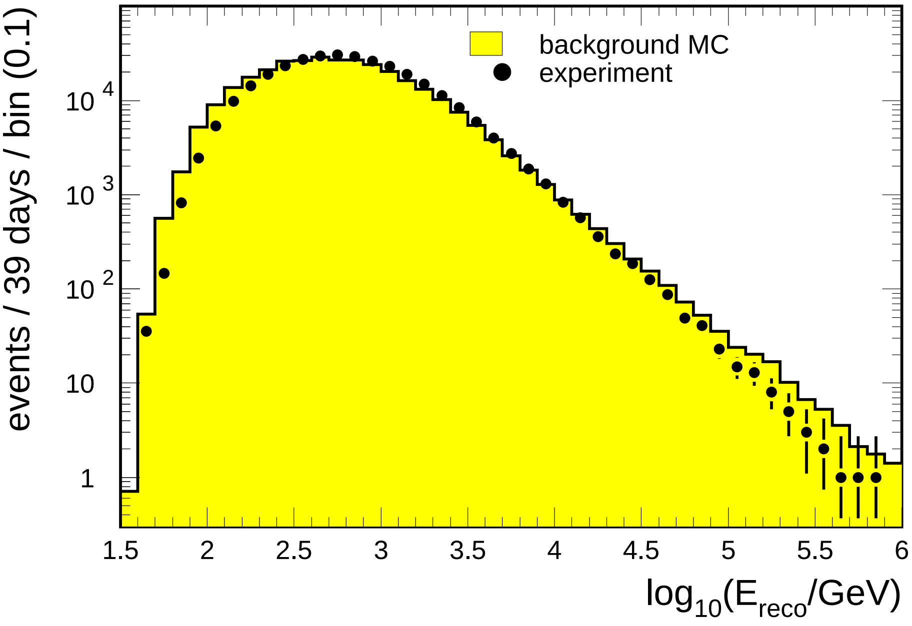

Figure 7.3.3: Energy spectrum of experimental data and atmospheric muons background simulation after cut # 3.

Figure 7.3.3 shows the energy spectrum of 20 % of the experimental data events (39.2 days of livetime), as well as that expected from the MC simulation. The distribution of the MC simulation was normalized to that of the experiment. It can be seen, that the central region can be described by the MC simulation, but that the tails of the distributions don't match very well. However, with application of further cuts, the discrepancies at high energies are reduced. The lower energies are of no further interest for this analysis and will hence not be considered anymore.

7.3.3 Cut on the Quality of the Energy Fit

In order to reduce the fraction of events with a mis-reconstructed energy, a cut on the value of the likelihood function at its minimum, L_{energy}, has been applied. Since the average

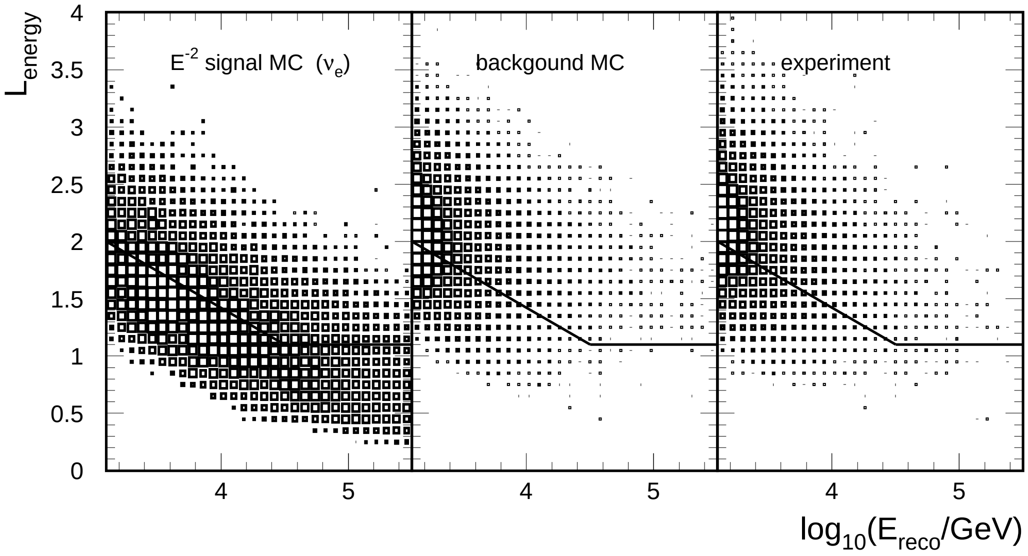

Figure 7.3.4: Likelihood value of energy reconstruction versus reconstructed energy

likelihood value depends on the reconstructed energy, this cut was set as a function of energy. Figure 7.3.4 shows the distribution of L_{energy} versus the reconstructed energy. Events below the indicated line survive the cut. The cut criterion is:

$$L_{\text{energy}} \leq \begin{cases} 1.1 & \text{for} \quad E_{\text{reco}} \geq 25 \text{ TeV} \\ 0.7 \cdot \log(E_{\text{reco}}/\text{GeV}) - 1.98 & \text{for} \quad E_{\text{reco}} < 25 \text{ TeV} \end{cases} \tag{7.3.1}$$

Note that the main aim of this cut is not the reduction of the background, but to assure that the remaining events were reconstructed correctly.

7.3.4 Position Cuts

The radial and vertical distance of the reconstructed vertex position relative to the center of the detector was constrained in order to increase the fraction of signal like events.

The z-coordinate of the vertex fit

The distribution of the z-coordinate, z_{reco}, of the reconstructed vertex is shown in figure 7.3.5. Here, a prominent problem appears. The distribution of the experimental data exhibits three distinct peaks, which are not reproduced by the background MC simulation. This problem, which has been known for many years, has appeared throughout various analyzes. Typically, on higher cut levels the distribution of the z-coordinate of the center of gravity of all hits shows the characteristic triple peak structure (and therefore is called COG-Z problem).

In the appendix B, it is shown that a likely explanation of the distinct triple peak structure is given by the vertical variation of optical ice properties. The regular detector simulation treats these variations only approximately. As shown in the appendix B, a

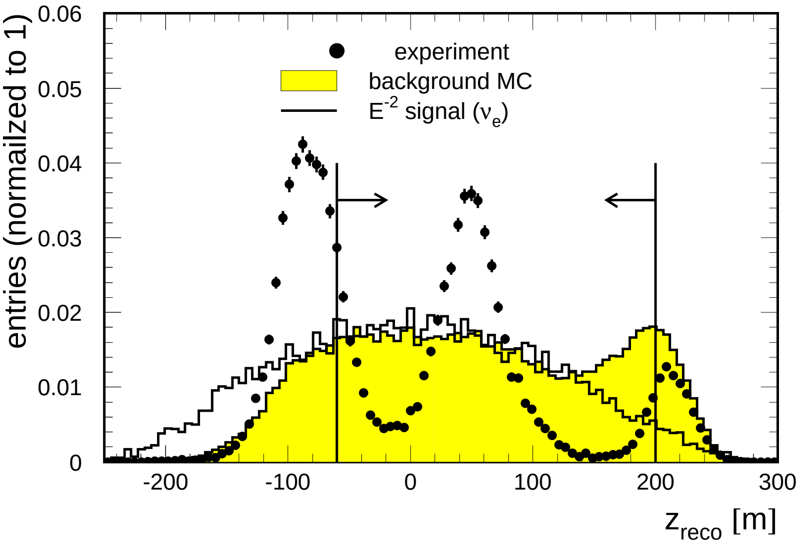

Figure 7.3.5: Distribution of the z-coordinate of the reconstructed vertex position.

simple, but physically motivated procedure for removing hits from the simulated data, leads to a qualitative agreement between experimental and simulated data. However, this special simulation can not be used for simulation of high energy events, and will hence not be used within this analysis.

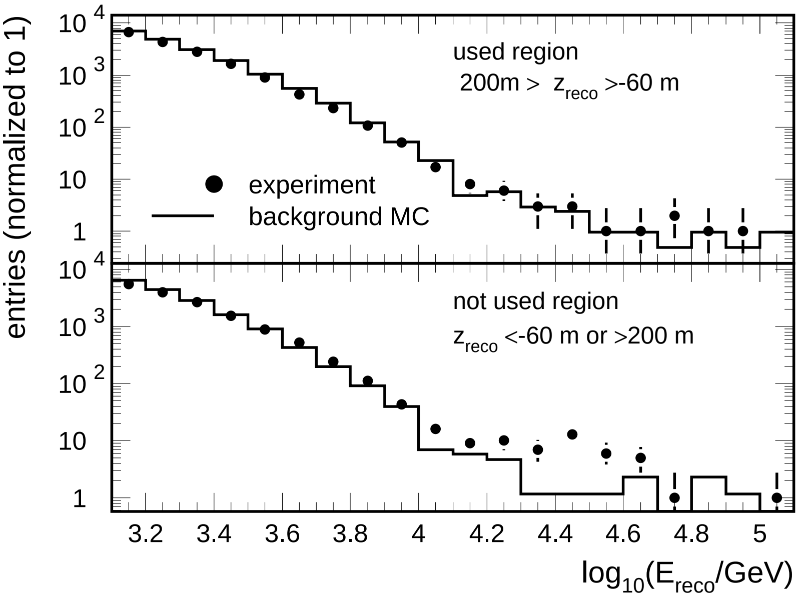

Figure 7.3.6: Spectrum of reconstructed energies for experiment and atmospheric muon MC simulation. The spectra are shown for events (top/bottom) within and outside the region, 200 m> z_{reco} >-60 m.

A cut on z_{reco} was introduced, removing events above 200 m and below -60 m. The instrumented volume ends approximately 200 m above and about 120 m below the center of the detector[1]. Nevertheless, the lower boundary was moved upward, because the background MC simulation does not reproduce the experimental data very well in the region $z_{\mathrm{reco}} \geq$-60 m. This is shown in figure 7.3.6, where the spectrum of reconstructed energies after cut # 4 is shown, for the region 200 m> z_{reco} >-60 m as well as for the region outside of the boundaries. For the region outside, the higher energy part of the spectrum, which is of main interest in this analysis, shows large discrepancies.

The radial distance

Figure 7.3.7 shows the distribution of the radial distance, $\rho_{\mathrm{reco}} = \sqrt{x^2_{\mathrm{reco}} + y^2_{\mathrm{reco}}}$, of the reconstructed vertex location as a function of the reconstructed energy. As can be seen, higher energetic events are often reconstructed at distances outside of the detector. This is expected, since these events are also visible at larger distances.

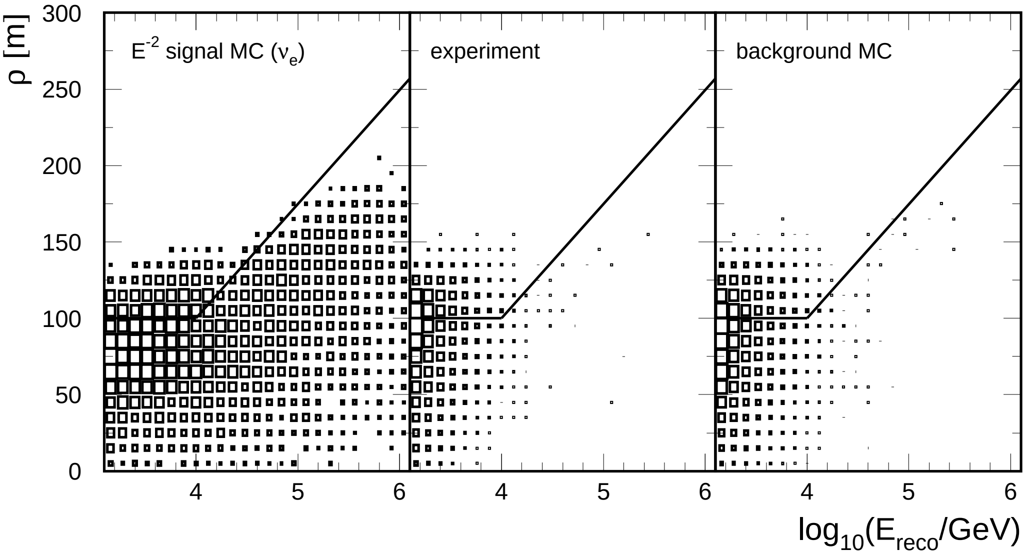

Figure 7.3.7: Distribution of radial distance, $\rho_{\mathrm{reco}} = \sqrt{x^2_{\mathrm{reco}} + y^2_{\mathrm{reco}}}$, versus reconstructed energy. Events in the region below the broken line pass the cuts.

In general, events reconstructed outside of the detector (the outer strings are arranged on a circle of radius ρ =100 m), are more likely to stem from atmospheric muons than events reconstructed inside the detector. This is because a muon event is more efficiently rejected, when passing through the detector volume. Hence, a cut is applied, restricting the radial vertex position:

$$\rho_{\mathrm{reco}} \leq \begin{cases} 100 \text{ m} & \text{for} \quad E_{\mathrm{reco}} \leq 10 \text{ TeV} \\ 75 \text{ m} \cdot \log(E_{\mathrm{reco}}/\mathrm{GeV}) - 200 \text{ m} & \text{for} \quad E_{\mathrm{reco}} > 10 \text{ TeV} \end{cases} \tag{7.3.2}$$

---

[1] The center of AMANDA-II is defined as the geometrical center of the smaller AMANDA-B4 detector.

For energies below 10 TeV, the cut leads to events contained in the fiducial volume of the detector. For higher energies, the allowed volume increases, since the anticipated background is rather small, and can effectively be removed by further cuts.

7.4 Final Selection Criteria

The final selection criteria consist of a cut on an event likelihood parameter, L_s, combined with a cut on the reconstructed energy. As will be described below L_s thereby unifies three discriminating variables into a single one. The discriminating power of L_s is not large enough to fully remove the background at all energies. At energies above ~50 TeV, however, the background expectation becomes marginal. Hence, the final selection criteria consists of a combined cut on L_s and E_reco. As will be described in detail below, the cut values where optimized for largest sensitivity to an astrophysical flux of neutrinos.

7.4.1 The Input Variables

The input variables which enter the final quality parameter, L_s, where chosen for their discriminating potential.

The radial distance between two vertex fits, $\boldsymbol{\Delta}\rho_\mathrm{xy}$. An additional vertex fit is performed, using the same method as for the regular one, but thereby excluding hits located within a 60 m sphere around the previously fitted vertex position. The selection of hits for a muon event is schematically illustrated in the left graph of figure 7.4.1. Using only hits outside a 60 m radius reduces the fraction of hits which stem from light of the brightest secondary cascade, and increase the fraction of hits steming from the muon. The underlying muon track becomes *visible* again. The radial distance between the regular and the additional fit has shown to be a useful parameter for discriminating signal from background:

$$\Delta\rho_\mathrm{xy} = \sqrt{(x_\mathrm{reco} - x_\mathrm{reco}^{60m})^2 + (y_\mathrm{reco} - y_\mathrm{reco}^{60m})^2}.$$

The coordinates x_reco^{60m} and y_reco^{60m} are those resulting from the additional fit. The distributions of $\Delta\rho_\mathrm{xy}$ for experimental data, simulated background and signal MC data is shown in the right plot of figure 7.4.1. As can be seen there is good agreement between the experiment and background MC simulation.

The likelihood of the vertex fit, $\mathbf{L}_\mathrm{vertex}$. This variable had already been used for cut # 3. However, as can be seen in figure 7.4.2, there is still some discrimination potential left. The agreement between experiment and background distributions is reasonably good.

The cosine of the muon track fit, $\cos\theta_\mu$. The events were reconstructed with a regular 1-p.e. muon likelihood fit [170]. The fit was thereby iteratively repeated 16 times, and the results with the best likelihood was stored in the event record. The distributions of $\cos\theta_\mu$ are shown in figure 7.4.2. The majority of atmospheric muon events reconstructed with $\cos\theta_\mu > 0.2$ can be considered well reconstructed. Note that the signal MC events, though originating from more or less isotropic neutrino directions, are reconstructed in a narrow peak around $\cos\theta_\mu = 0$. This is due to the spherical light field of cascades. The approximate spherical symmetry of the light field, which typically is only partially contained in the rather narrow AMANDA-II detector, results in a horizontally reconstructed muon track as the most favored solution. The distributions of the experimental data deviates strongest from the atmospheric muon MC simulation in the region of mis-reconstructed muon tracks, $\cos\theta_\mu < 0.2$. A possible reason for the discrepancy are wrongly simulated ice properties. As shown in figure B.0.3 of appendix B, a background simulation which aimed at improving the simulation of the vertical variations of optical properties of the ice, leads to a slightly better agreement.

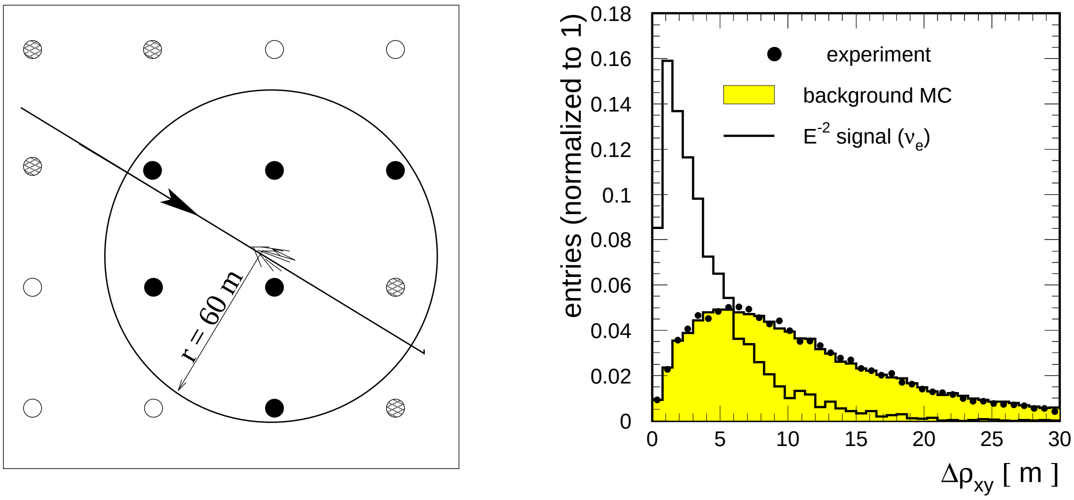

Figure 7.4.1: Left: Schematic distribution of hit OMs. OMs are represented by circles. Black OMs are hit by light from the secondary particle cascade, hatched OMs are hit by light from the muon and OMs which are not hit are represented by empty circles. Right: Normalized distribution of $\Delta\rho_{\rm xy}$. Shown are experimental data as well as background and signal MC simulations.

7.4.2 The Likelihood Parameter $L_{\rm s}$

The construction of a discriminating variable from a set of observables, $\vec{x}$, which can be used for classification of signal (s) and background (b), is a frequent issue in data analysis.

	Signal			**Background**			**Experiment**		
	$L_{\rm vertex}$	$\Delta\rho_{\rm xy}$	$\cos\theta_\mu$	$L_{\rm vertex}$	$\Delta\rho_{\rm xy}$	$\cos\theta_\mu$	$L_{\rm vertex}$	$\Delta\rho_{\rm xy}$	$\cos\theta_\mu$
$\cos\theta_\mu$	0.05	0.04	1	-0.08	-0.04	1	-0.11	-0.03	1
$\Delta\rho_{\rm xy}$	0.18	1		0.07	1		0.09	1	
$L_{\rm vertex}$	1			1			1		

Table 7.4.1: Correlation coefficient r for the four quality parameters in all simulations

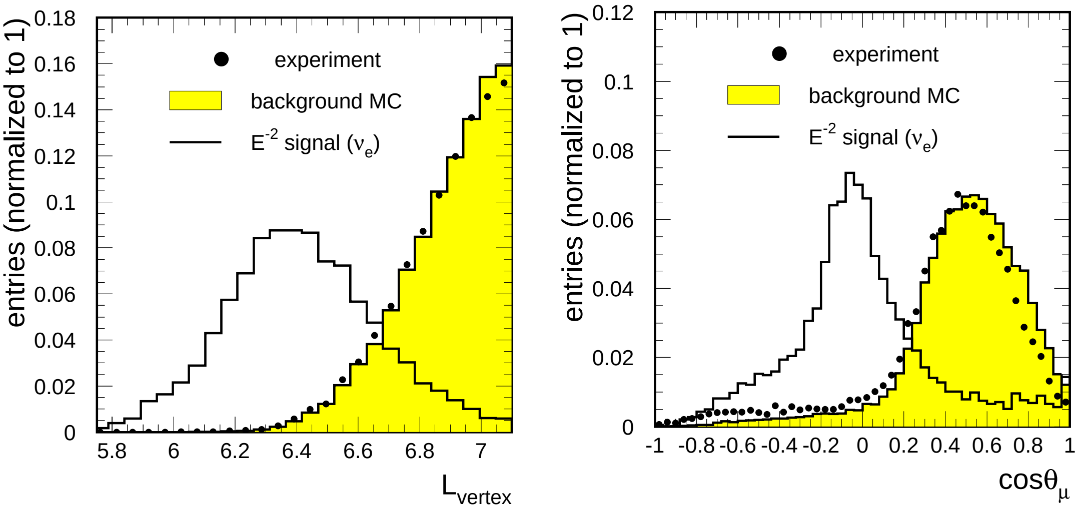

Figure 7.4.2: Normalized distribution of L_vertex and $\cos\theta_\mu$. Shown are experimental data as well as background and signal MC simulations.

For this work, a so called *Bayesian* discriminator is chosen. Ideally, the conditional probability density function (PDF), $P(\vec{x}|h)$, for observing $\vec{x}$ given the hypothesis h ($h \in \{s, b\}$), is known. If further the *a priori* PDF for a given hypothesis, $P(h)$, as well as the PDF for observing the set of observables, $P(\vec{x})$, is known, one obtains the PDF for a correct classification of h, given the observation $\vec{x}$:

$$P\left(h|\vec{x}\right) = \frac{P(h) \cdot P\left(\vec{x}|h\right)}{P(\vec{x})}. \tag{7.4.1}$$

This became known as Bayes theorem. In most realistic cases, however, the so called *prior* PDFs, $P(h)$, are not known. Therefore, one must chose the prior PDFs by hand. Interestingly, the choice has no impact for the purpose of classification, as shown in appendix C. Here, constant prior PDFs are assumed, $P(s) = P(b) = 0.5$, leading to

$$P(s|\vec{x}) = \frac{P(\vec{x}|s)}{(P(\vec{x}|s) + P(\vec{x}|b))}, \tag{7.4.2}$$

where $P(\vec{x}) = P(\vec{x}|s)P(\mathrm{s}) + P(\vec{x}|b)P(b)$ was used.

A practical problem is connected with the determination of $P\left(\vec{x}|h\right)$. In principle, this function can be obtained with help of MC simulation. In case of a large number of observables, the MC events will typically not cover the parameter space very well. For this reason one often chooses smoothening methods, as for example described in [98, 156]. Here, a simpler solution was adopted (see also [1]). The PDFs are approximated by the product of the one dimensional probability densities, $p(x_i)$:

$$L_\mathrm{s} := \frac{\prod_i p_i^s(x_i)}{\prod_i p_i^s(x_i) + \prod_i p_i^b(x_i)} \approx P(s|\vec{x}), \tag{7.4.3}$$

The one dimensional PDFs are defined by:

$$p_i^h\left(x_i\right) := \frac{f_i^h(x_i)}{f_i^s(x_i) + f_i^b(x_i)}, \tag{7.4.4}$$

where f_i^{s} and f_i^{b} are the *i-th* distributions for signal and background MC simulations, shown in figures 7.4.2 and 7.4.1. In the absence of correlations between the observables, the factorization in equation (7.4.3) would lead to an accurate representation of $P(\mathrm{s}|\vec{x})$. A correlation parameter can be defined as:

$$r_{i,j} = \frac{\langle\left(x_i - \langle x_i\rangle\right)\left(x_j - \langle x_j\rangle\right)\rangle}{\sigma\left(x_i\right)\cdot\sigma\left(x_j\right)}, \tag{7.4.5}$$

with $\langle x_i\rangle$ being the average and $\sigma\left(x_i\right)$ the RMS of the distributions. For full correlation, one obtains $r = 1$, while in case of no correlation one obtains $r = 0$. The resulting correlation parameters for the variables used here are summarized in table 7.4.5. As can be seen, they are rather small.

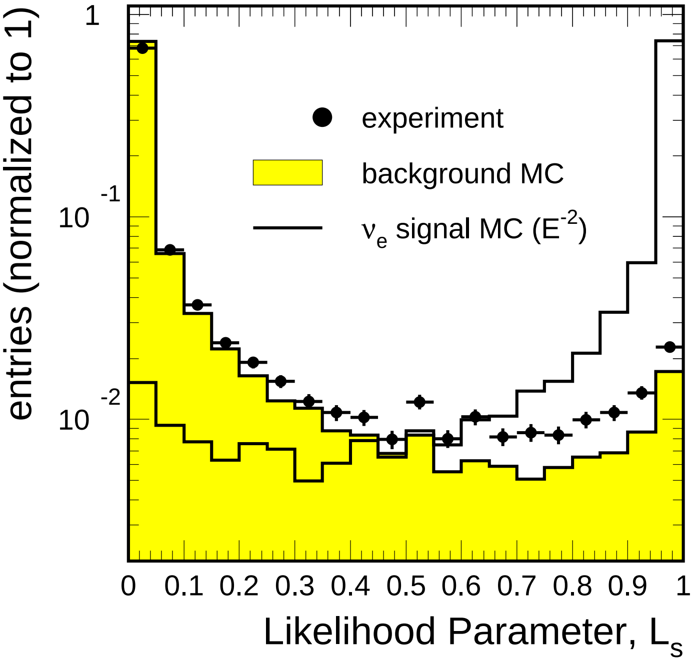

Figure 7.4.3: Normalized distribution of the likelihood parameter, L_{s}. Shown are experimental data as well as background and signal MC simulations after application of cut # 5.

The distribution of the likelihood parameter, L_{s}, as defined in equation (7.4.3), is shown in figure 7.4.3, for experimental data, signal and background MC simulation. The distribution of background events exhibits a peak at $L_{\mathrm{s}} \approx 0$, while the distribution of signal events peaks around $L_{\mathrm{s}} \approx 1$. For larger L_{s}, the experimental distribution exceeds that of the background MC simulation. This mis-match is mainly related to the mis-match in the distribution of $\cos\theta_\mu$, which was shown in figure 7.4.2.

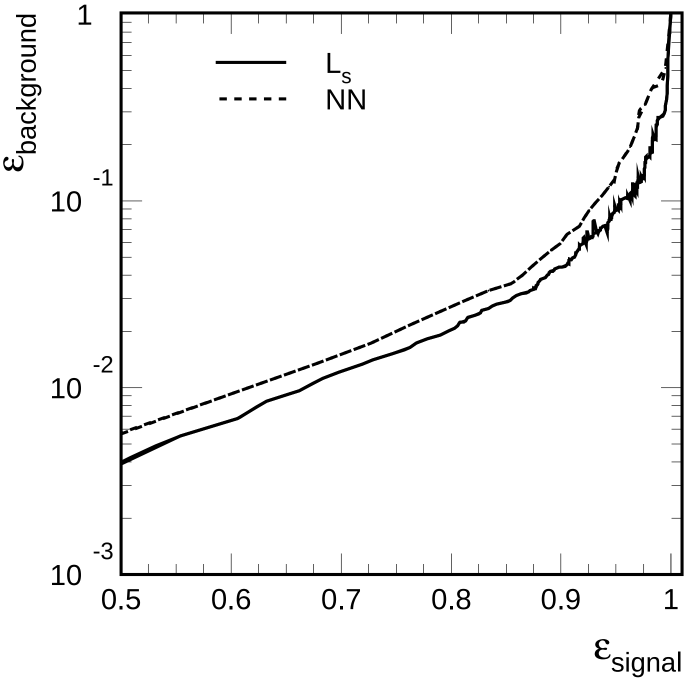

Figure 7.4.4: Discrimination potential of the likelihood parameter compared with that of a Neural Net .

The discriminating potential can be characterized by comparing the fraction of events passing a cut, $L_\mathrm{s} \geq L_\mathrm{cut}$, for background ($\varepsilon_\mathrm{background}$) and signal ($\varepsilon_\mathrm{signal}$). Figure 7.4.4 shows $\varepsilon_\mathrm{background}$ as a function of $\varepsilon_\mathrm{signal}$ for a large range of cut values.

How efficiently does L_s combine its input variables? For comparison, the discriminating potential of a *Neural Net* was tested. A Neural Net [89] was trained using the three input variables, which where used for the construction of L_s. Its architecture had a hidden layer with 6 nodes and one output node. The Neural Net returns a variable, which can be used similar to the likelihood parameter, L_s, for discriminating signal from background. The discriminating potential of this variable is shown in figure 7.4.4 as a dashed line. The performance of the Neural Net is thereby generally slightly worse than that of the L_s parameter. Note however, that the performance of the Neural Net can further be optimized, for example by rescaling its input variables.

7.4.3 Final Cuts

A cut on the likelihood parameter L_s reduces the background significantly, however, even after rather strict cuts background events remain. Since the aim of the analysis is to select astrophysical neutrinos, which are expected to have a harder energy spectrum, one can further reduce the background by selecting only high energy events. For this reason, additionally to the cut on L_s, a cut on the reconstructed energy, E_reco, was applied. The cut values are obtained from an optimization procedure, using only simulated data. The

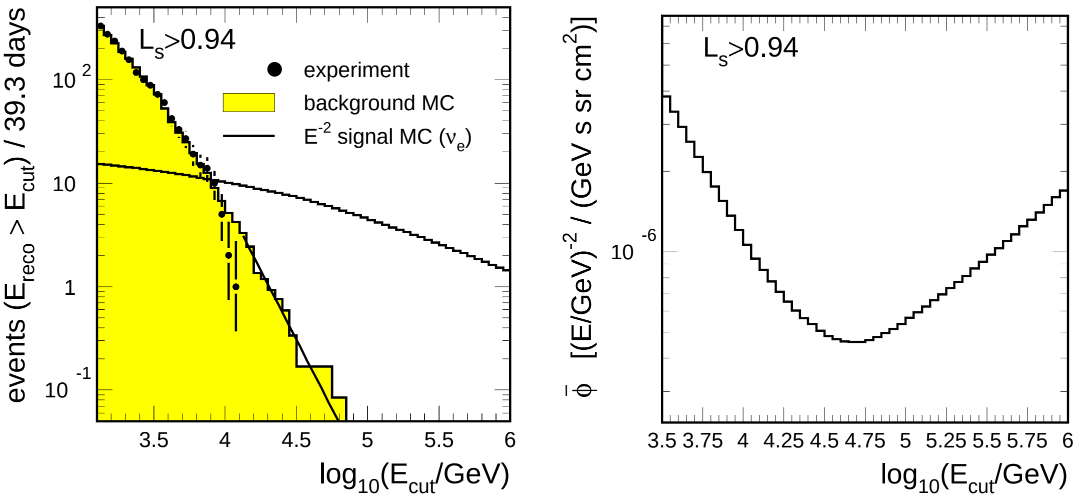

Figure 7.4.5: Optimization of energy cut. Left: Integrated spectrum of the experimental data (20 % of the full data set) and atmospheric muon background simulation. The smooth line is the result of a power-law fit to the simulation. Right: Average upper limit, $\overline{\phi}$, for the diffuse flux of ν_e after application of a cut $L_\mathrm{s} > 0.94$ shown as a function of the cut value E_cut.

reason for an optimization are twofold. First, one would like to have a final sensitivity of the analysis which is close to being optimal. And second, the cuts should be chosen independently of the experimental outcome. This is important, in order not to (unintentionally) tune the cuts to enhance or remove experimental events, since this would affect the outcome of the measurement.

The optimization procedure chosen here is based on a method described in [81]. The cuts are chosen to result in the highest sensitivity to an astrophysical flux of neutrinos. As a measure of the sensitivity, the so called average upper limit, $\overline{\phi}$, was used [52]. To obtain $\overline{\phi}$, the number of observed background events was simulated for a large number of repeated *toy* experiments, in the absence of signal. For each of these experiments, an upper limit on the flux of astrophysical neutrinos was computed (see section 9.2 for explanation of the limit calculation). $\overline{\phi}$ is then given by the average of the individual upper limits.

The optimization of $\overline{\phi}$ proceeded as follows. In a first step, a cut on L_s was applied and in a second step the optimal energy cut was evaluated. This was repeated for a large range of different L_s cuts to result in the optimal values for the L_s and energy cuts.

A problem in finding the optimal energy cut was, that fluctuations in the distribution of simulated background events significantly bias the outcome. The sensitivity becomes better, if the assumed background has a downward fluctuation. To obtain a smooth energy spectrum of the expected background, the distribution was fitted with a power-law function. Figure 7.4.5 (left) shows as an example the integrated distribution of reconstructed energies, as well as the result of the fit to the simulated background distribution, after a cut $L_\mathrm{s} > 0.94$ was applied. The simulated background distribution was normalized to the experimental data. The signal simulation corresponds to a flux of ν_e with strength $E^2\phi(E) = 10^{-6}$ GeV s^{-1} sr^{-1} cm^{-2}. The expected signal and background events above

E_{cut} can be used to calculate the average upper limit. The average upper limit after application of the cut $L_{\mathrm{s}} > 0.94$, for an experimental livetime of 197 days is shown in figure 7.4.5 (right) as a function of the energy cut. The cut values leading to the lowest $\overline{\phi}$ is $\log(E_{\mathrm{cut}}/\mathrm{GeV}) = 4.7$.

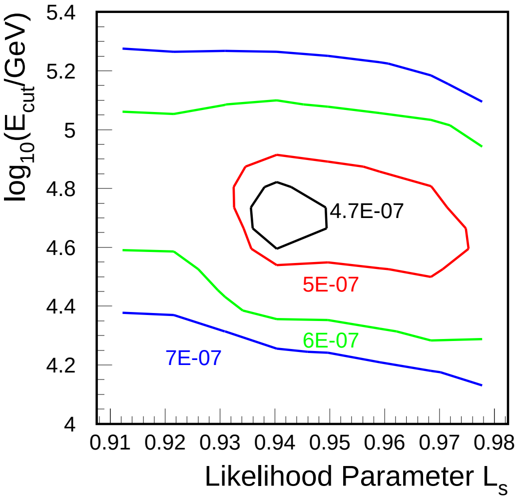

Figure 7.4.6: Optimization of final cuts. The sensitivity for the diffuse flux of ν_e is shown as a function of cuts on E_{reco} and L_{s}. The coefficient next to the contour lines correspond to the average upper limit in units of $(E/\mathrm{GeV})^{-2} \cdot \mathrm{GeV}^{-1}\ \mathrm{s}^{-1}\mathrm{sr}^{-1}\mathrm{cm}^{-2}$. See text for details.

By repeating this procedure for a range of different L_{s} cuts, the sensitivity as a function of the cut values was obtained. The optimal cuts are $L_{\mathrm{s}} = 0.94$ and $\log(E_{\mathrm{cut}}/\mathrm{GeV}) = 4.7$, leading to an average upper limit of $4.6 \cdot 10^{-7}(E/\mathrm{GeV})^{-2} \cdot \mathrm{GeV}^{-1}\ \mathrm{s}^{-1}\mathrm{sr}^{-1}\mathrm{cm}^{-2}$. This is shown in figure 7.4.6.

7.5 The Final Spectrum

The energy spectrum of the events of the full experimental data sample, after application of all but the final energy cut, is shown in figure 7.5.1 (left). The simulated background distribution was normalized to the experiment. The final energy cut, as obtained from the optimization procedure, is indicated by the line with the arrow. One experimental event of the 2000 data set passed all cuts.

The expected background consists of atmospheric muon events and to a smaller extent atmospheric neutrino induced events. For the first time during the analysis, the fraction of events induced by neutrinos is not negligible.

Figure 7.5.1 (right) shows the energy spectrum expected from atmospheric neutrino induced events. The event rate due to ν_e and ν_μ is shown separately (both CC and NC reactions are included). Note that the rate of ν_μ induced events exceeds the rate of ν_e induced events. This is due to the fact that the flux of ν_μ generated in the atmosphere is much larger than the flux of ν_e (see section 2.4.3). Hence, despite the larger efficiency of ν_e induced events to pass all cuts, the number of expected ν_μ induced events exceeds

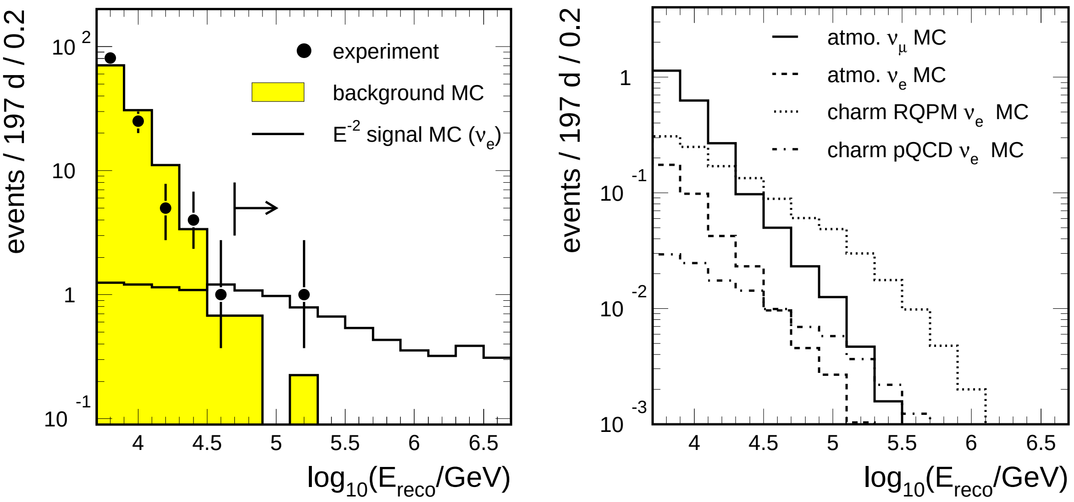

Figure 7.5.1: Distributions of reconstructed energies after all but the final energy cut. Left: experimental data, atmospheric muon background simulation and a hypothetical flux of astrophysical neutrinos. The final energy cut is indicated by the line with the arrow. Right: expected event rates from conventional and prompt atmospheric neutrinos.

those due to ν_e. The detection efficiencies of the various neutrino flavors will be compared in more detail in section 8.1.

Additionally, figure 7.5.1 (right) shows two representative models for a prompt atmospheric ν_e flux (see section 2.4.3 for a brief review of the prompt neutrino flux). Since the cross-sections involved in the production of charmed particles in the atmosphere are not well known, this flux is rather uncertain. The lower bound shown in figure 7.5.1 (right) is given by a pQCD calculation of the cross-section [69]. The upper curve corresponds to a flux calculation which is based on a non-perturbative model for the cross-sections [36], named Recombination Quark Parton Model (RQPM). Since the prompt atmospheric neutrino flux is so uncertain, it will not be counted as background, but instead as a potential signal. Upper limits on the flux of neutrinos due to prompt charm production will be given in section 9.2.

experiment	atm. μ MC	atm. ν_e MC	atm. ν_μ MC
1	$0.90^{+0.69}_{-0.43}$	$0.011^{+0.015}_{-0.007}$	$0.050^{+0.075}_{-0.03}$

Table 7.5.1: Number of events passing the final cut for experiment and background simulation consisting of atmospheric muons, atmospheric ν_e and ν_μ.

Table 7.5.1 lists the number of events surviving all cuts for both experiment and background simulation of atmospheric muons and neutrinos. The quoted errors will be explained in section 7.6. The total expected background is $0.96^{+0.70}_{-0.43}$, where the individual errors have been added quadratically. This is consistent with the number of observed events.

7.6 Systematic Uncertainties

In this section, the systematic uncertainties of the background and signal predictions are discussed. The influence of the uncertainties will be evaluated in terms of final event rates. The predicted event rates, along with its uncertainty, will be used in chapter 9 to calculate upper limits on the flux of astrophysical neutrinos. Each class of events has their specific uncertainties and hence will be discussed separately. Nevertheless, a few sources of systematic uncertainties affect all classes of events:

Uncertainties in the optical properties of the ice. As mentioned in section 6.2.4, there is an uncertainty connected with modeling the optical properties of the ice. To obtain an estimate of the impact of this uncertainty, two implementations were used for simulation, namely the MAM and KGM ice-models.

Uncertainties in the OM efficiencies. The combined transmissivity of pressure sphere glass, optical gel and PMT glass has been measured in the laboratory. Some PMT specific properties such as quantum and collection efficiencies have only been measured for a few selected PMTs. Aging effects of the PMT and of the optical gel could lead to a slight degradation of the total efficiency. The uncertainty related to the total transmissivity is roughly 20 %.

The situation becomes more complicated, if effects due to the re-frozen ice of the drill hole are included. The so called *hole-ice* has distinctly different optical properties due to fresh air bubbles. This leads to a change in the angular response function of the OM. By using atmospheric muons to evaluate the angular response function of the OM, it was shown that the sensitivity in forward direction (photon incident angle parallel to the PMT axis) might be overestimated by as much as 40 % [128]. Here, the average sensitivity for all photon incident angles is of main importance, since the typical distance between emitter and receiver is significantly longer than the scattering length. On average the sensitivity is reduced by ∼20 %. Combining this with the uncertainties in the efficiency of the OM itself leads to a total of ∼30 % uncertainty. An investigation of atmospheric muon data showed that the variations between the sensitivity of individual OMs are smaller than this uncertainty [118].

Light yield. In principle the Cherenkov light yield from charged particles can be precisely calculated. However, as described in section 3.4.1, different calculations have lead to results which vary by as much as ±20 %. The light yield currently used in the AMANDA detector simulation is 10 % lower than the latest calculations. For cascades, a larger or smaller light yield is indistinguishable from larger or smaller OM sensitivities.

Cut efficiencies. Many cuts where necessary to reduce the background to the final level. Often, the experimental distribution of the cut variables where not well described by the MC simulation. As summarized in table 7.2.1 some of the cuts lead to different passing rates for experimental and simulated MC data. Generally, experimental data events have the higher passing rate, thus relaxing the concern that the cuts remove an unpredictably larger fraction of hypothetical signal events. Nevertheless, in order to estimate the systematic effects which the cuts have on the final data set, selected cuts were varied over a small range.

7.6.1 Uncertainties in the Event Rate due to Atmospheric Muons

The background expectation of atmospheric muons has a large uncertainty. The main reason is the limited available statistics of simulated atmospheric muon events. The difference in passing rates indicates a possible source of error which will be discussed in connection with uncertainties in cut efficiencies as well as in the light yield of cascades.

Limited statistics. After application of the final cut $L_{\mathrm{s}} > 0.94$ and above a reconstructed energy of 5 TeV one is left with 4.4 times more MC events than in the experiment. (The energy bound is necessary, since the optimized atmospheric muon simulation is only applicable above a minimal energy.) Based on the available statistics of experimental ($N_{\mathrm{exp}} = 117$) and simulated ($N_{\mathrm{MC}} = 519$) events it is convenient to introduce an effective livetime of the MC sample which is $N_{\mathrm{lt}} = N_{\mathrm{MC}}/N_{\mathrm{exp}} = 4.4$ times longer than that of the experiment. Taking into account the difference in passing rate, this corresponds to a simulated livetime of more than 2000 days. Four atmospheric muon MC events have passed all cuts which, after scaling with a factor $1/N_{\mathrm{lt}}$, corresponds to an event expectation for the experimental data set of 0.90. The statistical uncertainty on this number is obtained by the 68 % CL upper and lower bounds obtained from Feldman and Cousins [52], scaled with the factor $1/N_{\mathrm{lt}}$, $N_{\mu} = 0.90^{+0.65}_{-0.36}$. The method of Feldman and Cousins was used to evaluate the statistical errors since it is well suitable for small numbers. Note that an additional uncertainty is introduced, since the normalization value is by itself uncertain. With 117 experimental events before the final energy cut, this error is approximately 10 % and because of its smallness will be neglected in the further discussion.

Uncertainties in the optical properties of the ice. To estimate the influence of ice properties on the background expectation, atmospheric muons were simulated using both the MAM and KGM ice-models. Approximately equally large data sets exist of both type, which where combined in the above estimate of the background. Figure 7.6.1 shows the spectra of reconstructed energies for experimental data and the two background MC data samples. In both MC samples two events pass all cuts. If one again normalizes the MC spectra to the experimentally observed, the two events translate to an expectation of 0.79 events (for MAM) and 1.04 events (for KGM). The statistical error on these numbers is according to Feldman and Cousins ~ 100 %. To reduce the influence of the limited statistics of simulated events, one can fit the background distributions, over a large range of energies. Figure 7.6.1 shows the result of an exponential fit to both MC spectra. Using the result of the fits leads to a background prediction of 0.93 (for MAM) and 1.19 events (for KGM). These values, though being larger, are consistent with the previous estimates of N_{μ}. Taking the mean value as the central value one obtains: $N_{\mu}^{\mathrm{fit}} = 1.06 \pm 0.13$. This central value will further not be used, since it is not clear if the exponential fit results in a reliable extrapolation. Nevertheless, the relative error can be used for estimating the uncertainties, since the bias introduced by the choice of the fit function is similar for both data sets. A relative error of 12 % due to uncertainties in the ice properties is consistent

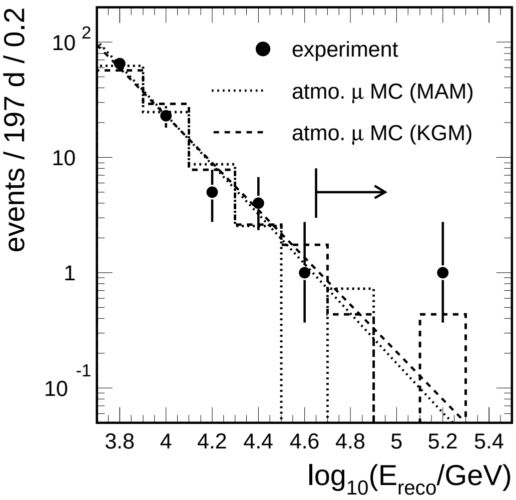

Figure 7.6.1: Energy spectra of experimental data and atmospheric muon MC samples simulated with KGM and MAM ice-models. The smooth lines are the result of an exponential fit to the two MC distributions.

with the above estimate obtained from counting the events passing the cuts.

Cut efficiencies. Experimental and predicted passing rates deviate by more than a factor of two. Typically, the passing rate for experimental data is higher. The reason is not clear and obviously is related to an insufficient description of the detector response. In order to estimate this effect, the final cut on L_s was lowered for MC data ($L_\mathrm{s} > 0.85$), so that the fraction of events passing the cut is similar to that in the experiment. Following the above prescription and normalizing the MC spectrum to that of the experiment leads to an expectation of 1.1 events for the experimental data sample, which is an increase of approximately 20 % over the previous estimate. If the cut is tightened instead, the statistics of remaining events is too small to obtain a meaningful estimate of the background.

OM sensitivity and light yield. The effect of uncertainties in the OM efficiency translates into large uncertainties in the total rate of events. The effects on the final spectrum can be estimated analytically. As shown in section 3.5.2, the spectrum of secondary particles can be approximately described by a power-law, $\mathrm{d}N/\mathrm{d}E_\mathrm{secondary} \propto E_\mathrm{secondary}^{-3.48}$ for $E_\mathrm{secondary} \gtrsim 3$ TeV. If the uncertainty in the light yield is expressed in terms of a scaling factor S, the number of events above a given threshold of visible light follows $\propto S^{-2.48}$. A 30 % systematic uncertainty in the OM sensitivity translates to a systematic error of a factor $(1 \pm 0.3)^{-2.48} \approx 2^{\pm 1}$ in the total event rate. This effect could explain the observed discrepancy in the passing rates of MC and experimental data. Note however, that a constant scale factor S would not change the slope of the high energy part of the spectrum. Hence it would not lead to a change in the atmospheric muon prediction after normalization the MC spectrum to that of the experimental data.

A similar argument can be made for the systematic uncertainties due to the uncertainty in the light yield of electromagnetic and hadronic cascades. For low energy muons most Cherenkov light stems from the muon itself, while for high energies ($\gtrsim 1$ TeV), the Cherenkov light from secondary particles dominates. Since for cascades, a larger or smaller light yield is indistinguishable from a larger or smaller OM efficiency, the effects on the high energy part of the spectrum are of the same type. As discussed in section 3.4.1, various calculations of the light yield of electromagnetic cascades have led to different results. The light yield currently used in the AMANDA detector simulation is 10 % lower than the latest calculations. If instead the newer value would have been used, one would expect approximately 30 % more atmospheric events at high energies.

Theoretical uncertainties. The flux and the composition of primary cosmic rays has an uncertainty, which is generally growing with cosmic ray energies. The total flux normalization does not impact the final result, as the simulated background distribution is normalized to the experimental one. However, uncertainties in the spectral slope and composition result in a change of the final distribution of reconstructed energies. The uncertainty in the slope of the primary spectrum at the energies of interest ($E_{\mathrm{primary}} \approx 10$ TeV - 1 PeV) was evaluated to $\Delta\gamma = 0.02$ [82]. Another source of uncertainties are the high energy interaction models used. Atmospheric muons where generated using various high energy interaction models available within CORSIKA [38]. The spectral index of the cosmic ray primary flux was unfolded using the various MC samples and with the exception of the SYBILL interaction model, the results are consistent within $\Delta\gamma = 0.1$. The results obtained with the SYBILL interaction models are not consistent with results of other direct or indirect measurements and are hence not considered. The effect due to insufficient knowledge of the spectral shape or interaction model can be estimated by reweighting the available atmospheric muon events according a varied primary spectrum. Reweighting the events with a factor proportional to $E_{\mathrm{primary}}^{\pm\Delta\gamma}$ leads to a change in predicted number of events of only 5 %. Effects due to a variation of the composition are estimated to be even smaller.

Muon propagation, though in principle well understood, is a numerically challenging part in the simulation. However, systematic uncertainties in the cross-section, or limited numerical precision have a reasonable small impact [35]. The flux of atmospheric muons at depth of the AMANDA detector has an additional systematic uncertainty of only a few percent. Additionally, the process being most important for this analysis is bremsstrahlung has a well established cross-section.

Altogether, the theoretical uncertainties are estimated to be smaller than those due to other effects discussed above and will not be considered any further.

The uncertainty of the total number of events expected due to atmospheric muons can now be estimated:

$$N_\mu = 0.90(^{+0.65}_{-0.36})^{\mathrm{stat}}(\pm 0.11)^{\mathrm{ice}}(\pm 0.20)^{\mathrm{cuts}} \approx 0.90^{+0.69}_{-0.43}.$$

In the last step, the individual errors were added in quadrature.

7.6.2 Uncertainties in the Event Rate due to Atmospheric Neutrinos

The uncertainty in the event rate due to conventional atmospheric neutrinos is large and nearly independent of the flavor of the interacting neutrino. This is due to the fact that the energy spectra of ν_e and ν_μ are steeply falling ($\phi \propto E^{-3.7}$), which results in large energy threshold effects.

Large uncertainties in the predicted rates arise due to insufficient knowledge of the ice. Again, we use the two available ice models to estimate the uncertainties. For the MAM ice-model one expects 0.03 events while for KGM one expects 0.09 events per 197 days livetime after final cuts are applied. The strong effect of the assumed ice models can be understood, since a change in the simulated attenuation length leads to systematically shifted reconstructed energies (see section 5.3) and hence changes the effective threshold energy.

Effects due to uncertainties in the light yield and OM sensitivity was estimated by simulation of a detector with a 30 % reduced or increased OM sensitivity. The uncertainty in either OM sensitivity or light yield translates to an uncertainty of approximately a factor of two.

The filter efficiency has a smaller error than that for atmospheric muons. The reason is the significantly larger fraction of events passing the cuts. For example, relaxing the final cut to $L_{\mathrm{s}} > 0.85$ (as described in section 7.6.1) leads to a moderate increase of 10 % in rate.

Additionally, one has a theoretical uncertainty in the primary neutrino flux prediction. It was estimated in [59] that the uncertainty of the conventional atmospheric neutrino flux does not exceed 20 %.

The total number of events expected due to conventional atmospheric neutrinos is estimated to be:

$$N_\nu^{\mathrm{atmo}} = 0.06(^{+0.08}_{-0.02})^{\mathrm{sensi}}(\pm 0.03)^{\mathrm{ice}}(\pm 0.01)^{\mathrm{theo}} \approx 0.06^{+0.09}_{-0.04}.$$

Only the three main contributions to the systematic error are displayed. The individual errors where added in quadrature to obtain the total error. Since the expected background due to atmospheric neutrinos is small, it's impact on the final result is marginal.

7.6.3 Uncertainties in the Detection Efficiency of Astrophysical Neutrinos

The typical assumed astrophysical neutrino flux has a harder spectrum than that of atmospheric neutrinos and muons. This reduces the energy threshold effects, which leads to smaller uncertainties in their detection efficiency.

The evaluation of the systematic error due to the uncertainty in the ice properties follows that of atmospheric neutrinos. The systematic error due to an uncertainty in the OM sensitivity has been evaluated by generating MC event samples using an OM sensitivity reduced or increased by 30 %. The resulting systematic variations in event rates are summarized in table 7.6.1 for various assumed spectral slopes. The three values per table entry represent the event rates for ν_e, ν_μ and ν_τ in percent of the default (MAM ice model). For hard spectra following E^{-1} to E^{-2}, the variations are smaller than 25 %. For a steeper spectrum $\propto E^{-3}$ the systematic errors become larger than 50 %.

Evaluation of the systematic error due to uncertainties in the cut efficiency was done similarly as for atmospheric neutrinos and muons. The systematic error is not larger than 10 %.

A small additional error is introduced by the simplifications made in the simulation of cascades. The *ksplit* program (see section 6.2.4) was used to generate a smaller but more realistic sample of ν_e events. The difference in resulting event rates is not larger than 1 %, which additionally validates the assumptions made in the simulation.

The uncertainties related to the cross-section calculations used can be estimated by comparing the result of various calculations. In the energy range of interest (100 TeV $\lesssim E_\nu \lesssim$ 10 PeV), different extrapolations of the structure functions lead to cross-section predictions which vary by less than 5 % [62]. The cross-sections used here match those tabulated in [62, 63].

Systematic effects related to electronics artefacts such as cross-talk were evaluated to be smaller than 10 % for the AMANDA-B10 detector [155]. Since the majority of additional OMs of AMANDA-II are read out through optical fibers and hence have a considerably smaller cross-talk probability, the effects due to cross-talk should have decreased. The previous calculations will not be repeated for AMANDA-II and instead the value for AMANDA-B10 is taken as a conservative estimate of the effects due to cross-talk.

	E^{-1}	E^{-2}	E^{-3}
KGM	81/95/91	109/120/121	177/179/192
70 %	95/92/95	79/76/85	60/54/71
130 %	98/105/99	110/122/119	136/154/155

Table 7.6.1: Summary of systematic effects for neutrino rates. The three values represent the event rates for ν_e, ν_μ and ν_τ in percent of the default (MAM ice-model). The relative rates are shown for a simulation using the KGM ice-model, and OM sensitivities which were scaled by 70 and 130 %. The rates are shown for three different assumed slopes of the neutrino energy spectrum.

Altogether, the uncertainties in the event rate of a hypothetical flux of ν_e, ν_μ or ν_τ with a spectrum $\propto E^{-1}$ to E^{-2} do not exceed 25 %. For a spectrum $\phi \propto E^{-2.7}$, as typically expected for atmospheric neutrinos from prompt charm decay, the systematic errors become as large as 50 % and for steeper spectra even larger.

Chapter 8

The Effective Detector Size

This chapter will focus on the resulting capabilities of the AMANDA detector to detect astrophysical neutrinos. Useful measures of the detector efficiency are the neutrino effective area and the effective volume.

8.1 Effective Volume for Neutrino-induced Events.

Assuming an ideal detector, which is able to detect all neutrino reactions inside its fiducial volume V and given a flux of neutrinos at the Earth's surface, $\phi(E_\nu, \theta)$, the number of events observed is:

$$N_{\text{event}} = \frac{\rho}{m_{\text{N}}} T \int\int\int \mathrm{d}E'_\nu \mathrm{d}E_\nu \mathrm{d}\Omega \; \phi(E_\nu, \theta) P(E_\nu, E'_\nu, \theta) V \sigma(E'_\nu). \tag{8.1.1}$$

ρ is the density of the detector material, m_{N} is the mass of a nucleon and T is the exposure time. $P(E_\nu, E'_\nu, \theta)$ is the transition probability density for a neutrino being injected at the Earth surface with energy E_ν and zenith angle θ to emerge at the detector with E'_ν. $\sigma(E'_\nu)$ is the total cross-section for a neutrino interaction.

Since Cherenkov telescopes such as AMANDA have no clearly defined spatial boundaries, it is useful to introduce the concept of effective volume. The effective volume allows an intuitive characterization of the detector sensitivity as a function of the neutrino energy and angle of incidence as well as a comparison of the sensitivities of different detectors.

The effective volume is defined as:

$$V_{\text{eff}} = \lim_{\substack{V_{\text{gen}} \to \infty \\ N_{\text{gen}} \to \infty}} \frac{N_{\text{final}}}{N_{\text{gen}}} \times V_{\text{gen}}. \tag{8.1.2}$$

Here, V_{gen} is the generation volume in which neutrino interactions were simulated, and N_{gen} is the number of neutrino events simulated. N_{final} is the number of events triggering the detector and passing all cuts of the cascade analysis. In practice, one chooses a generation volume just large enough to contain all neutrino tracks that can possibly contribute to N_{final}. Note that in the definition used here, neutrino absorption and regeneration effects are implicitly included in the effective volume, since N_{gen} is the number of all simulated

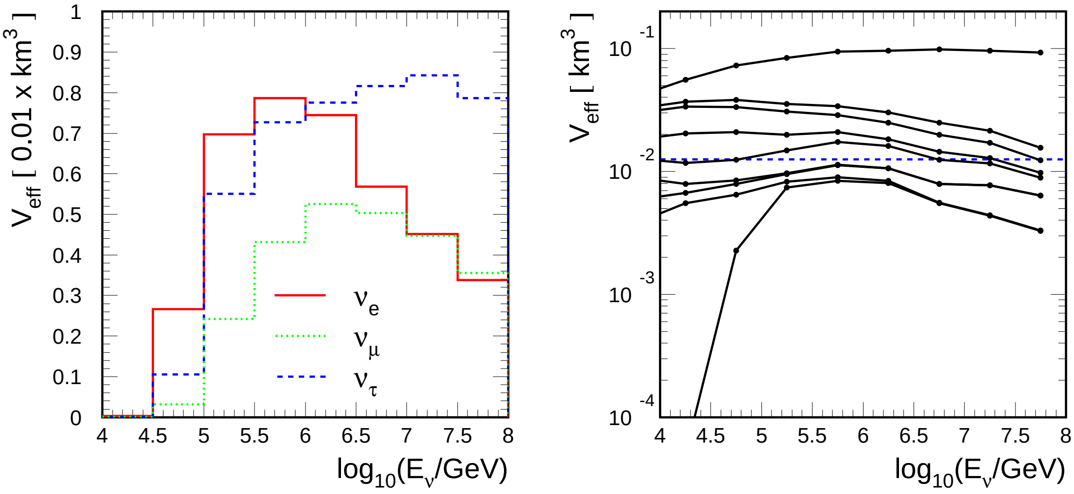

Figure 8.1.1: Left: Effective volume for ν_e, ν_μ and ν_τ interactions as a function of the neutrino energy (in units of 0.01×km^3). Right: Effective volume for ν_e events on trigger level (upper line) and after application of cut # 1 to 7 (all lines below). The final cut is the cut on the reconstructed energy. The dashed line indicates the geometrical volume of a cylinder of 100 m radius and 400 m height.

events, counting also neutrinos which are absorbed in the Earth. The analogy to an ideal detector with a volume V is given by:

$$V_{\text{eff}}(E_\nu, \theta) = \int \mathrm{d}E'_\nu P(E_\nu, E'_\nu, \theta) V. \tag{8.1.3}$$

V_{eff} should *not* be inserted into equation (8.1.1) to calculate the event rate, unless the transition probability is described by a delta function: $P(E_\nu, E'_\nu, \theta) \propto \delta(E_\nu - E'_\nu)$. In case regeneration effects are significant, the effective volume should not be used to calculate event rates. For calculation of event rates we advocate to use the less intuitive effective area described in the next section.

Figure 8.1.1 (left) shows the final volume after all cuts were applied as a function of the neutrino energy for ν_e, ν_μ and ν_τ. The effective volumes were averaged over all angles of incidence. The volume starts to increase above a threshold energy of ∼50 TeV which is a result of the cut on the reconstructed energy. For ν_e events, the visible energy[1] is only slightly smaller than the neutrino energy itself. Only for NC reactions, which are suppressed due to a lower cross-section by more than a factor two, the visible energy is substantially smaller than the neutrino energy. The maximal effective volume for ν_e is reached at neutrino energies of a few hundred TeV and then slowly declines again. The decline is partially caused by the reconstruction and selection criteria, which for the highest energies have a worse performance. The other reason for the decline is neutrino absorption in the Earth, which leads to an energy dependent reduction of the flux of ν_e.

The efficiency of ν_μ events to pass all cuts is lower than the efficiency of ν_e and ν_τ events. This can be understood since for ν_μ the visible energy of the vertex cascade is

---

[1] The visible energy corresponds to the light yield of an electro-magnetic cascade.

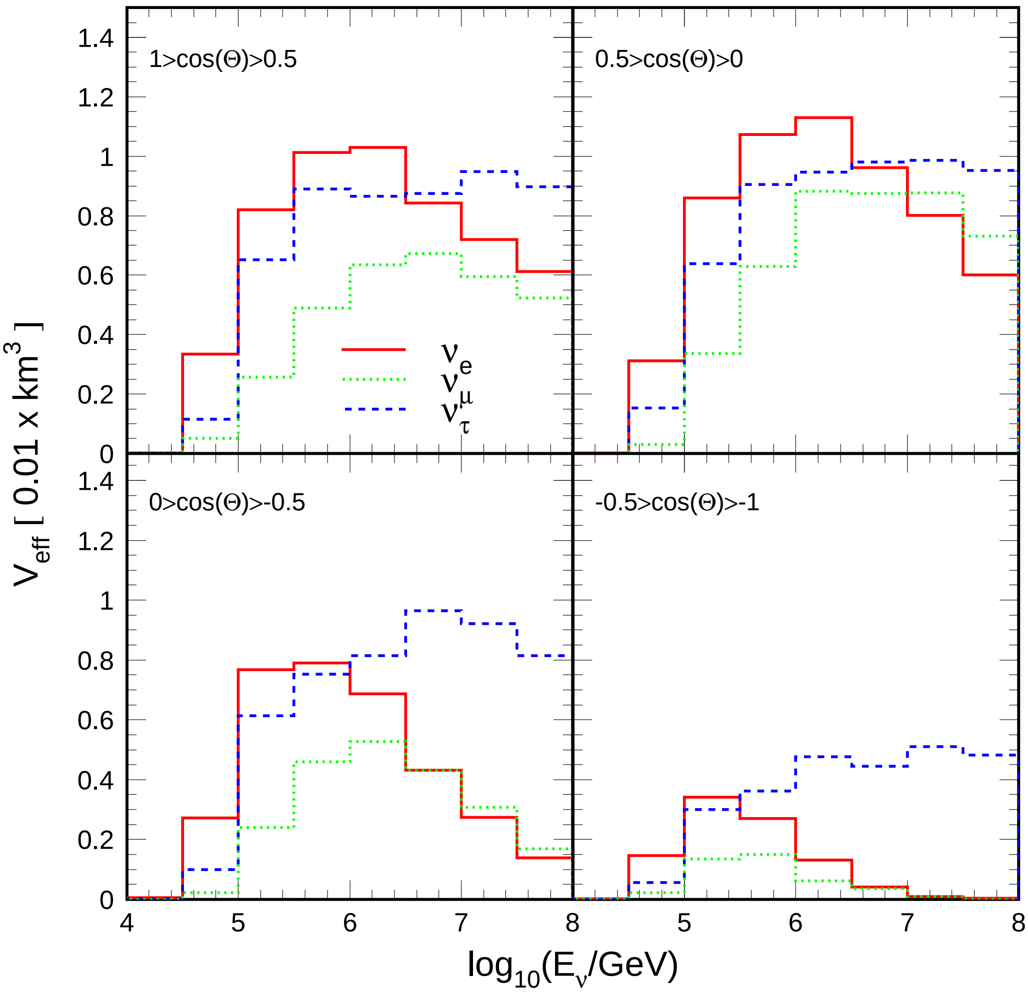

Figure 8.1.2: The effective volume as a function of the neutrino energy for all neutrino flavors and different zenith angle bins.

typically lower than in the case of ν_e and ν_τ. Additionally, the muon generated in a CC reaction is often mis-identified as an atmospheric muon and hence the event is rejected. At higher energies the volume decreases again. While neutrino absorption affects ν_μ in a similar way as ν_e, the decline due to reconstruction and selection effects sets in at higher neutrino energies (but at similar visible energies).

For ν_τ, the maximal effective volume extends to higher energies and saturates at a volume of about 0.008 km^3. The reason for the different behavior when compared to ν_e is the fact that ν_τ do not get absorbed in the Earth but instead regenerate to lower energies (see section 3.5.1). High energy ν_τ are regenerated to energies of $\mathcal{O}(100\ \mathrm{TeV})$, at which the Earth becomes transparent again. Additionally, there is a contribution due to *double-bang* events (see section 3.2). At energies above 10 PeV, the average distance between the vertex and the decay of the tau is several hundred meters. Hence the chances to observe the event by either the cascade from the vertex or the decay increases by up to a factor of two. The track of the tau itself, being minimum ionizing, is producing relatively few hits and is hence not contributing significantly to the event.

The effect of the cuts on the effective volume is illustrated in figure 8.1.1 (right). The effective volume for ν_e is shown for triggered events, as well as after application of all successive cuts. The cuts reduce the effective volume by more than one order of magnitude, but the remaining effective volume is not much smaller than the geometrical size of the detector, approximately given by a cylinder of 100 m radius and 400 m height.

Figure 8.1.2 shows the effective volume after all cuts for four different angles of incidence. The effective volume was calculated according to equation (8.1.2), however restricting the angle of incidence of the generated neutrino events to the four zenith angle bins: $1 > \cos(\theta) > 0.5$,$0.5 > \cos(\theta) > 0$, $0 > \cos(\theta) > -0.5$ and $-0.5 > \cos(\theta) > -1$.

For $\cos(\theta) < 0$ reduction due to neutrino propagation becomes significant. It is only due to the regeneration of ν_τ that its effective volume saturates with increasing neutrino energy.

8.2 Effective Area for Neutrinos

The effective area for neutrinos is useful for calculating neutrino event rates for a given neutrino flux. However, the correspondence with the actual detector size is less intuitive than that of the effective volume. The effective area represents the area of an ideal detector which is capable of detecting neutrinos with full efficiency. The number of events observed with such a detector is given by:

$$N_{\text{event}} = T \int \mathrm{d}E_\nu \mathrm{d}\Omega \; \phi(E_\nu, \theta_\nu) A_{\text{eff}}(E_\nu, \theta_\nu) \tag{8.2.1}$$

Given the simplicity of equation (8.2.1), one can argue that A_{eff} is the most meaningful representation of the detector sensitivity.

The effective area is calculated by:

$$A_{\text{eff}} = \lim_{\substack{A_{\text{gen}} \to \infty \\ N_{\text{gen}} \to \infty}} \frac{N_{\text{final}}}{N_{\text{gen}}} \times A_{\text{gen}} \times P_{\text{inter}}. \tag{8.2.2}$$

The fraction of finally selected to generated events is scaled with the size of the generation plane A_{gen}, which is the cross-sectional area of the cylinder that contains all generated neutrino tracks with directions parallel to its axis. Finally, one multiplies this area by the interaction probability of the neutrino passing through the cylindrical volume, P_{inter}. Here, one averages over the full range of neutrino directions.

Figure 8.2.1 (left) shows the effective area for ν_e, ν_μ and ν_τ after all cuts of this analysis have been applied. The effective area is rising for the full range of simulated energies. It is the growing interaction probability which compensates for detector saturation and neutrino propagation effects. The effective area for neutrinos and anti-neutrinos is generally very similar, with the exception of $\overline{\nu}_e$ near the Glashow resonance (see section 3.1.1). The additional effective area due to the resonant increase of cross-section is shown in

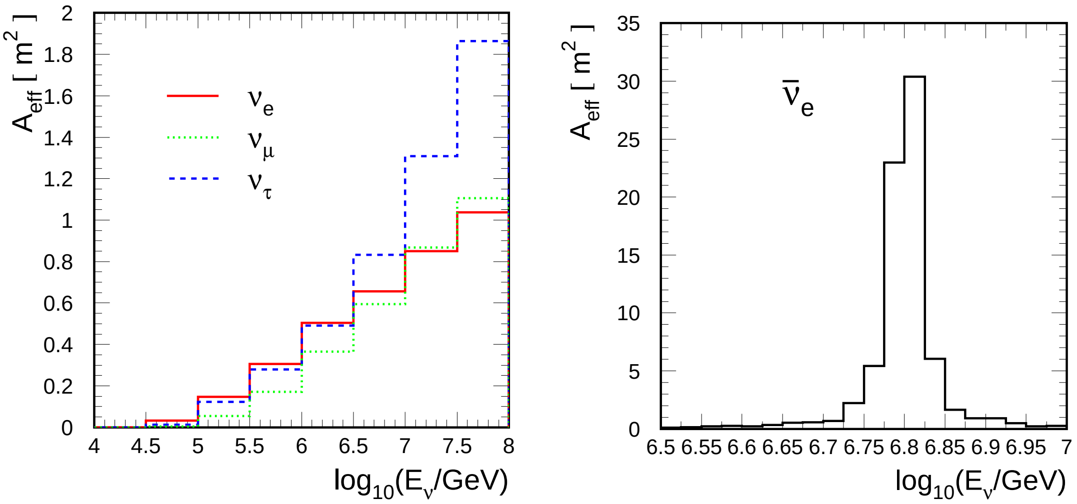

Figure 8.2.1: Left: Effective area as a function of energy for neutrinos of all flavors averaged over all angles of incidence. Right: Effective area for $\overline{\nu}_e$ due to the resonant increase of the cross-section at 6.3 PeV.

figure 8.2.1 (right). Note that the true effective area at the center energy of the resonance is even larger than shown in the plot, since the effective area is averaged over a bin of size 0.025. The average effective area for energies between $10^{6.7}$ and $10^{6.9}$ GeV, is $\overline{A_{\text{eff}}^{\overline{\nu}_e}} = \frac{1}{0.2} \cdot \int_{6.7}^{6.9} \mathrm{d}\log E\ A_{\text{eff}}(E) = 8.4\ \mathrm{m}^2$.

Ignoring the Glashow resonance, the effective detection area for all flavor neutrinos reaches 1 m^2 at about 10 PeV neutrino energies. Due to the smallness of the effective area, one might wonder what the chances are to detect an astrophysical neutrino flux. Typical ground based TeV gamma ray telescopes have effective areas a few orders of magnitude larger while the bolometric intensities of the neutrino fluxes should not exceed that of gamma-rays. The large difference in area is partially compensated by the longer observation time available for neutrino telescopes and the very different background expectations. Due to the large background of cosmic ray events, a gamma ray telescope needs a large statistics to identify a source, while already a small number of high energy neutrino events leads to a significant identification of a source.

The angular dependence of the effective area is illustrated in figure 8.2.2 for four zenith angle bins. The energy dependent absorption effects are clearly visible for $\cos(\theta) < 0$. Similar to the effective volume, ν_τ regeneration results in a larger effective area at higher energies than for the other neutrino flavors. However, the difference is less striking than for the effective volume, since the effective area already includes the interaction probability. Since the energy of the regenerated neutrinos is lower, their interaction probability is reduced.

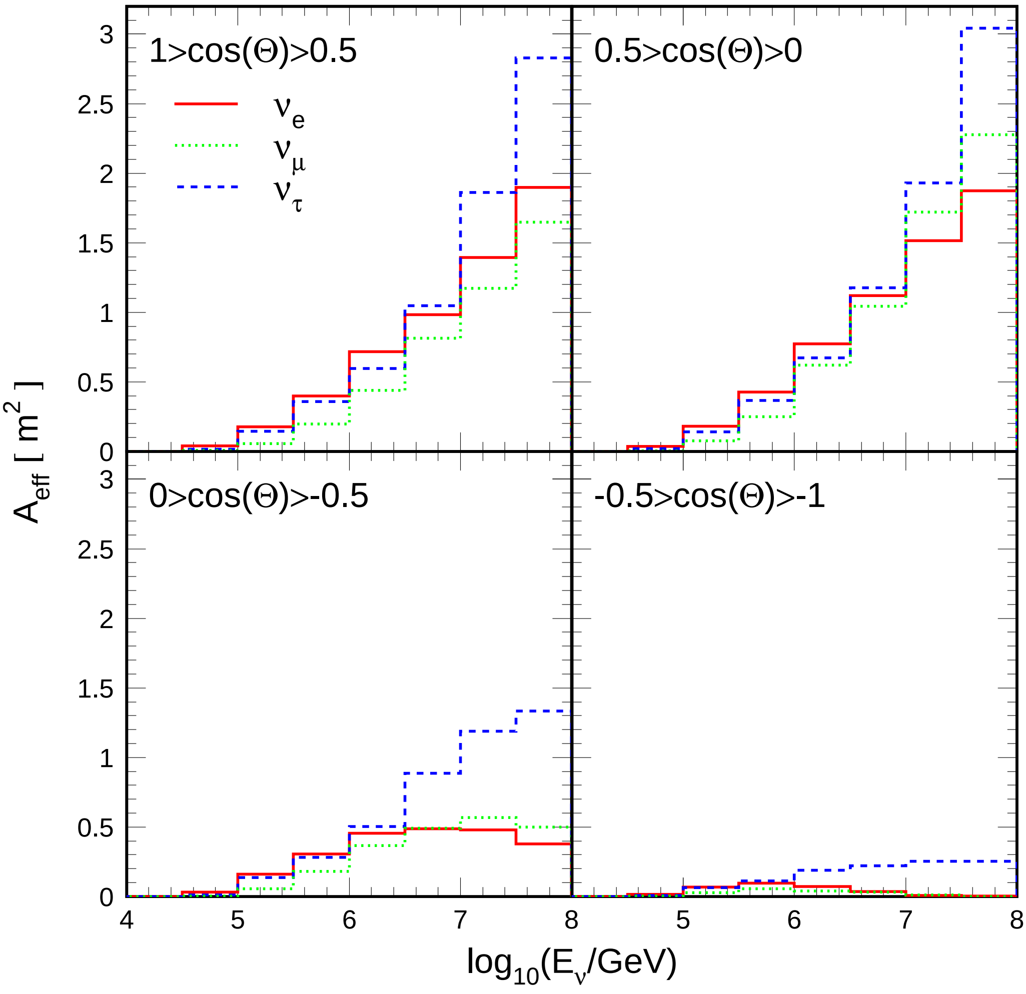

Figure 8.2.2: Effective area for ν_e, ν_μ and ν_τ as a function of the neutrino energy averaged over four different zenith angle bins.

Chapter 9

Results

The number of events remaining in the experimental data sample after application of all cuts is consistent with the expectations from atmospheric muons and neutrinos. Hence there is no evidence for a contribution due to additional sources of high energy neutrinos. As a result upper limits are derived for the diffuse flux of astrophysical neutrinos. There is, however, no fully model-independent way of presenting such limits. The consequences of this is that a large number of different approaches for presenting limits on astrophysical neutrinos have been pursued in the literature.

Here, the results will be presented in both a model dependent way as well as a *quasi model-independent* way. The advantages and the disadvantages of the two presentations will be discussed. The resulting limits will be compared to limits of other experiments. Finally, their scientific implications will be discussed in the context of potential astrophysical neutrino sources.

9.1 The Signal Event Upper Limit

One event of the experimental data of the year 2000 has passed all cuts of this analysis. The expected number of events from atmospheric muons is $0.90^{+0.69}_{-0.43}$ and that from atmospheric neutrinos is $0.06^{+0.09}_{-0.04}$. Adding these numbers (and the errors in quadrature) leads to a background prediction of $0.96^{+0.70}_{-0.43}$, which is in agreement with the observation.

What is the maximal number of signal events, μ, which is still consistent with the observation (at a certain confidence level), i.e. the signal event upper limit? Feldman and Cousins described a procedure for calculating $\mu(n_{\mathrm{obs}}, n_{\mathrm{b}})$ for any number of observed (n_{obs}) and expected background events (n_{b}) [52]. For presenting upper limits we chose a confidence level (CL) of 90 %, meaning that for a signal expectation given by $\mu_{90\%}$, an identical experiment repeated a large number of times would correctly identify the signal in more than 90 % of the cases. The signal event upper limit for this analysis is according Feldman-Cousins $\mu_{90\%} = 3.39$.

The Feldman-Cousins procedure is strictly based on frequentist statistics and does not allow for inclusion of systematic errors. Since systematic errors in AMANDA are generally non-negligible, they are incorporated into all final AMANDA results following a prescription of Cousins and Highland [43] and implemented by Conrad *et al.* [41] and Hill [80].

In these methods the limited knowledge (due to the presence of systematic uncertainties) of the signal detection efficiency and background expectation is characterized by PDFs. The upper limit is then obtained by integrating over the PDFs, thereby averaging over different configurations of signal efficiencies and background expectations. Hence the resulting event upper limit $\mu_{90\%}$ has an additional dependence on the size of the uncertainty of the signal efficiency (σ_s) and background prediction (σ_b) as well as the shape of the corresponding PDFs.

We will assume that the PDFs are represented by Gaussian functions with a width σ_s and σ_b. The estimated relative errors for signal and background are not symmetric around their mean value, so the larger one (which is the upper boundary) is chosen to represent σ_s and σ_b. For the background expectation we obtain a relative error of σ_b =73 %. As discussed in section 7.6.3, the systematic errors for the signal expectation are dependent on the spectral shape of the neutrino flux. For rather hard neutrino spectra with a spectral slope $\gamma \lesssim 2$ the systematic error was estimated to be 25 %. For a steeper spectral index $\gamma \approx 2.7$, as expected for atmospheric neutrinos due to prompt charm decay, the uncertainties rise to 50 %.

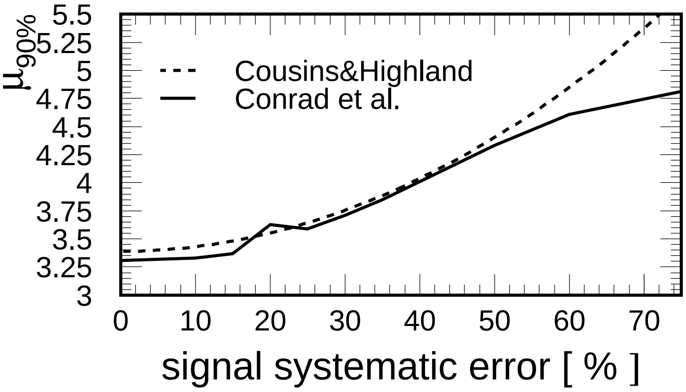

Figure 9.1.1: Signal event upper limit as a function of the relative systematic error evaluated by a method of Cousins and Highland [43] and Conrad *et al.* [41]. An uncorrelated relative systematic error of σ_b = 73 % was assumed for the uncertainties in the background expectation.

Figure 9.1.1 shows the signal event upper limit as a function of the systematic error of the signal event rate prediction, evaluated using the program *POLE* from Conrad *et al.* as well as using an analytical expression from Cousins and Highland [43]. The method of Cousins and Highland incorporates systematic errors of the signal in terms of a more standard error propagation. It assumes a well known background expectation with a negligible systematic error.

As discussed above, the method of Conrad *et al.* additionally allows to include a systematic error of the background expectation. The systematic error for the background expectation was assumed to be uncorrelated with that for the signal efficiency. The irregularities in the curve from Conrad *et al.* are inherent to the method used for calculating $\mu_{90\%}$ [80]. In the region of interest, both methods lead to comparable results and the method of Conrad *et al.* is chosen in order to be consistent with other analyzes performed by the AMANDA collaboration. The signal event upper limit increases from its value without any systematic errors by 6(28) % for $\sigma_s = 25(50)$ %.

9.2 Model Dependent Limits on the Diffuse Flux of Neutrinos

For any assumed neutrino flux prediction, one can calculate the expected event rate, N_{model}, using equation (8.2.1). A model is ruled out (at 90 % CL), if the number of signal events exceeds the event upper limit, $\mu_{90\%}$. A useful quantity is the *model rejection factor*, MRF= $\mu_{90\%}/N_{\text{model}}$, which quantifies the sensitivity for a model flux. Any flux of neutrinos $\phi_{\text{model}}(E_\nu)$ is ruled out at 90 % CL, if its strength would be rescaled to MRF $\times\, \phi_{\text{model}}(E_\nu)$.

Figure 9.2.1 shows various predictions for high energy neutrino fluxes. The total neutrino flux, which is the sum of all flavors, is presented as a function of the neutrino energy. Shown are the flux predictions for astrophysical sources such as AGNs and GRBs as well as for atmospheric neutrinos due to prompt charm production. The models were chosen such that those tested in reference [8] are included.

As discussed in section 2.3, most models for astrophysical neutrino sources predict a flux ratio of $\phi_{\nu_e} : \phi_{\nu_\mu} : \phi_{\nu_\tau} \approx 1 : 2 : 0$ at the source which is then transformed by neutrino-oscillations to a ratio close to $1 : 1 : 1$. It is possible to place limits on the flux of neutrinos of one particular flavor. However, stronger constraints on the models are obtained if limits are placed on the total neutrino flux, $\phi_\nu = \phi_{\nu_e} + \phi_{\nu_\mu} + \phi_{\nu_\tau}$. Many flux predictions were made for ν_μ without incorporating the effects of neutrino-oscillations. In these cases we correct for oscillation effects when calculating the limits.

Model	ν_e	ν_μ	ν_τ	$\nu_e + \nu_\mu + \nu_\tau$	MRF ($\frac{\mu_{90\%}}{N_{\text{model}}}$)
$10^{-6}\ E^{-2}$	2.08	0.811	1.28	4.18	0.86
SDSS	4.20	1.91	2.77	8.88	0.40
SS Blazar	2.72	1.07	1.68	5.48	0.66
MPR	0.38	0.18	0.25	0.81	4.41
SS Quasar	8.21	3.57	5.30	17.08	0.21
SP u	33.0	13.0	20.5	66.6	0.054
SP l	6.41	2.34	3.98	12.7	0.28
P $pp + p\gamma$	5.27	1.57	2.86	9.70	0.37
P $p\gamma$	0.84	0.40	0.56	1.80	1.99
WB GRB	0.0090	0.0035	0.0055	0.018	200
Charm D	0.51	0.14	0	0.65	6.66
Charm TIG	0.016	0.0039	0	0.020	216

Table 9.2.1: Event rates and model rejection factors (MRF) for models of astrophysical neutrino sources and atmospheric neutrinos due to prompt charm production. The assumed event upper limits with all uncertainties incorporated are $\mu_{90\%} = 3.61$ for the astrophysical flux models and $\mu_{90\%} = 4.35$ for the atmospheric neutrinos (see section 9.1).

Table 9.2.1 summarizes expected event rates per 197 days livetime due to neutrinos of different flavors. Additionally, the MRF for the respective model is given, which was calculated based on the sum of the events due to ν_e, ν_μ and ν_τ. A model with a MRF<1 means that the model is excluded (at 90 % CL). The various models can be grouped according to the site of neutrino production:

- AGN core models, in which neutrinos are produced in the central regions of AGNs. Protons are accelerated in the accretion flow onto a super-massive black hole and interact with the UV and X-ray fields present in the environment of AGNs. These models generally exhibit an energy cut-off around $10^5 - 10^8$ GeV. The pioneering work by Stecker *et al.* [149] (model SDSS) has been updated by their more recent work [148] (model SS Quasar). Further shown are flux predictions by Szabo and Protheroe [154] for two different maximal proton energies (model "SP u"and "SP l").

  As can be seen from table 9.2.1, these models are ruled out with MRF$\sim 0.05 - 0.4$. The physical implication of these limits will be further discussed in section 9.6.

- AGN jet models, in which highly relativistic AGN jets provide the environment for proton acceleration and neutrino production. Typically, because of lower target matter densities, the emerging neutrinos have higher cut-off energies. Shown is one of the earlier calculations by Protheroe [134], which included neutrino production through $p\gamma$ and pp collisions (model P $p\gamma$ and $pp + p\gamma$). An evaluation of the maximum flux due to a super-position of possible extragalactic sources was done by Mannheim, Protheroe and Rachen [117] (model MPR).

  A somewhat simpler model by Stecker and Salamon for neutrino production in jets of Blazars [148] (model SS Blazar) predicts a larger flux of neutrinos by normalizing to the observed extragalactic gamma ray flux (instead of the flux of cosmic rays). This model is also excluded (MRF=0.66).

  Other models of neutrino production in AGN jets include the early work by Mannheim [116] as well as the more recent model by Mücke *et al.* [124], which lead to lower or similar flux predictions as the MPR model. These models are not ruled out.

- GRB models generally result in lower neutrino flux predictions. The prediction of a model by Waxman and Bahcall [164] is shown for completeness. As can be seen from the MRF, the current sensitivity is more than two orders of magnitude too small to lead to a meaningful restrictions.

The list of models which have been tested is not complete. However, they do represent various classes of astrophysical neutrino sources. Additionally, two models for atmospheric charm production have been tested: a perturbative QCD calculation of the cross-section for charm production (Charm TIG) [69] as well as a model (Charm D) from reference [177] which is based on a non-perturbative model for the cross-sections [161].

In calculating the limits, a particular flavor composition had to be assumed. However, since neutrinos of different flavors contribute to the potential signal, the effects of neutrino oscillations on the final limits are rather small. For example, in the absence of neutrino oscillations, the model dependent limits on the total astrophysical neutrino flux worsen by

10-12 %. The limits on neutrino fluxes from charm production are unaffected by neutrino oscillations.

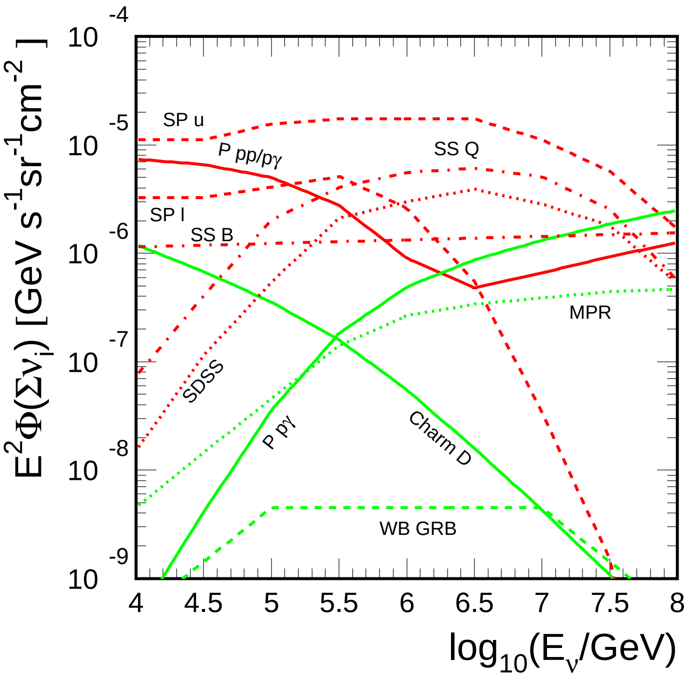

Figure 9.2.1: Flux predictions for models of astrophysical neutrinos sources. Additionally shown is a model for atmospheric neutrinos due to prompt charm production. Models represented by red curves are excluded by the results of this work. Green curves are consistent with the experimental data. The labels are explained in the text.

It is custom that any limits are calculated for neutrino fluxes with a constant slope: $\phi(E) \propto E^{-\gamma}$. This is motivated by the fact that the spectra of cosmic rays and gamma rays can be described by a single power-law for at least a few orders of magnitude in energy, as expected from Fermi-acceleration. Figure 9.2.2 shows the limits on the flux of neutrinos for γ ranging from 1 to 3. The length of each line indicates the energy range where 80 % of the events are located, while 10 % of the events have higher and 10 % have lower neutrino energies. The horizontal line represents the limit for an energy spectrum falling as E^{-2}:

$$E^2\phi(\Sigma_i\nu_i) = 0.86 \times 10^{-6}\ \mathrm{GeV\ s^{-1}\ sr^{-1}\ cm^{-2}}.$$

The upper limits shown in figure 9.2.2 are illustrative, however they have to be handled with care. An upper limit rules out a model only if it lies entirely below the predicted flux. This comes from the fact, that the limits are calculated by integrating the signal expectation over a large range of energies. The limit is presented in a differential form, however it is strictly valid only for a spectral shape as assumed in the integration. Hence, if the differentially displayed limit crosses a model prediction, the limit can not be applied to test the model. For this reason, all limits derived in this section are highly model dependent.

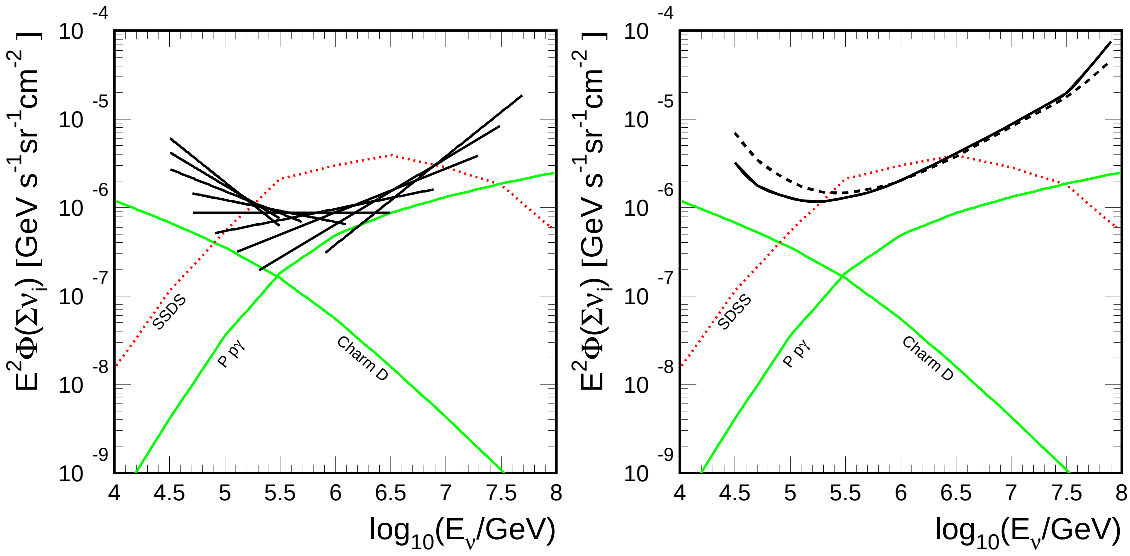

Figure 9.2.2: Left: Limits on the diffuse flux of neutrinos for different power-law spectra ($\phi(E) \propto E^{-\gamma}$) with γ ranging from 1 to 3 in steps of 0.2. The length of the lines indicate the energy range where 80 % of the events are located. Additionally shown are predictions for an AGN core model (SDSS), an AGN jet model (P $p\gamma$) and atmospheric neutrinos from prompt charm production (Charm D). Right: Quasi-differential limit as obtained according to equation (9.3.1). The full line corresponds to $\gamma = 1$ and the dashed line $\gamma = 2$.

9.3 Model Independent Limits

It is desired to present experimental limits in a form such that they are independent of any assumed spectral shape. In principle this is achieved by stating the experimental signal event upper limit, $\mu_{90\%}$, of section 9.1 combined with an energy dependent detector sensitivity (e.g. A_{eff}) which allows calculation of signal event rates. Clearly, this is not very illustrative, as it does not directly relate to the presentation of neutrino fluxes.

To obtain a limit which can be truly treated as a limit on the differential flux one has to reduce the energy range, for which a neutrino signal is assumed. The range should be small enough, such that the expected event rates do not depend strongly on the assumed spectrum shape. On the other hand, if the energy range is chosen too small, the upper limits, though nearly model independent, become very unrestrictive.

Here, we chose as an energy range one decade of energy. The limit on the flux at an energy E_0 is obtained by calculating a *moving average* of the number of events expected:

$$N(E_0) = 4\pi \times T \times \int_{E_-}^{E_+} \mathrm{d}E \; \phi_0 \; (E/E_0)^{-\gamma} \; \overline{A}_{\text{eff}}(E); \;\; E_\pm = 10^{(\log E_0 \pm 0.5)} \qquad (9.3.1)$$

ϕ_0 is a constant representing a unit flux: $\phi_0 = 1$ GeV^{-1} s^{-1} sr^{-1} cm^{-2}. A neutrino flavor ratio of 1:1:1 is assumed, which is incorporated into the average effective area: $\overline{A}_{\text{eff}}(E) = 1/3(A_{\text{eff}}^{\nu_e} + A_{\text{eff}}^{\nu_\mu} + A_{\text{eff}}^{\nu_\tau})$. The weight factor $(E/E_0)^{-\gamma}$ has been introduced to test the model dependency. An upper limit on the flux of neutrinos of energy E_0 is then given (at 90 % CL) by $\phi(E_0) = \mu_{90\%}/N(E_0) \times \phi_0$.

Figure 9.2.2 (right) shows the upper limits as a function of the neutrino energy. The limit was calculated for two spectral slopes: γ =1 and 2. As can be seen the limits differ significantly only near the threshold energy. For higher energies the model dependency is rather small. One can calculate a MRF for the limits as the minimal ratio between the flux limit and model prediction:

$$\mathrm{MRF} = \min \frac{\phi^{\mathrm{limit}}(E)}{\phi^{\mathrm{model}}(E)}$$

The limits obtained in this way have a smaller potential for rejecting specific models than model dependent limits. However, the differences in the MRFs are typically not larger than a factor of two. The advantage of presenting limits in this more model independent way is that the limit can now be interpreted differentially: A flux prediction which is crossing the upper limits is ruled out at 90 % CL. For this reason the limit derived using equation (9.3.1) will be called *quasi-differential* limit.

The strong increase in effective area at the energy of the Glashow resonance allows to set a limit on the differential flux of $\overline{\nu}_e$ at 6.3 PeV. Reoptimizing the final energy cut results in an optimal cut, $E_{\mathrm{reco}} > 0.3$ PeV. More than 98 % of the events due to the Glashow resonance which have passed all previous cuts pass the additional energy cut. The background prediction is negligible. No experimental event has been observed in that energy range, which results in a signal event upper limit $\mu_{90\%} = 2.44$ without oscillation and $\mu_{90\%} = 2.65$ assuming 25 % uncertainties in the signal expectation. The limit on the flux at 6.3 PeV is hence:

$$\phi(E = 6.3 \text{ PeV}) = \frac{\mu_{90\%}}{4\pi \times T \times \overline{A_{\mathrm{eff}}^{\overline{\nu}_e}} \times \Delta E} = 5 \times 10^{-20}\ \mathrm{GeV}^{-1}\ \mathrm{s}^{-1}\ \mathrm{sr}^{-1}\ \mathrm{cm}^{-2}$$

Here, $\overline{A_{\mathrm{eff}}^{\overline{\nu}_e}}$ represents the effective area for $\overline{\nu}_e$, averaged over an energy range given by ΔE (see section 8.2). Due to the narrow energy range (0.2 in the logarithm of the energy), the limit is rather insensitive to variations of the spectral shapes. The transformation of this limit to a limit on a total neutrino flux is not completely straightforward, since the fraction of $\overline{\nu}_e$ produced in the source is unknown. In cases of neutrino production through pp collisions one expects a ratio $\overline{\nu}_e/\nu_e \approx 1$. Hence, one would expect that about 1/6 of all neutrinos are $\overline{\nu}_e$. However, the fraction of $\overline{\nu}_e$ produced in $p\gamma$ interactions is negligible. In that case, a flux of $\overline{\nu}_e$ would emerge only due to neutrino oscillations. For the case of maximal neutrino mixing, $\overline{\nu}_e$ would constitute 1/9 of the total neutrino flux. If the mixing is non-maximal, that fraction would be even smaller. Assuming optimistically a fraction 1/6, one finds that the limit on $\overline{\nu}_e$ at 6.3 PeV is similar to the quasi-differential limit obtained by adding the contributions of neutrinos of all flavors and shown in figure 9.2.2 (right)

9.4 Comparison with Other Searches

9.4.1 Searches Performed by AMANDA

In this section the results of this work are compared to results of other searches performed by the AMANDA collaboration. The different analyzes are independent, using different filter and reconstruction techniques and result in very different final data samples with marginal overlap. In addition to being sensitive to different flavor compositions, they probe different regions of energy. So far, none of the performed searches has shown evidence for a flux of astrophysical neutrinos. Figure 9.4.1 shows the resulting quasi-differential upper limits of the various analysis calculated according to equation (9.3.1). The width of the regions represent the remaining model dependency which was evaluated by varying γ between 1 and 2 (see section 9.3).

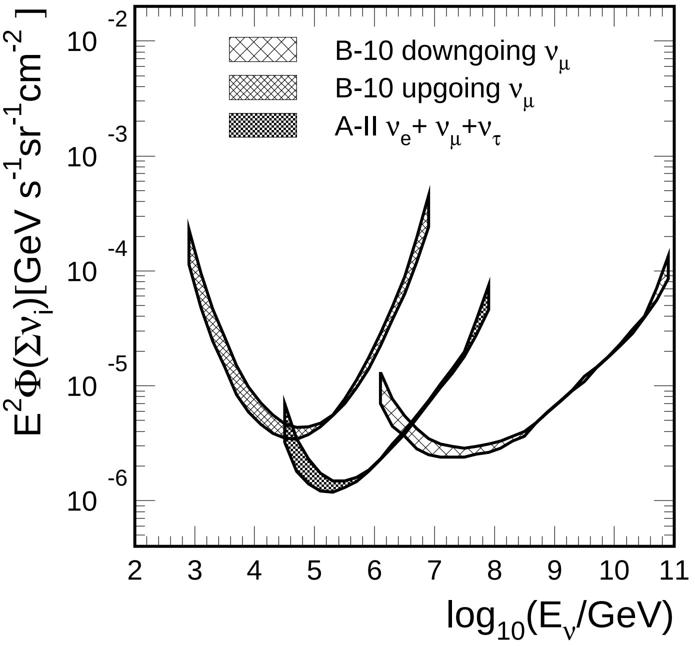

Figure 9.4.1: Comparisons of the quasi-differential limits obtained in this work with results of other analyzes performed by the AMANDA collaboration. The width of the regions represent the remaining model dependency of the limits. Specific limits for an E^{-2} spectrum are given in the text.

The AMANDA-B10 all flavor search

A search for a diffuse flux of neutrinos of all flavors was performed using the 1997 data set of the smaller AMANDA-B10 detector [9,155]. Though having a similar goal, the analysis was in many ways different from the one presented here. One of the crucial differences is that a cut on the reconstructed cascade zenith angle ($\theta_{\text{casc}} \geq 120°$) was used to reduce the background of atmospheric muons. The cut allowed to reduce the energy threshold to about 5 TeV. However, the acceptance of the detector was limited to neutrinos with a large angle of incidence and hence neutrino absorption in the Earth lead to a severely reduced sensitivity at energies above 300 TeV. The upper limits on the total flux with an E^{-2} spectrum is one order of magnitude above the limits obtained here.

The AMANDA-B10 upgoing ν_μ search

The first search performed was a search for an excess of upward moving muons from CC interactions of ν_μ [8, 112]. The advantages of searching for ν_μ are well known. The direction of the neutrino can be reconstructed rather precisely by observation of long muon tracks. Additionally, the long muon range allows to detect neutrinos interacting at large distances from the detector, resulting in a larger number of signal events in this detection channel. On the other hand the energy resolution of muon tracks is $\sigma_{\log E} \approx 0.5$ [170] and hence significantly worse than that obtained for cascades. Additionally, only a fraction of the neutrino energy is carried away by the muon. The muon has an energy which, depending on the traveled distance, is further degraded during propagation. With only a weak estimator of the neutrino energy available, the background due to the steeply falling spectrum of atmospheric neutrinos is generally larger when compared to a search for neutrino induced cascades. Since the search focuses on upward moving neutrinos, absorption in the Earth is limiting the maximum expected neutrino energies.

No excess above the background of atmospheric neutrinos was found in the 1997 data of the AMANDA-B10 detector. With 3 events observed and 3.06 expected a signal upper limit of $\mu_{90\ \%} = 4.75$ was obtained, leading to a limit on the flux of ν_μ for an energy spectrum following E^{-2}:

$$E^2 \phi_{\nu_\mu} = 0.84 \times 10^{-6}\ \mathrm{GeV\ s^{-1}\ sr^{-1}\ cm^{-2}}.$$

The predominant energy range is 6 TeV to 1 PeV.

Additionally the final cuts where optimized with respect to different model predictions, resulting in model dependent signal event upper limits. For calculating the limit shown in figure 9.4.1 the constant signal event upper limit $\mu_{90\%} = 4.75$ as well as the expected signal event rates as published in [8] were used.

A preliminary analysis of the 2000 data has shown that AMANDA-II is about three times more sensitive than the smaller AMANDA-B10 detector.

The AMANDA-B10 Downgoing ν_μ Search

By looking for highly energetic muon tracks one can extend the search for ν_μ to arrival directions above the horizon [84]. However, the large background of atmospheric muons results in a high energy threshold of a few PeV for this analysis. The main contribution to the signal event rate stems from neutrinos from horizontal directions, where the effective target matter is larger than for vertically downward directions, but not too large as to lead to neutrino absorption. The 1997 data set was analyzed and 6 events where observed while 8.3 are expected from atmospheric muons. A signal event upper limit of $\mu_{90\ \%} = 3.6$ was obtained, leading to an upper limit for a flux of ν_μ with an energy spectrum following E^{-2}:

$$E^2 \phi_{\nu_\mu} = 0.72 \times 10^{-6}\ \mathrm{GeV\ s^{-1}\ sr^{-1}\ cm^{-2}}.$$

The predominant energy range is 2.5 PeV to 600 PeV. A preliminary analysis of the 2000 data indicates that for this channel AMANDA-II is about three times more sensitive than the smaller AMANDA-B10 detector.

9.4.2 Searches Performed by Other Experiments

Other experiments aim at detecting a diffuse flux of neutrinos as well. Here, the emphasis is on those experiments which are currently operating and which have competitive sensitivities. For further reviews on this subject see [146, 110].

The BAIKAL collaboration has published an upper limit on the diffuse flux of neutrinos of all flavors [173]. They filter out bright events which pass simple selection criteria. The vertex position or energy of the events are not reconstructed. Zero events of a three year data sample (502 days) have passed all selection criteria. Upper limits are obtained which are about 50 % worse than the one presented here. The energy ranges for which the limits are valid are roughly the same.

The RICE experiment, which aims at detecting a radio Cherenkov signal from electromagnetic and hadronic neutrino vertex cascades has published an updated limit [106] using three years of experimental data. The energy threshold of their analysis is about 100 PeV with an effective volume which is slowly increasing with energy. They have observed no event candidates resulting in an upper limit on the flux of neutrinos with an E^{-2} spectrum, which is comparable with that of the AMANDA-B10 downgoing ν_μ search.

Other limits on the diffuse flux of muon neutrinos have been obtained by the MACRO [15] and Frejus collaborations [139]. Their limits are more than one order of magnitude worse than the limits obtained here. Published data from the AGASA and Fly's Eyes experiment have been used to derive upper limit on the flux of neutrinos with energies above 100 PeV [16]. These limits are less restrictive than the limits from AMANDA and RICE discussed above.

9.5 Limits on Point Sources

So far, detection of a potential diffuse flux has been considered. However, it is possible that the total neutrino flux is dominated by only a few sources of fixed location in the sky. In this section we calculate upper limits on the flux from such *point sources.* In the detector coordinates of AMANDA, the location of a point source is spread evenly over a constant declination band. A flux of neutrinos from the direction of the source, $\phi(E)$, will result in the average number of events,

$$N_{\text{event}}^{\text{source}} = T \int \mathrm{d}E_\nu \; \phi(E_\nu) A_{\text{eff}}(E_\nu, \theta_{\text{source}}) \tag{9.5.1}$$

The sensitivity for the given flux can again be expressed by the model rejection factor, MRF=$\mu_{90\%}/N_{\text{event}}^{\text{source}}$. If MRF<1, the predicted flux is ruled out by the observation (at 90 % CL). Figure 9.5.1 shows the largest possible flux consistent with the observation (MRF=1), where a spectral shape: $\phi(E) \propto E^{-2}$ was assumed. As previously, the systematic uncertainty in the signal efficiency (25 %) and background prediction (73 %) is included in the event upper limit $\mu_{90\%} = 3.61$. The upper limit is nearly constant for positive declinations, while it worsens for negative declinations due to neutrino attenuation in the Earth. Note that, in case of a possible detection of a signal, the current angular resolution of neutrino-induced cascades would be too poor to allow its localization.

Additionally shown is the sensitivity obtained from a dedicated search for point sources using ν_μ-induced muon events [75] with the AMANDA-II detector. In that analysis, the sky is divided into 301 independent search bins and for each bin an upper limit is calculated. The sensitivity represents the average upper limit for a given declination (in the absence of a signal). The sensitivity is more than one order of magnitude better for negative declinations, which is attributed to the larger effective neutrino area for ν_μ and the good angular resolution ($2.0° - 2.5°$ in the median of the angular mismatch), which allows to reduce the background of atmospheric neutrino events to a few per search bin. For negative declinations, the background of atmospheric muons is responsible for considerably worse upper limits.

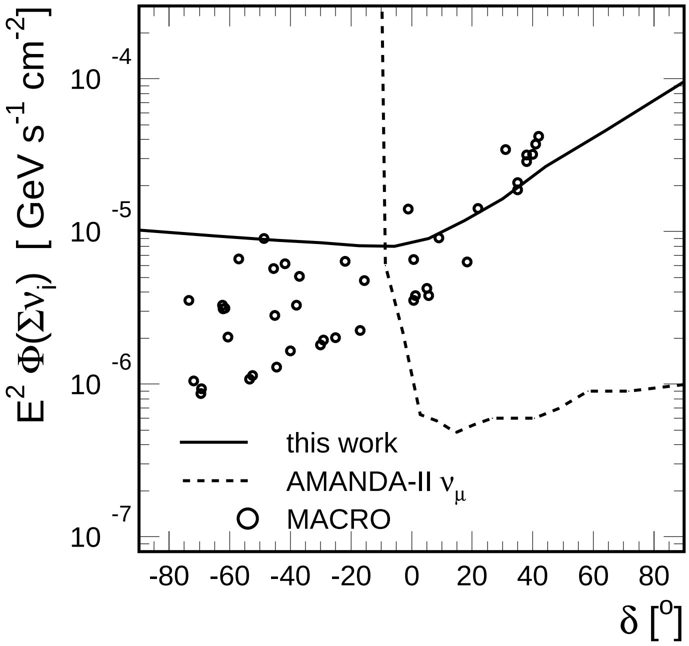

Figure 9.5.1: Limit on the flux of neutrinos of all flavors from point sources as a function of the declination of the source. A ratio of neutrino flavors of 1:1:1 was assumed.

Additionally shown are upper neutrino flux limits for 42 selected source as obtained by the MACRO collaboration [14]. Since the MACRO experiment is located on the northern hemisphere, the limits are better for negative declinations. MACRO has provided upper limits for an $E^{-2.1}$ spectrum by stating the integral flux of neutrinos above 1 GeV. The limit was translated to a limit on a E^{-2} spectrum by renormalizing the flux by the ratio of integral number of events,

$$\int_{1\ \mathrm{GeV}}^{\infty} E^{-2.0}\mathrm{d}E \Big/ \int_{1\ \mathrm{GeV}}^{\infty} E^{-2.1}\mathrm{d}E = 1.1.$$

For most sources, the MACRO limits are more restrictive than the limits obtained here. However, this changes if harder spectra are considered. Since the typical neutrino energies which contribute to the event expectations of the analysis presented here are one order of magnitude higher, the limits become comparable or better for spectral slopes $\gamma \lesssim 1.5$.

The Super-Kamiokande collaboration has published limits on the flux of neutrino-induced muons from a few selected point sources [163]. They did not publish limits on the neutrino flux, however it can be expected that the Super-Kamiokande sensitivity is not very different from that of the MACRO experiment. Summarizing, the upper limits on points sources in the northern hemisphere illustrate a sensitivity which, depending on the assumed spectral shape, is competitive with that of other experiments. Certainly, assuming an improved angular resolution and using directional information, the sensitivity could still be increased.

9.6 Discussion of the Limits

The result of this work currently represents the most restrictive limit on the diffuse flux of neutrinos in the energy region from 50 TeV to about 5 PeV. What is the astrophysical relevance of these limits? To answer this question one can look at the models which have been ruled out. Besides the two main model categories, namely neutrino production in the core and jets, an example for a more exotic astrophysical flux model is discussed.

AGN core models: As shown in section 9.2 the original models for neutrino production in AGN cores are inconsistent with the experimental data. This does not mean that the models are conceptually wrong, but only that the assumed parameters of the models have been chosen too optimistic. For example, Stecker and Salamon [148] make the more or less *ad hoc* assumption that 30 % of the observed quasar X-ray luminosity is due to electromagnetic cascades originating from π^0 production. Hence ruling out the Stecker & Salamon model with a MRF≈ 0.2 is equivalent to reducing the non-thermal contribution in the model to MRF$\times$30 % $\approx$ 6 %. Note that for selected quasars, the X-ray spectrum can be well described by thermal radiation with at most a 15 % contribution due to non-thermal processes [179]. Accepting the non-thermal hadronic model of Stecker & Salamon, its constrains can be strengthened. This illustrates the astrophysical relevance of the limit. Similar constrains can be derived for other AGN core models.

A recent model for proton interaction in AGN cores intends to explain the uniform large scale jet structures observed in X-rays [127]. In this model a nearly monoenergetic beam of protons of energy E_p produces gamma rays and neutrinos with energies $E_{\nu/\gamma} \sim E_p/20$. The diffuse flux of neutrinos for this model was evaluated in [95]. Unlike in the other AGN core models, the energy released into neutrinos cannot be lowered without consequences, i.e. without a loss of motivation. This model is not yet ruled out, however the allowed parameter space of the model can be constrained. The contributing initial proton energies are bounded from below, $E_p \gtrsim 30$ PeV, which is one order of magnitude below the natural scale of the model. It is expected that the full parameter space of the model will be tested by an analysis covering a few years of AMANDA data.

AGN jet models: AGN jet models, in contrast to the core models, typically allow predictions of neutrinos of higher energies due to lower target densities. These models are attractive as they often forsee the acceleration of cosmic rays up to the highest energies observed. Only the simplest and most optimistic of these models can currently be ruled out and the more realistic models are still not probed. The models which assume optically thick environments generally predict larger fluxes of neutrinos and could be tested by a future analysis covering a few years of AMANDA data [134, 117].

Models for neutrino production in AGN jets which assume optically thin environments are astrophysically more favored [24]. However, for these models to be consistent with the observed spectrum of cosmic rays, the predicted flux is so low that only next generation neutrino detectors are expected to observe them.

Other models: The limits obtained here are valid at energies which are rather low compared to the energies of the highest energy cosmic rays. Nevertheless, for some more speculative cosmic ray production mechanisms they do represent meaningful bounds. To give an example: the *Z-burst* mechanism assumes that a large flux of neutrinos with $E_\nu \gtrsim 10^{21}$ eV is emitted from extra-galactic sources, which then interacts with cosmic relic neutrinos through resonant Z-boson production and thereby produces a local flux of energetic protons [166,50]. This model has obtained considerable interest as it circumvents the GZK cut-off (see section 2.1). However, the potential astrophysical sources of these high energy neutrinos are highly constrained. Optically thin sources would produce, along with protons and neutrinos, a large flux of γ-rays, thereby exceeding the observation of EGRET [94] (see section 2.4.4). As shown in [70], this EGRET bound can be avoided when assuming optically thick sources. The flux of secondary neutrinos from such sources was evaluated, and in the energy range from 100 TeV to 100 PeV it can be described by a power-law, $\phi \propto E^{-1.75}$ [70]. While the model was consistent with previous upper bounds, it is ruled out (with a MRF=0.3) by the limits presented here.

Chapter 10

Summary

The subject of this dissertation was the search for a diffuse flux of high energy neutrinos using the data collected with the AMANDA-II detector during the year 2000. In particular this work focused on the detection of neutrino-induced cascades. The signature of a charged current interaction of ν_e and ν_τ is a hadronic and/or electro-magnetic cascade. Additional cascade events from all neutrino flavors are obtained from neutral current interactions.

Methods for reconstructing cascades were further improved or newly developed. Where possible, the performance of the reconstruction was tested with in-situ light sources. A Monte Carlo generator was developed, which allows state-of-the-art simulation of all-flavor neutrino events.

A dedicated filter was designed which aimed at reducing the large background of atmospheric muons, while keeping a high efficiency for neutrino-induced cascades. For simulating the background due to atmospheric muons, an optimized simulation chain was developed. This allowed an optimization of the final cuts using simulated data.

The first year of data of the AMANDA-II detector was searched for neutrino induced cascades and one candidate event was found while $0.96^{+0.70}_{-0.43}$ are expected due to muons and neutrinos produced in the atmosphere. The number of observed events is consistent with the expected background, hence upper limits on an additional signal contribution were calculated. The systematic error on both signal efficiency (25 % for a spectral index: $\gamma \leq 2$) and background expectation was incorporated into the limits.

Upper limits were presented in both a model-dependent and quasi model-independent way. The model independent way of presenting limits allowed to compare the results of different analyzes. The upper limits in the energy range between 50 TeV and 5 PeV as obtained in this work are currently the most restrictive ones available, ruling out several models for astrophysical neutrino production. Since neutrinos of all flavors contribute to the potential signal, the effects of neutrino oscillations on the final limits are rather small.

Chapter 11

Outlook

The search for neutrino-induced cascades with AMANDA-II has revealed a large sensitivity for detection of high energy astrophysical neutrino fluxes. Nevertheless, since the analysis of cascade-like events is the first one performed with AMANDA-II, there remain a few open questions. Some of them are listed below.

Can the analysis be improved?
So far, only the first year of data of the completed AMANDA-II detector was used. The data of the years 2001 and 2002 have a similar or larger livetime than the analyzed data set of the year 2000. By re-optimizing the final cuts to a larger data sample, the background expectation can be kept low. The increase in sensitivity, if compared to the presented analysis, is close to a factor of three.

The first level filter was designed to have a high passing rate for both low energy atmospheric and high energy astrophysical neutrino events. Since only events with a reconstructed energy of $E_{\mathrm{reco}} > 50$ TeV pass the final energy cut, the first level filter could be readjusted accordingly. By focusing on higher energy events only, the neutrino passing rate during data processing could possibly be increased.

A future analysis would benefit from further improvements in the simulation of experimental data. The largest contribution to the systematic uncertainty in the background expectation is due to limited statistics of simulated atmospheric muon events. A larger statistics and better agreement between simulated and experimental data distributions would allow to improve the cut selection and hence the neutrino passing rate.

What can one expect from the hardware upgrade?
Since the year 2003, the AMANDA-II detector has a newly installed Flash ADC system. It is expected that the significant increase in linearity of the amplitude response allows to improve the reconstruction of cascade-like events. The light intensities in the close vicinity of the cascade holds valuable information, since photons typically are less scattered. For example, the forward backward asymmetry of the emitted light from a cascade is significantly more pronounced at closer distances. It can be expected, that new algorithms using the amplitude information will improve the reconstruction of the cascade direction. A benefit would be a significant increase in sensitivity for point sources. This is not unreasonable: Already now, the current limit is competitive with other limits for the southern

sky obtained by MACRO and Super-Kamiokande. In case of detection of a signal, a better angular resolution would possibly allow the identification of its source.

The energy reconstruction will also benefit from the hardware upgrade. Besides improving the energy resolution, one could reduce the systematic uncertainties in the total energy scale. This is related to the fact, that by measuring the near field of the light of a cascade instead of the far field, one would reduce the effects of the optical ice properties.

Can one measure the flux of atmospheric neutrinos with cascades?
In order to measure at least a few neutrino-induced cascades from atmospheric neutrinos, the energy threshold of the analysis would have to be lowered by at least one order of magnitude. At the same time, the background due to atmospheric muon events would have to be reduced by more than two orders of magnitude, in order to keep it significantly below the expected number of atmospheric neutrino events. The discrimination potential of the variables which have been inspected so far are not powerful enough to fulfill this requirement.

Improvements in the reconstruction of the cascade direction would allow a reduction of the background of atmospheric muons by demanding that the cascade is upgoing. Possibly, such an improved reconstruction can be developed based on the newly available amplitude information from the Flash ADC system. Depending on the performance of such new algorithms, one might become sensitive to atmospheric neutrinos.

What can one expect from IceCube?
The successor to AMANDA is the IceCube detector. IceCube will consist of 80 strings and 4800 OMs distributed within a volume of approximately 1 km^3 [85]. The effective volume should be approximately 100 times larger than the one obtained in this analysis. The large size of the instrumented volume and the full digital pulse shape information should allow to separate neutrino-induced cascades from the background of atmospheric muons events with significantly higher efficiency. For example, one can use the outer strings of IceCube as a veto shield.

When searching for astrophysical neutrinos, the dominant background will presumably be atmospheric neutrinos. Raising the threshold energy to 100 TeV will reduce this background to less than 1 event per year. It is believed that the sensitivity of the instrument will be a factor of 100 better than that of the present AMANDA-II detector.

Once neutrino telescopes will see first evidence for an astrophysical neutrino flux, it will be only weak. It is the complementarity of the different detection channels, namely good angular resolution of energetic muon tracks in the case of CC ν_μ interactions and good energy resolution in the case of cascade-like events due to neutrinos of all flavor, which will add confidence to the observation and allow its further interpretation.

Bibliography

[1] Achard, P. *et al.*, Standard model Higgs boson with the L3 experiment at LEP. *Phys. Lett.* **B517**:319 (2001).

[2] Agostinelli, S. *et al.*, GEANT4: A simulation toolkit. (2002), SLAC-PUB-9350.
URL `http://wwwinfo.cern.ch/asd/geant4.html`

[3] Agrawal, V. *et al.*, Atmospheric neutrino flux above 1 GeV. *Phys. Rev.* **D53**:1314 (1996).

[4] Aharonian, F. *et al.*, Variations of the TeV energy spectrum at different flux levels of Mkn 421 observed with the HEGRA system of Cherenkov telescopes. *Astron. Astrophys.* **393**:89 (2002).

[5] Ahmad, Q. R. *et al.*, Direct evidence for neutrino flavor transformation from neutral-current interactions in the Sudbury Neutrino Observatory. *Phys. Rev. Lett.* **89**:011301 (2002).

[6] Ahn, M. H. *et al.*, Indications of neutrino oscillation in a 250-km long-baseline experiment. *Phys. Rev. Lett.* **90**:041801 (2003).

[7] Ahrens, J. *et al.*, Observation of high energy atmospheric neutrinos with the Antarctic Muon and Neutrino Detector Array. *Phys. Rev.* **D66**:012005 (2002).

[8] Ahrens, J. *et al.*, Limits on diffuse fluxes of high energy extraterrestrial neutrinos with the AMANDA-B10 detector. *Phys. Rev. Lett.* **90**:251101 (2003).

[9] Ahrens, J. *et al.*, Search for neutrino-induced cascades with the AMANDA detector. *Phys. Rev.* **D67**:012003 (2003).

[10] Alvarez-Muñiz, J., Halzen, F. and Hooper, D. W., High Energy Neutrinos from Gamma Ray Bursts: Event Rates in Neutrino Telescopes. *Phys. Rev.* **D62**:093015 (2000).

[11] Alvarez-Muñiz, J. *et al.*, Comparative study of simulations of Cerenkov radio emission from high energy showers in dense media. (2002), astro-ph/0206043.

[12] AMANDA, Optical Module Data Base. (2001), unpublished.
URL `http://area51.berkeley.edu/amanda-private/omdb/`

[13] AMANDA, Siegmund - User Manuals. (2003).
URL `http://amanda.wisc.edu/software/siegmund/manuals.shtml`

[14] Ambrosio, M. *et al.*, Neutrino astronomy with the MACRO detector. *Astrophys. J.* **546**:1038 (2001).

[15] Ambrosio, M. *et al.*, Search for diffuse neutrino flux from astrophysical sources with MACRO. *Astropart. Phys.* **19**:1 (2003).

[16] Anchordoqui, L. A. *et al.*, Neutrino bounds on astrophysical sources and new physics. *Phys. Rev.* **D66**:103002 (2002).

[17] Andrés, E. *et al.*, The AMANDA neutrino telescope: principle of operation and first results. *Astropart. Phys.* **13**(1):1 (2000).

[18] Apollonio, M. *et al.*, Limits on neutrino oscillations from the CHOOZ experiment. *Phys. Lett.* **B466**:415 (1999).

[19] Arkani-Hamed, N., Dimopoulos, S. and Dvali, G. R., The hierarchy problem and new dimensions at a millimeter. *Phys. Lett.* **B429**:263 (1998).

[20] Askebjer, P. and the AMANDA Collaboration, Optical Properties of Deep Ice at the South Pole: Absorption. *Science* (267):1147 (1995).

[21] Athanassopoulos, C. *et al.*, Evidence for $\nu_\nu \rightarrow \nu_e$ neutrino oscillations from LSND. *Phys. Rev. Lett.* **81**:1774 (1998).

[22] Athar, H., Jezabek, M. and Yasuda, O., Effects of neutrino mixing on high-energy cosmic neutrino flux. *Phys. Rev.* **D62**:103007 (2000).

[23] Bahcall, J. N., Gonzalez-Garcia, M. C. and Pena-Garay, C., Before and after: How has the SNO neutral current measurement changed things? *JHEP* **07**:054 (2002).

[24] Bahcall, J. N. and Waxman, E., High Energy Astrophysical Neutrinos: the Upper Bound is Robust. *Phys. Rev.* **D64**:023002 (2001).

[25] Bahcall, J. N. and Waxman, E., Has the GZK cutoff been discovered? *Phys. Lett.* **B556**:1 (2003).

[26] Balkanov, V. A. *et al.*, Registration of atmospheric neutrinos with the BAIKAL Neutrino Telescope NT-96. *Astropart. Phys.* **12**(1–2):75 (1999).

[27] Beacom, J. F. *et al.*, Decay of high-energy astrophysical neutrinos. *Phys. Rev. Lett.* **90**:181301 (2003).

[28] Becka, T., Experience with 2001 online processing – and proposal for 2002. AMANDA Internal Report 20020102 (2002), unpublished.

[29] Berezinsky, V. S., Super-GZK neutrinos: Testing physics beyond the standard model. (2003), hep-ph/0303091.

[30] Berezinsky, V. S. and Zatsepin, G. T., Cosmic rays at ultrahigh-energies (neutrino?). *Phys. Lett.* **B28**:423 (1969).

[31] Bhattacharjee, P., Hill, C. T. and Schramm, D. N., Grand unified theories, topological defects and ultrahigh- energy cosmic rays. *Phys. Rev. Lett.* **69**:567 (1992).

[32] Bhattacharjee, P. and Sigl, G., Origin and propagation of extremely high energy cosmic rays. *Phys. Rept.* **327**:109 (2000).

[33] Brucher, L., Keranen, P. and Maalampi, J., Searching scalar resonances with ultra-high energy neutrinos. *JHEP* **05**:060 (2001).

[34] Brun, R. and Rademakers, F., ROOT - An Object-Oriented Data Analysis Framework. *Nucl. Instrum. Meth. A* **389**:81 (1997).
URL `http://root.cern.ch/`

[35] Bugaev, E. V., Sokalski, I. A. and Klimushin, S. I., Simulation accuracy of long range muon propagation in medium: Analysis of error sources. (2000), hep-ph/0010323.

[36] Bugaev, E. V. *et al.*, Prompt Leptons in Cosmic Rays. *Nuovo Cim.* **C12**:41 (1989).

[37] Cavallon, G., On the sources of ultra-high energy cosmic rays. *Astron. and Astrophys.* **65**:415 (1978).

[38] Chirkin, D., Cosmic Ray spectrum measured with AMANDA-II. In Kajita *et al.* [93], pages 1311–1214.

[39] Chirkin, D. and Rhode, W., Muon Monte Carlo: A new high-precision tool for muon propagation through matter. In Wischnewski [172], pages 15–22.

[40] Chirkin, D. and Rhode, W., Muon Monte Carlo: A new high precision tool for muon propagation through matter. In Heinzelmann *et al.* [78], pages 1017–1020.

[41] Conrad, J. *et al.*, Including systematic uncertainties in confidence interval construction for Poisson statistics. *Phys. Rev.* **D67**:012002 (2003).

[42] Costa, C. G. S., The prompt lepton cookbook. *Astropart. Phys.* **16**:193 (2001).

[43] Cousins, R. D. and Highland, V. L., Incorporating systematic uncertainties into an upper limit. *Nucl. Instrum. Meth.* **A320**:331 (1992).

[44] Cowen, D. F., Hanson, K. *et al.*, Time Calibration of the AMANDA Neutrino Telescope with Cosmic Ray Muons. In Heinzelmann *et al.* [78], pages 1133–1136.

[45] Dimopoulos, S. and Landsberg, G., Black holes at the LHC. *Phys. Rev. Lett.* **87**:161602 (2001).

[46] Drury, L. O. *et al.*, Tests of galactic cosmic ray source models. (2001), astro-ph/0106046.

[47] Dziewonski, A. M. and Anderson, D. L., Preliminary Reference Earth Model (PREM). *Phys. Earth. Planet. Inter.* **25**:297 (1981).

[48] Eguchi, K. *et al.*, First results from KamLAND: Evidence for reactor anti- neutrino disappearance. *Phys. Rev. Lett.* **90**:021802 (2003).

[49] Engel, R. and Stanev, T., Neutrinos from propagation of ultra-high energy protons. *Phys. Rev.* **D64**:093010 (2001).

[50] Fargion, D., Mele, B. and Salis, A., Ultrahigh energy neutrino scattering onto relic light neutrinos in galactic halo as a possible source of highest energy extragalactic cosmic rays. *Astrophys. J.* **517**:725 (1999).

[51] Farzan, Y. and Smirnov, A. Y., Leptonic unitarity triangle and CP-violation. *Phys. Rev.* **D65**:113001 (2002).

[52] Feldman, G. J. and Cousins, R. D., Unified approach to the classical statistical analysis of small signals. *Phys. Rev.* **D57**:3873 (1998).

[53] Fermi, E., On the Origin of Cosmic Radiation. *Phys. Rev.* **75**:1169 (1949).

[54] Fermi, E., Galactic Magnetic Fields and the Origin of Cosmic Radiation. *Astrophys. J.* **119**:1 (1954).

[55] Friess, J. J., Han, T. and Hooper, D., TeV string state excitation via high energy cosmic neutrinos. *Phys. Lett.* **B547**:31 (2002).

[56] Fukuda, Y. *et al.*, Evidence for Oscillation of Atmospheric Neutrinos. *Phys. Rev. Lett.* **81**(8):1562 (1998).

[57] Gabriel, T. A. *et al.*, Energy dependence of hadronic activity. *Nucl. Instrum. Meth. A* **338**:336 (1994).

[58] Gaisser, T. K., *Cosmic Rays and Particle Physics*. Cambridge University Press, UK, first edition (1990), ISBN 0-521-32667-2.

[59] Gaisser, T. K. and Honda, M., Flux of atmospheric neutrinos. *Ann. Rev. Nucl. Part. Sci.* **52**:153 (2002).

[60] Gaisser, T. K., Steigman, G. and Tilav, S., Limits on Cold Dark Matter Candidates from Deep Underground Detectors. *Phys. Rev.* **D34**:2206 (1986).

[61] Gandhi, R. *et al.*, Ultrahigh-energy neutrino interactions. *Astropart. Phys.* **5**(2):81 (1996).

[62] Gandhi, R. *et al.*, Neutrino interactions at ultrahigh energies. *Phys. Rev.* **D58**:093009 (1998).

[63] Gazizov, A. Z. and Yanush, S. I., Small-x Growth of Nucleon Structure Functions and Its Manifestations in Ultrahigh-Energy Neutrino Astrophysics. (2001), astro-ph/0112244.

[64] Gazizov, A. Z. and Yanush, S. I., On hard pomeron enhancement of ultrahigh-energy neutrino nucleon cross-sections. *Phys. Rev.* **D65**:093003 (2002).

[65] Giddings, S. B. and Thomas, S., High energy colliders as black hole factories: The end of short distance physics. *Phys. Rev.* **D65**:056010 (2002).

[66] Ginzburg, V. L. *et al.*, *Astrophysics of cosmic rays*. Elsevier Science, Amsterdam, Netherlands (1990), ISBN 0-444-88641-9.

[67] Glashow, S., Resonant Scattering of Antineutrinos. *Phys. Rev.* **118**:316 (1960).

[68] Goldschmidt, A. *et al.*, The ICECUBE detector. In Heinzelmann *et al.* [78], pages 1237–1240.

[69] Gondolo, P., Ingelman, G. and Thunman, M., Charm production and high energy atmospheric muon and neutrino fluxes. *Astropart. Phys.* **5**:309 (1996).

[70] Gorbunov, D. S., Tinyakov, P. G. and Troitsky, S. V., Constraints on ultra-high energy neutrinos from optically thick astrophysical accelerators. *Astropart. Phys.* **18**:463 (2003).

[71] Greisen, K., End to the cosmic ray spectrum? *Phys. Rev. Lett.* **16**:748 (1966).

[72] Gribov, V. N. and Pontecorvo, B., Neutrino astronomy and lepton charge. *Phys. Lett.* **B28**:493 (1969).

[73] Halzen, F. and Hooper, D. W., Neutrino Event Rates from Gamma Ray Bursts. *Astrophys. J. (Letters)* **527**(2):L93 (1999).

[74] Haungs, A., Energy spectrum and mass composition around the knee by EAS measurements. *J. Phys.* **G29**:809 (2003).

[75] Hauschildt, T., Steel, D. *et al.*, Search for Extraterrestrial Point Sources of Neutrinos with AMANDA-II. In Kajita *et al.* [93], pages 1305–1308.

[76] He, Y. D. and Price, P. B., Remote Sensing of Dust in Deep Ice at the South Pole. *Journal Geophysical Research* **103**(14):17041 (1998).

[77] Heck, D. *et al.*, CORSIKA: A Monte Carlo code to simulate extensive air showers. Wissenschaftlicher Bericht FZKA 6019, Forschungszentrum Karlsruhe, Karlsruhe, Germany (1998), see also http://www-ik3.fzk.de/∼heck/corsika.
URL `http://hikwww4.fzk.de/hbk/literatur/FZKA_Berichte/FZKA6019.pdf`

[78] Heinzelmann, G., Kampert, K.-H. and Spiering, C., editors, *Proceedings of the* 27^{th} *International Cosmic Ray Conference*, Hamburg, Germany (2001).

[79] Hill, G., Karle, A. and Desiati, P., Evidence for insufficient absorption in the AMANDA Monte Carlo. (2001).
URL `amanda.physics.wisc.edu/ghill/absorption/absorption.html`

[80] Hill, G. C., Comment on [Including systematic uncertainties in confidence interval construction for Poisson statistics]. *Phys. Rev.* **D67**:118101 (2003).

[81] Hill, G. C. and Rawlins, K., Unbiased cut selection for optimal upper limits in neutrino detectors: The model rejection potential technique. *Astropart. Phys.* **19**:393 (2003).

[82] Hoerandel, J. R., On the knee in the energy spectrum of cosmic rays. *Astropart. Phys.* **19**:193 (2003).

[83] Hundertmark, S., AMASIM Neutrino Detector Simulation Program. In Spiering [145], pages 276–286.

[84] Hundertmark, S. *et al.*, AMANDA-B10 Limit on UHE Muon Neutrinos. In Kajita *et al.* [93], pages 1309–1312.

[85] IceCube Collaboration, IceCube Preliminary Design Report (2001).
URL `http://icecube.wisc.edu/science/sci-tech-docs/`

[86] Information Technology Division, *PAW – Physics Analysis Workstation; User's Guide*. CERN Program Library Long Writeup Q121, Geneva, Switzerland (1999).
URL `ftp://asisftp.cern.ch/cernlib/doc/ps.dir/paw.ps.gz`

[87] Ingelman, G. and Thunman, M., Particle Production in the Interstellar Medium. (1996), hep-ph/9604286.

[88] Inoue, S. and Takahara, F., Electron acceleration and gamma-ray emission from blazars. *Astrophys. J.* **463**:555 (1996).

[89] J. Schwindling, B. M. and Couet, O., *Using Multi-Layer Perceptrons in PAW*. CERN Program Library, Geneva, Switzerland.
URL `http://wwwinfo.cern.ch/asd/paw/ps/mlpfit/pawmlp.html`

[90] Jackson, J. D., *Classical Electrondynamics*. Wiley, New York, USA, third edition (1996).

[91] Jadach, S. *et al.*, The tau decay library TAUOLA: Version 2.4. *Comput. Phys. Commun.* **76**:361 (1993).

[92] Jungman, G., Kamionkowski, M. and Griest, K., Supersymmetric dark matter. *Phys. Rept.* **267**:195 (1996).

[93] Kajita, T. *et al.*, editors, *Proceedings of the 28th International Cosmic Ray Conference*, Tsukuba, Japan (2003).

[94] Kalashev, O. E. *et al.*, Ultra-high energy cosmic rays from neutrino emitting acceleration sources? *Phys. Rev.* **D65**:103003 (2002).

[95] Kalashev, O. E. *et al.*, Ultra-high energy neutrino fluxes and their constraints. *Phys. Rev.* **D66**:063004 (2002).

[96] Karle, A., Monte Carlo simulation of photon transport and detection in deep ice: muons and cascades. In Spiering [145], pages 174–185.

[97] Karle, A. *et al.*, Analog optical transmission of fast photomultiplier pulses over distances of 2-km. *Nucl. Instrum. Meth.* **A387**:274 (1997).

[98] Knuteson, B., Miettinen, H. and Holmstrom, L., alphaPDE: A New Multivariate Technique for Parameter Estimation. *Comput. Phys. Commun.* **145**:351 (2002).

[99] Konopelko, A., The TeV spectrum of Mkn 501 as measured during the high state in 1997 by the HEGRA stereoscopic system of imaging air Cerenkov telescopes. *Astropart. Phys.* **11**:135 (1999).

[100] Kowalski, M., *On the Reconstruction of Cascade-Like Events in the AMANDA Detector*. Diploma thesis, Humboldt-Universität zu Berlin, Berlin, Germany (1999). URL `http://area51.berkeley.edu/manuscripts/`

[101] Kowalski, M., Cascade analysis for AMANDA-II. In *Proc. of AMANDA meeting*, Mainz (2001).

[102] Kowalski, M., Tracing tau-neutrinos from WIMP annihilation. *Phys. Lett.* **B511**:119 (2001).

[103] Kowalski, M., On the Light Yield of Hadronic and Electro-Magnetic Casacdes. AMANDA Internal Report 20020803 (2002), unpublished.

[104] Kowalski, M. and Gazizov, A., High Energy Neutrino Generator for Neutrino Telescopes. In Kajita *et al.* [93], pages 1459–1462.

[105] Kowalski, M., Ringwald, A. and Tu, H., Black holes at neutrino telescopes. *Phys. Lett.* **B529**:1 (2002).

[106] Kravchenko, I. and the RICE Collaboration, Updated Limits on the Ultra-High-Energy Neutrino Flux from the Rice Experiment at the South Pole. In Kajita *et al.* [93], pages 1337–1340.

[107] Krennrich, F. *et al.*, Cutoff in the TeV energy spectrum of Markarian 421 during strong flares in 2001. *Astrophys. J.* **560**:L45 (2001).

[108] Kutak, K. and Kwiecinski, J., Screening effects in the ultrahigh energy neutrino interactions. (2003), hep-ph/0303209.

[109] Lai, H. L. *et al.*, Global QCD analysis of parton structure of the nucleon: CTEQ5 parton distributions. *Eur. Phys. J.* **C12**:375 (2000).

[110] Learned, J. G. and Mannheim, K., High-Energy Neutrino Astrophysics. *Ann. Rev. Nucl. Part. Sci.* **50**:679 (2000).

[111] Learned, J. G. and Pakvasa, S., Detecting tau-neutrino oscillations at PeV energies. *Astropart. Phys.* **3**:267 (1995).

[112] Leuthold, M. J., *Search for Cosmic High Energy Neutrinos with the AMANDA-B10 Detector*. Ph.D. thesis, Humboldt-Universität zu Berlin, Berlin, Germany (2001).

[113] Lipari, P., Lepton spectra in the earth's atmosphere. *Astropart. Phys.* **1**(2):195 (1993).

[114] Lohmann, W., Kopp, R. and Voss, R., Energy Loss of Muons in the Range 1 – 10000 GeV. CERN yellow report 85-03, CERN, Geneva, Switzerland (1985).

[115] Mannheim, K., γ-rays and neutrinos from a powerful cosmic accelerator. *Phys. Rev.* **D48**:2408 (1993).

[116] Mannheim, K., High-energy neutrinos from extragalactic jets. *Astropart. Phys.* **3**:295 (1995).

[117] Mannheim, K., Protheroe, R. J. and Rachen, J. P., On the cosmic ray bound for models of extragalactic neutrino production. *Phys. Rev.* **D63**:023003 (2001).

[118] Martino, J., Ice Properties and Individual OM Sensitivities Using Atmospheric Muons. In *Proc. of AMANDA meeting*, Madison (2003).

[119] Maurin, D. *et al.*, Cosmic Rays below Z=30 in a diffusion model: new constraints on propagation parameters. *Astrophys. J.* **555**:585 (2001).

[120] Meszaros, P. and Rees, M. J., Relativistic fireballs and their impact on external matter - Models for cosmological gamma-ray bursts. *Astrophys. J.* **405**(1):278 (1993).

[121] Miocinovic, P., *Muon energy reconstruction in the Antarctic Muon and Neutrino Detector Array (AMANDA)*. Ph.D. thesis, Berkeley University, Berkeley, USA (2001). URL `http://area51.berkeley.edu/manuscripts/`

[122] Montaruli, T. *et al.*, ANTARES status report. In Kajita *et al.* [93], pages 1357–1360.

[123] Morris, D. A. and Ringwald, A., Astrophysical searches for exotic phenomena in ultrahigh- energy neutrino - nucleon scattering. (1994), hep-ph/9403214.

[124] Muecke, A. *et al.*, BL Lac objects in the synchrotron proton blazar model. *Astropart. Phys.* **18**:593 (2003).

[125] Nagano, M. and Watson, A., Observations and implications of the ultrahigh-energy cosmic rays. *Rev. Mod. Phys.* **72**:689 (2000).

[126] Naumov, V. A., Atmospheric muons and neutrinos. (2002), hep-ph/0201310.

[127] Neronov, A. *et al.*, Large scale extragalactic jets powered by very high-energy gamma rays. *Phys. Rev. Lett.* **89**:051101 (2002).

[128] Olbrechts, P. and Wiebusch, C. H. V., On the angular sensitivity of optical modules in ice. AMANDA Internal Report 20010102 (2001), unpublished.

[129] Pandel, D., *Bestimmung von Wasser- und Detektorparametern und Rekonstruction von Myonen bis 100 TeV mit dem Baikal-Neutrinoteleskop NT-72*. Diploma thesis, Humboldt-Universität zu Berlin, Berlin, Germany (1996), unpublished.

[130] PDG, Review of Particle Properties. *Euro. Phys. J. C* **3**(1-4):70 (2000).

[131] Pendleton, G. *et al.*, BATSE Observation of the Large-Scale Isotropy of Gamma-Ray Bursts. *Astrophys. J.* **464**:606 (1996).

[132] Pontecorvo, B., Mesonium and antimesonium. *Sov. Phys. JETP* **6**:429 (1957).

[133] Price, P. B., Kinetics of Conversion of Air Bubbles to Air Hydrate Crystals in Antarctic Ice. *Science* **267**:1802 (1995).

[134] Protheroe, R. J., Astrophysical sources of high energy neutrinos. (1996), astro-ph/9612213.

[135] Protheroe, R. J. and Johnson, P. A., Propagation of ultrahigh-energy protons over cosmological distances and implications for topological defect models. *Astropart. Phys.* **4**:253 (1996).

[136] Quinn, J. *et al.*, Detection of gamma-rays with E > 300-GeV from Markarian 501. *Astrophys. J.* **456**:L83 (1996).

[137] Rachen, J. P. and Meszaros, P., Photohadronic neutrinos from transients in astrophysical sources. *Phys. Rev.* **D58**:123005 (1998).

[138] Rhode, W. and Carloganu, C., Muon propagation in water and ice: Overview of various algorithms. In Spiering [145], pages 247–261.

[139] Rhode, W. *et al.*, Limits on the flux of very high-energetic neutrinos with the Frejus detector. *Astropart. Phys.* **4**:217 (1996).

[140] Ribordy, M., AMANDA-II/2000 data statistics, OM selection and retriggering procedure. *AMANDA Internal Report* (20020601) (2002), unpublished.

[141] Sambruna, R. M. *et al.*, Correlated intense X-ray and TeV activity of Mrk 501 in 1998 June. (2000), astro-ph/0002215.

[142] Schmidt, T., *Aufbau und Funtionsnachweis eines Optischen Moduls mit optisch-analoger Pulsübertragung für den AMANDA-II- und ICECUBE-Detektor*. Ph.D. thesis, Humboldt-Universität zu Berlin, Berlin, Germany (2002).

[143] Sigl, G., Ultrahigh-energy cosmic rays: A probe of physics and astrophysics at extreme energies. *Science* **291**:73 (2001).

[144] Sjöstrand, T. *et al.*, High-energy-physics event generation with PYTHIA 6.1. *Computer Physics Communications* **135**(2):238 (2001).

[145] Spiering, C., editor, *Simulation and Analysis Methods for Large Neutrino Telescopes*, DESY-Proc-1999-01, DESY Zeuthen, Germany (1999).

[146] Spiering, C., High energy neutrino astronomy: The experimental road. *J. Phys.* **G29**:843 (2003).

[147] Sreekumar, P. *et al.*, EGRET observations of the extragalactic gamma ray emission. *Astrophys. J.* **494**:523 (1998).

[148] Stecker, F. W. and Salamon, M. H., High Energy Neutrinos from Quasars. *Space Science Reviews* **75**:341 (1996).

[149] Stecker, F. W. *et al.*, High-energy neutrinos from active galactic nuclei. *Phys. Rev. Lett.* **66**:2697 (1991), erratum published in [150].

[150] Stecker, F. W. *et al.*, Erratum: High-energy neutrinos from active galactic nuclei. *Phys. Rev. Lett.* **69**(18):2738 (1992), erratum to [149].

[151] Steffen, P., The CORAMA program.
URL `http://www-zeuthen.desy.de/$\sim$steffenp/`

[152] Sudhoff, P., Transmission measurements with Amanda Glass and Evaluation for IceCube. *AMANDA Internal Report* (20010701) (2001), unpublished.

[153] Sveshnikova, L. G., The knee in galactic cosmic ray spectrum and variety in supernovae. (2003), astro-ph/0303159.

[154] Szabo, A. P. and Protheroe, R. J., The intensity of high energy neutrinos from unresolved active galactic nuclei. In Y. Suzuki, K. N., editor, *International Symposium on Neutrino Astrophysics*, pages 335–340, Takayama, Japan (1992).

[155] Taboada, I., *Search for high-energy neutrino induced cascades with the AMANDA-B10 detector*. Ph.D. thesis, Pennsylvania University, Pennsylvania, USA (2002).
URL `http://area51.berkeley.edu/manuscripts/`

[156] Towers, S., Kernel probability density estimation methods. In Whalley, M. and Lyons, L., editors, *Advanced statistical techniques in particle physics*, pages 112–115, Durham, England (2002).

[157] Tzamarias, S. E., NESTOR: A deep-sea neutrino telescope. *Nucl. Instrum. Meth.* **A502**:150 (2003).

[158] University of Chicago, Astroparticle Physics at Chicago - Cosmic Ray Spectrum Picture (1997).
URL `http://astroparticle.uchicago.edu/cosmic_ray_spectrum_picture.htm`

[159] Urry, C. M. and Padovani, P., Unified Schemes for Radio-Loud Active Galactic Nuclei. *Publ. Astron. Soc. Pac.* **107**:803 (1995).

[160] Van Ginneken, A., Energy Loss and Angular Characteristics of High-Energy Electromagnetic Processes. *Nucl. Instrum. Meth.* **A251**:21 (1986).

[161] Volkova, L. V. *et al.*, Prompt Muon Production in Cosmic Rays. *Nuovo Cim.* **C10**:465 (1987).

[162] Wagner, W. *et al.*, New Capabilities of the AMANDA-II High Energy Neutrino Detector. In Kajita *et al.* [93], pages 1365–1368.

[163] Washburn, K. *et al.*, A Search for Astrophysical Neutrino Sources with the Super-Kamikande Detector. In Kajita *et al.* [93], pages 1285–1288.

[164] Waxman, E. and Bahcall, J. N., High energy neutrinos from cosmological gamma-ray burst fireballs. *Phys. Rev. Lett.* **78**:2292 (1997).

[165] Waxman, E. and Bahcall, J. N., High Energy Astrophysical Neutrinos: An Upper Bound. *Phys. Rev.* **D59**:023002 (1999).

[166] Weiler, T. J., Cosmic ray neutrino annihilation on relic neutrinos revisited: A mechanism for generating air showers above the Greisen-Zatsepin-Kuzmin cut-off. *Astropart. Phys.* **11**:303 (1999).

[167] Wiebel-Sooth, B., Biermann, P. L. and Meyer, H., Cosmic Rays VII. Individual element spectra: prediction and data. (1997), astro-ph/9709253.

[168] Wiebusch, C. H. V., *The detection of Faint Light in Deep Underwater Neutrino Telescopes*. Ph.D. thesis, Rheinisch Westfälische Technische Hochschule Aachen, Aachen, Germany (1995), PITHA 95/37.

[169] Wiebusch, C. H. V., Muon reconstruction with AMANDA. In Spiering [145], pages 302–316.

[170] Wiebusch, C. H. V. *et al.*, Muon Track Reconstruction in AMANDA. (2003), submitted to *Nucl. Instrum. Meth. A*.

[171] Wigmans, R., *Calorimetry: Energy measurement in particle physics*. Clarendon, Oxford, UK, 1 edition (2000).

[172] Wischnewski, R., editor, *Methodical Aspects of Underwater/Ice Neutrino Telescopes*, DESY-PROC-2002-01, Hamburg, Germany (2001).

[173] Wischnewski, R. *et al.*, Results from the BAIKAL Neutrino Teleskope. In Kajita *et al.* [93], pages 1353–1356.

[174] Woschnagg, K. *et al.*, Optical Properties of South Pole Ice at Depths from 140 to 2300 Meters. In Kieda, D., Salamon, M. and Dingus, B., editors, *Proceedings of the* 26^{th} *International Cosmic Ray Conference*, volume 2, pages 200–203, Salt Lake City, USA (1999).

[175] Yoshida, S. and Teshima, M., Energy spectrum of ultrahigh-energy cosmic rays with extragalactic origin. *Prog. Theor. Phys.* **89**:833 (1993).

[176] Zas, E., Halzen, F. and Stanev, T., Electromagnetic pulses from high-energy showers: Implications for neutrino detection. *Phys. Rev.* **D45**:362 (1992).

[177] Zas, E., Halzen, F. and Vazquez, R. A., High-energy neutrino astronomy: Horizontal air shower arrays versus underground detectors. *Astropart. Phys.* **1**:297 (1993).

[178] Zatsepin, G. T. and Kuzmin, V. A., Upper limit of the spectrum of cosmic rays. *JETP Lett.* **4**:78 (1966).

[179] Zdziarski, A. A., X-rays and soft gamma-rays from Seyferts, radio galaxies, and black-hole binaries. (1998), astro-ph/9812449.

Appendix A

Optimizing the background MC

The main background in the analysis presented here consists of atmospheric muons. However, simulation of a sufficiently large data set is, due to the large number of events accumulated during the year, a computationally intensive task. For this reason the simulation chain has been optimized, to allow generation of a sufficient statistics of atmospheric muon MC events.

A significant increase in simulation speed can be achieved when focusing on events of higher energies. For example, if one is mainly interested in the spectrum $\geq$1 TeV, one needs to run the detector simulation only for muon events, which have a secondary particle with energy $E_{\mathrm{secondary}} \gtrsim 500$ GeV. This reduces the number of events for which the detector response is simulated to less than 1 % of the initial value. However since the generation of atmospheric muons with CORSIKA is almost as computationally intensive as the simulation of the detector response, this does not immediately translates into a large increase of the simulation rate.

Therefore the simulation chain before the detector simulation needs optimization. CORSIKA allows to set the energy thresholds for primary cosmic rays, as well as secondary particle tracking. The energy distribution of secondary particles, muons and primary cosmic rays are shown in figure A.0.1, for atmospheric muon MC events, passing cut # 3. The left plot shows the energy distribution of the standard MC and the right shows the data after application of a cut on the reconstructed energy, $E_{\mathrm{reco}} > 1$ TeV.

By moving the energy threshold of the primary cosmic ray flux from E=800 GeV to E=3 TeV and by demanding that muons produced in the air shower have at least 1200 GeV instead of 400 GeV, only a small fraction of events with E_{reco} >1 TeV are lost. However, the time needed for simulation of the air shower is greatly reduced.

The optimization is described by a triplet of threshold energies, namely those of the secondary particles, the muons produced in the air shower and the primary cosmic rays. For the example above these are {500 GeV, 1.2 TeV, 3 TeV}. Figure A.0.2 (left) shows the distribution of reconstructed energies for the regular and optimized atmospheric muon MC simulation. The right plot shows the ratio of the two curves. It can be seen that above $E_{\mathrm{reco}} \gtrsim 1$ TeV, approximately 80 % survive the optimization cuts, and that this fraction does not change much with energy. The fluctuations in the distributions are due to the limited available statistics of 6.3 days atmospheric muon MC simulation.

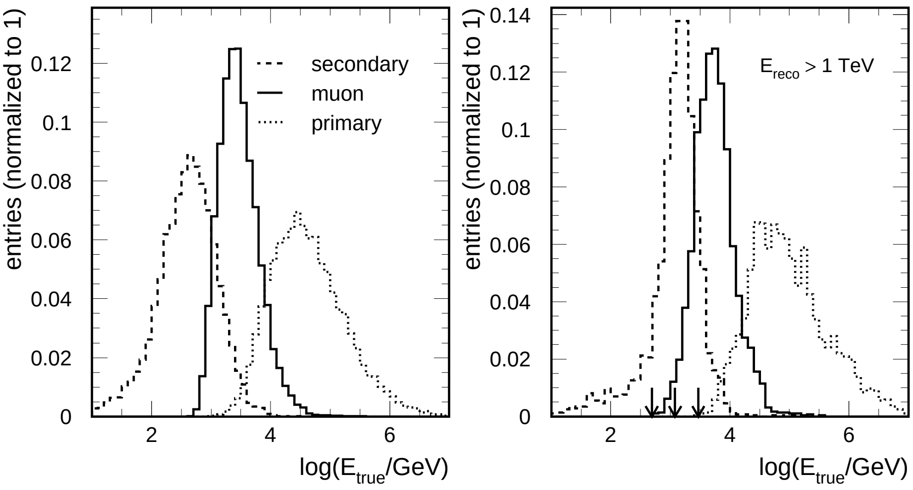

Figure A.0.1: Left: Energy distributions of secondary particles along the muon track, muons and primary cosmic rays, for events passing cut # 3. Right: an additional cut on the reconstructed energy of the event was applied, E_{reco} >1 TeV. The small arrows indicate the energy cuts chosen for optimization of the simulation chain.

The optimized simulation chain, which can only be used for the high energy part of the spectrum, is $\mathcal{O}(30)$ times faster than the regular MC simulation chain. It allowed to simulate 110 days of lifetime. Another atmospheric muon MC sample, was simulated using the settings {800 GeV, 3 TeV, 20 TeV }. This sample can only be used for reconstructed energies with $E_{\mathrm{reco}} \gtrsim 5$ TeV. An additional improvement in simulation speed of about a factor 3, allowed to generate an equivalent MC event statistics of 800 days of experimental data.

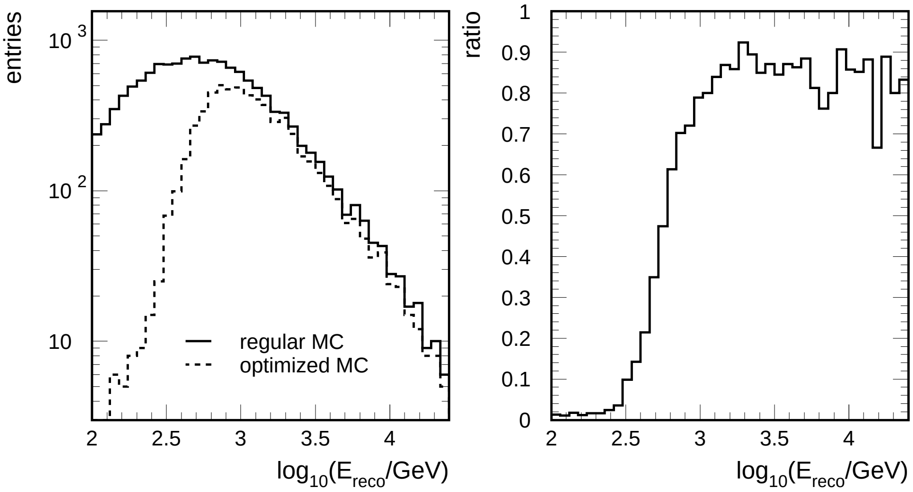

Figure A.0.2: Left: Distribution of reconstructed energies for the regular and optimized atmospheric muon MC simulation after cut # 3. Right: ratio of the two curves.

Appendix B

The COG-Z Problem

During analysis of AMANDA data one often encounters the so called COG-Z effect. The effect appears only in experimental data and consists of a triple peak structure in the distribution of the z-coordinate of the mean position of all hits (COG). This effect, becoming visible at a data reduction level of $\mathcal{O}(10^{-2})$, is only partially reproduced by the atmospheric muon background MC. As will be shown here, the near absence of the three peak structure in the MC simulation can be explained in terms of inaccurate modeling of the vertically changing ice properties (also called ice layers). A simple but physically motivated procedure for removing hits, after the simulation of the detector response by the program AMASIM, leads to the observable triple peak structure.

First, a brief review of the detector response simulation is necessary. Photon propagation tables are generated using the program PTD assuming constant absorption and scattering lengths. These tables tabularize photon arrival probabilities as a function of the emitter and receiver distance, orientation and direction. Vertically changing ice properties are only approximately simulated in AMASIM by choosing the photon propagation table corresponding to the ice properties of the location of the OM which response is simulated.

While such an implementation of vertical ice layers improves the agreement of MC simulation in many respect, it is nevertheless incomplete. This can be made clear by a simple example, illustrated in figure B.0.1. If a photon is emitted in a region of clear ice, and the receiving OM is located in another layer of clear ice, which however, is disconnected by the first through a layer of dusty ice, the arrival probability will be severely overestimated by the current MC simulation. This is due to the fact, that a configuration of emitter/receiver is simulated according to constant ice properties at the position of the receiver. Hence the dust layer in between has no influence on the result. The process of photons, passing through regions of large dust concentrations and reaching OMs in clear ice, will be called *tunneling*.

As described above, there are quite a few configurations of emitter/receivers for which the photon arrival probability is overestimated in the MC. The emitter can either be a secondary particle radiated by the muon or the muon itself. For each simulated hit, the parent particle contributing most photons is stored in the hit record. The information about other contributing particles is not available posterior to the detector response simulation.

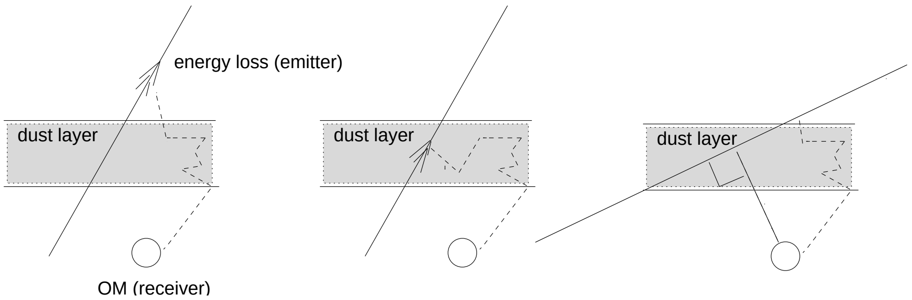

Figure B.0.1: Configurations of emitters (cascades or muons) and receivers (OMs) positions, which are presently not correctly simulated by AMASIM. The first two configurations correspond to an emitting cascade, while the third configuration illustrates an emitting muon track. See text for details.

To obtain an estimate of the impact of the photon tunneling effect, hits from the following configurations of emitter/receivers are removed from the event record:

- If the emitting secondary particle is above/below/within a dust layer and the receiver is below/above the dust layer, the hit is removed. These cases correspond to the first two diagrams of figure B.0.1.
- If the emitting particle is a muon, the position of the origin of the emittance is not well defined. Therefore the point of closest approach of the muon to the hit OM is assumed as the emitters location. Hits are removed under the same conditions as above. The case of a muon being the emitter is illustrated in the last diagram of figure B.0.1.

The borders of the 3 dustiest regions are taken according to the MAM-ice model and are: -140 m to -160 m, -10 to -40 and 90m to 170 m.

Figure B.0.2 shows the distribution of z_{COG} for experimental data and background MC simulation after cut # 3. The upper plot displays the distribution for the regular MC simulation used throughout the analysis, while the lower plot shows the MC simulation with additional removed hits , according to the prescription defined above. About 20 % of the hits where removed. As can be seen, the triple peak structure seen for the experimental data, can be qualitatively reproduced with the special background MC.

It is an interesting question, how the distributions of other variables compare. For most distributions, the differences between the special and the regular MC simulation is not very large. As an example, the distribution of the reconstructed zenith angle of the muon track is shown in figure B.0.3. The special MC simulation appears to describe the experimental data better in the region of wrongly reconstructed muon tracks, $cos(\theta) < 0$.

However, there is an important limitation concerning the applicability of the special MC simulation. The fraction of hits, which are removed due to the hit cleaning procedure, increases for higher energies. This is due to the fact, that for ~TeV energies the size of the events (see section 5.3) exceeds the average distance between the ice layers defined above. However, if a large fraction of hits of an event is removed, the event will be mis-reconstructed or mis-identified and rejected. A consequence is, that the energy spectrum

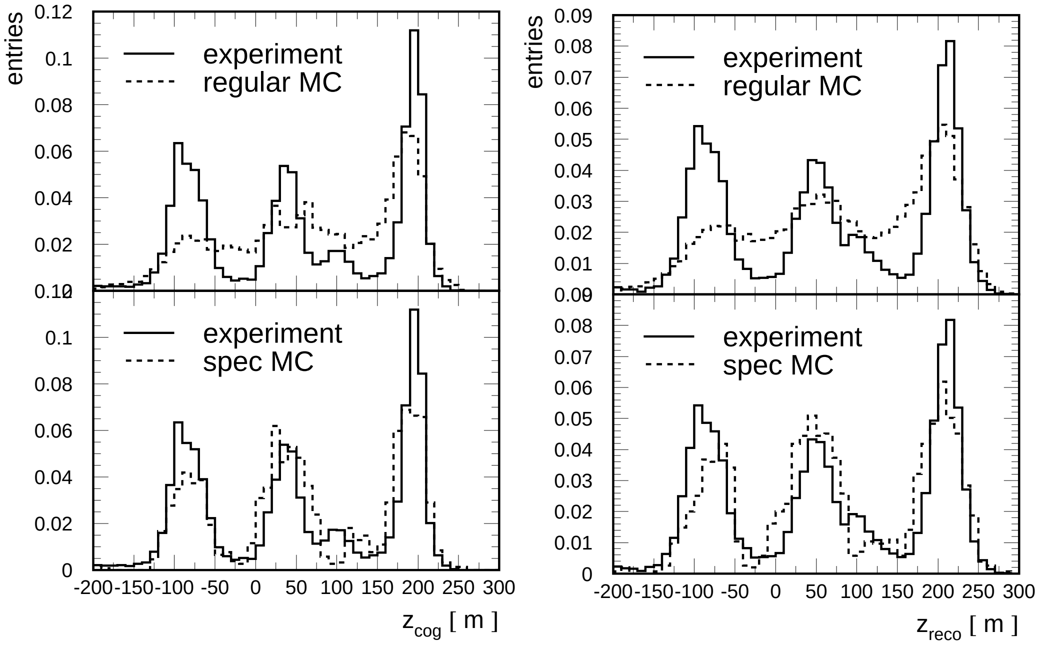

Figure B.0.2: Distribution of z-coordinate of center of gravity of all hits ($z_{\rm cog}$, left plot) and vertex reconstruction ($z_{\rm reco}$, right plot). The top figures show experimental data compared to the regular background MC simulation, while the lower plots show the special MC simulation, with tunneling hits removed. The events shown have passed cut # 3.

of simulated atmospheric muons is significantly steeper than observed in the experiment. For this reason, the MC simulation presented here, is not used further in the analysis presented in this dissertation.

The criteria for removing hits described above are certainly too strict, as they apply only for the case of totally absorbing ice layers. In reality, there is a non-negligible probability for photons to *tunnel* through dusty layers of ice. Unfortunately, the information given in the event record posterior to the detector response simulation does not permit a significantly more realistic extension of the method described above. However, the results shown here provide additional motivation for implementation of an exact simulation of photon transport through ice with vertically changing optical properties. A realistic simulation of photon propagation can be done with the PHOTONICS program [121]. It generates tables containing photon arrival probabilities for a range of different emitter and receiver positions and orientations. Due to the largeness of the parameter space, already reduced versions of these tables have a total size of $\mathcal{O}(1)$ Gigabytes. Integration of these tables into the detector simulation of AMANDA is forseen.

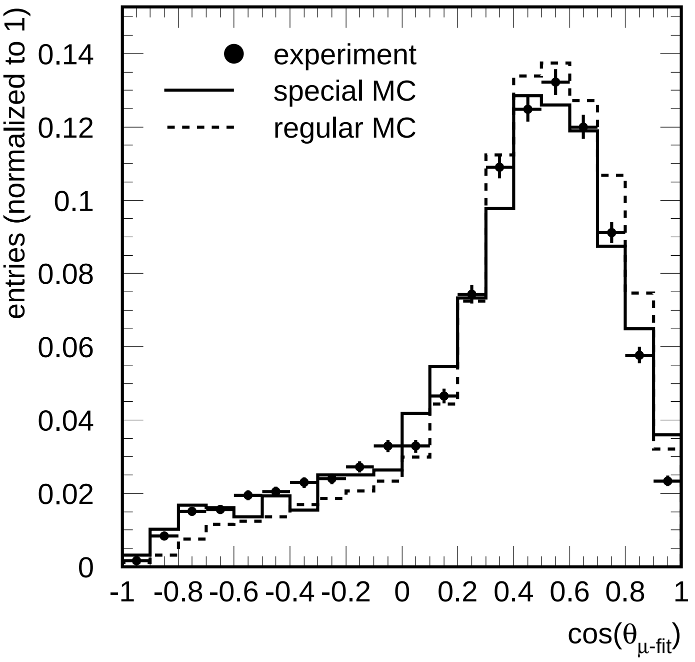

Figure B.0.3: Distribution of the cosine of the zenith angle resulting from the muon track fit. The data has passed cut # 3.

Appendix C

Bayesian Discriminant

Discrimination between a class of signal (s) and background (b) events is optimal for a given set of observables ($\vec{x}$) if the probability:

$$P(s|\vec{x}) = \frac{P(s)P(\vec{x}|s)}{P(s)P(\vec{x}|s) + P(b)P(\vec{x}|b)},$$

is used as the discriminating variable (see section 7.4.2 for an explanation of $P(s|\vec{x})$, $P(s)$, $P(b)$, $P(\vec{x}|s)$ and $P(\vec{x}|b)$).

The discrimination potential can be characterized by the fraction of events (ε) passing a cut, $P(s|\vec{x}) > P_{cut}$:

$$\varepsilon_\mathrm{s} = \int\limits_{P(s|\vec{x}) \geq P_{cut}} P(\vec{x}|s)\mathrm{d}\vec{x}; \qquad \varepsilon_\mathrm{b} = \int\limits_{P(s|\vec{x}) \geq P_{cut}} P(\vec{x}|b)\mathrm{d}\vec{x} \tag{C.0.1}$$

What will be shown next, is that the discrimination potential is independent of the choice of the (e.g. unknown) prior probabilities $P(s)$ and $P(b)$. By changing to a different set of priors, one can readjust the cut value P_{cut} such that ε_s and ε_b are left unchanged.

Without loss of generality, one can chose the original priors to be $P(s) = P(b) = 0.5$ and obtain a new set of prior density probabilities by weighting the original ones with $0 \leq c \leq 2$:

$$P(s)' = c \cdot P(s); \quad P(b)' = (2-c) \cdot P(b).$$

The resulting $P(s|\vec{x})'$ can be obtained from the original $P(s|\vec{x})$ by:

$$P(s|\vec{x})' = \frac{cP(\vec{x}|s)}{cP(\vec{x}|s) + (2-c)P(\vec{x}|b)} = \frac{1}{1 + \frac{P(\vec{x}|b)}{P(\vec{x}|s)}\frac{2-c}{c}} = \frac{1}{1 + (\frac{1}{P(s|\vec{x})} - 1)\frac{2-c}{c}}.$$

The important feature is that $P(s|\vec{x})'$ is a strictly monotonic function of $P(s|\vec{x})$ and not explicitly dependent on $P(\vec{x}|s)$ and $P(\vec{x}|b)$. Hence, for any cut $P(s|\vec{x}) > P_{cut}$, one finds a new cut $P(s|\vec{x})' > P'_{cut}$, for which ε_s and ε_b are left unchanged and the sample of events passing the cuts are identical. One consequence of this is that when optimizing the cut value the assumed signal strength has no influence on the final result.

Appendix D

The Remaining Experimental Event

One event of the data sample of the year 2000 passed all selection criteria of this analysis. The event appeared on day 170 at 16:37:38 UTC. Its reconstructed vertex coordinates and energy are $\{x,y,z,E\} = \{47.8\ \mathrm{m}, 4.1\ \mathrm{m}, -35.3\ \mathrm{m}, 132\ \mathrm{TeV}\}$.

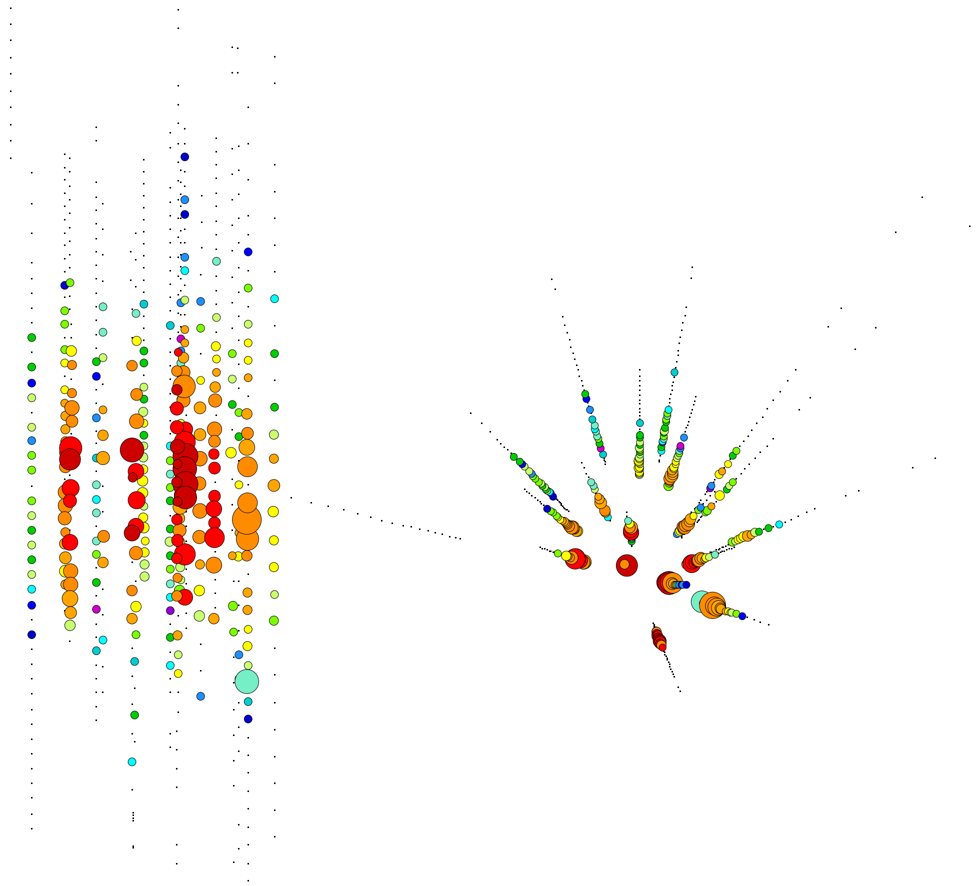

Figure D.0.1: The remaining event is displayed from the side and from above. Colored circles represent hits (early hits are red, late hits are blue). Larger circles represent larger registered amplitudes.

Appendix E

Data Processing

The data processing was done with a chain of different programs and command options, which are summarized below. A documentation of the various programs and options can be found in [13].

E.1 Preprocessing

`Program`	command line	comments
`reader`	–use-config=Db/detector.money.1_corr.cnf	data conversion
`deff`	-v -Y -y N=3 ...	bad OM removal
`deff`	-Y -y b=75:2000:1:307 ...	TOT window cut
`soff`	-v -e100	multiplicity trigger
`amacalib`	-v -D ./Db/vmecal.db	VME calibarion
`soff`	-v -O 24:2500 -y u=9 -y u=10	software trigger
`deff`	-v -P 22875:2000:8000:all	time window cut
`amacalib`	-Z	de-calibration
`amacalib`	-v -Aa -y 0:20975 -D ./Db/omdb-00-20010926.amacalib.txt -z	full calibration
`deff`	-v -D -19000	time shift
`deff`	-Y -y R=-2000:4500	time window cut
`deff`	-v -Y -y u=9 -y u=10 -y u=11 -y a=0.1:1000 -y I=100.:500.:1	further hit cleaning

E.2 Event Reconstruction and Filter

`Program`	Command Line	Comments
`recoos`	-v -rn -ik -p p=e- -X g=n -pw=1. -X s=n -y u=12 -y f=1:10 -p n=1000:5000 -p j=15 -p a=96. -p t=1:5 -X o=2	*c_first* reco.
`muff` `muff`	-v -Z rchi2(1)<0.05 -v -Z prob(1)>8	first level filter
`recoos`	-v -rn -im -X g=f -pw=0. -X s=o -y u=12 -y I=70.:500.:1 -y A=1 -p t=1:4 -y f=1:10 -p n=1000:5000 -p j=15 -p a=96. -p t=1:5 -X o=2	unused reco.
`recoos`	-v -rn -ii -p p=e- -X g=f -pw=1. -X s=n -y u=12 -y f=1:10 -p n=1000:5000 -p j=15 -p a=96. -p t=1:5 -X o=2	unused reco.
`deff`	-r 3 ...	bad OM removal
`amacalib`	-v -Z	de-calibration
`xt-filt`	-v -a87:302 -t20 -p20 -m -d -f 40. -b Db/adc_tot_2000-20020524.fit	cross-talk filter
`amacalib`	-v -G -D Db/omdb-00-20010926.amacalib.txt	full calibration
`recoos`	-v -mp -p m=0 -rm -m x -rm -if -p f=3 -p p=e- -X g=n -X s=n -z a_pp_upandel -p t=0:0 -l xyzt -x x:step=20,y:step=20,z:step=20, time:step=200 -y A=1 -y f=1:10 -y u=12 -y u=13 -p n=1000:5000 -p j=15 -p a=96. -p t=1:5 -X o=2	1-pe vertex fit
`recoos`	-v -mp -p m=0 -rm -m x -rm -if -p f=4 -p p=e- -X g=n -X s=n -z a_upandel_ps_mpe -p t=0:0 -l xyzt -x x:step=20,y:step=20,z:step=20, time:step=200 -y A=1 -y f=1:10 -y u=12 -y u=13 -p n=1000:5000 -p j=15 -p a=96. -p t=1:5 -X o=2	mpe vertex fit
`muff`	-v -Z rchi2(5)<7.1	cut on likelihood
`recoos`	-v -m x -rg -p M=16 -p L=0. -if -X g=n -X s=c -z a_upandel -p f=2 -l xyzza -x x:step=40,y:step=40,z:step=40,zenith:step=0.1, azimuth:step=0.2 -y A=1 -y f=1:10 -y u=12 -y u=13 -p n=1000:5000 -p j=15 -p a=96. -p t=1:5 -X o=2	16-iteration track fit
`recoos`	-mp -p m=0 -rm -if -X g=n -X s=n -z a_pp_phpnh_f -p p=e- -p f=5 -l energy -p t=0:0 -x energy	energy fit (isotropic)
`recoos`	-mp -p m=0 -rm -if -y A=1 -X g=n -X s=n -z a_pp_phpnh_ig -p p=e- -p f=5 -x energy,zenith,azimuth -p t=0:0 -l energy,za -p m=0 -p M=5	energy fit (with direction)
`recoos`	-v -m x -rm -if -p f=4 -p p=e- -X g=n -X s=n -z a_upandel_ps_mpe -p t=0:0 -l xyzt -x x:step=20,y:step=20,z:step=20,time:step=200 -mp -p m=0 -rm -p n=1000:5000 -p j=15 -p a=96. -p t=1:5 -X o=2 -y A=1 -y f=1:10 -y u=12 -y u=13 -y q=4:60	mpe vertex fit without hits in 60 m radius

Acknowledgment

I would like to take the opportunity to thank all the people who supported me during my Ph.D. studies. First I would like to thank Prof. Thomas Lohse for taking the responsibility for this thesis. It is a pleasure to thank Dr. Christian Spiering who gave me the opportunities to work within the AMANDA group of DESY Zeuthen. His regular advice and support as well as the freedom received when setting priorities has motivated me throughout the years.

I want to thank the members of the AMANDA group for much support related to this work. I have benefited from numerous fruitful discussions and advice concerning both physics and technical issues. I feel strong ties to all my co-graduate-students: thanks go to Markus Ackerman, Sebastian Böser, Tonio Hauschild and Henrike Wissing for creating a very pleasant working atmosphere. Dr. Peter Steffen deserves a special thanks, for donating the Espresso machine. The boost in productivity easily compensates for the time spend in coffee conversations. I want to thank those who have been involved in proof-reading this thesis: Dr. Elisa Bernardini, Dr. David Boersma, Dr. Rolf Nahnhauer, Dr. Stefan Schlenstedt, Dr. Christian Spiering, Jutta Stegmeier and Michael Unger.

It want to thank all the members of the AMANDA collaboration. I have enjoyed numerous stimulating discussions with Prof. Steve Barwick, Dr. Tyce DeYoung, Dr. Paolo Desiati, Lisa Gerhard, Prof. Allan Hallgren, Prof. Francis Halzen, Dr. Gary Hill, Dr. Stephan Hundertmark, Prof. Albrecht Karle, Till Neunhöffer, Prof. Lutz Köpke, Dr. Kathrine Rawlins and Dr. Kurt Woschnagg. Additionally I want to thank those few believers who have worked in the field of cascades for a fruitful collaboration: Prof. Doug Cowen, Dr. Kael Hanson, Prof. Ignacio Taboada and Dr. Christopher Wiebusch. May this list be growing!

I am grateful to Prof. Tom Gaisser, for giving me the opportunity for a research visit at the Bartol Research Institute. The pleasant atmosphere at Bartol provided by Dr. Ralph Engel, Prof. Tom Gaisser, Prof. David Seckel and Prof. Todor Stanev has been very stimulating. Additional thanks go to Dr. Andreas Ringwald and Huitzu Tu for a fruitful collaboration.

I am thankful to my parents for their love and support. And finally I express my gratitude and devotion to Eva Vogt - I owe her much.

Selbständigkeitserklärung

Hiermit erkläre ich, die vorliegende Arbeit selbständig ohne fremde Hilfe verfaßt und nur die angegebene Literatur und Hilfsmittel verwendet zu haben. Ich habe mich anderwärts nicht um einen Doktorgrad beworben und besitze einen entsprechenden Doktorgrad nicht. Ich erkläre die Kenntnisnahme der dem Verfahren zugrunde liegenden Promotionsordnung der Mathematisch-Naturwissenschaftlichen Fakultät I der Humboldt-Universität zu Berlin.

Marek Paul Kowalski

Berlin, den 15. Oktober 2003

Lebenslauf

Name:	Marek Paul Kowalski
Geburtstag und -ort:	23. Mai 1974 in Bonn

Schulbildung

9/1980 - 7/1984	Gorch-Fock Grundschule, Hamburg
9/1985 - 7/1986	Realschule Iserbarg, Hamburg
9/1986 - 7/1994	Gymnasium Blankenese, Hamburg Schulabschluss: Abitur

Ersatzdienst

9/1994 - 1/2000	Freiwillige Feuerwehr in Hamburg und Berlin

Studium

10/1994 - 9/1996	Studium an der Universität Hamburg Abschluss: Vordiplom in Physik, “sehr gut”
10/1996 - 9/1998	Hauptstudium an der Humboldt-Universität zu Berlin
10/1998 - 9/1999	Diplomarbeit am DESY Zeuthen; Titel: “On the Reconstruction of Cascade-Like Events in the AMANDA Detector”
9/1999	Studienabschluss: Diplom in Physik, “sehr gut”
1/2000 - 9/2003	Wissenschaftlicher Mitarbeiter am DESY Zeuthen
3/2000 - 8/2000	Studienaufenthalt am Bartol Research Institute, Newark, USA

List of Publications

Refereed Journals
(† indicating principal authorship and/or direct participation in the published work)

1. Ahrens, J. *et al.* (AMANDA collaboration), Limits on Diffuse Fluxes of High Energy Extraterrestrial Neutrinos with the AMANDA-B10 Detector, *Phys. Rev. Lett.* **90**, 251101 (2003).
2. Ahrens, J. *et al.* (AMANDA collaboration), Search for Point Sources of High-Energy Neutrinos with AMANDA, *Astrophys. J.* **583**, 1040 (2003).
3. † Ahrens, J. *et al.* (AMANDA collaboration), Search for Neutrino-Induced Cascades with the AMANDA Detector, *Phys. Rev.* **D 67,** 012003 (2003).
4. † Kowalski, M., Ringwald, A. and Tu, H., Black Holes at Neutrino Telescopes, *Phys. Lett.* **B 529**, 1 (2002).
5. Ahrens, J. *et al.* (AMANDA collaboration), Limits to the Muon Flux from WIMP Annihilation in the Center of the Earth, *Phys. Rev.* **D 66**, 032006 (2002).
6. Ahrens J. *et al.* (AMANDA collaboration), Observation of High-Energy Atmospheric Neutrinos with the Antarctic Muon and Neutrino Detector Array, *Phys. Rev.* **D 66**, 012005 (2002).
7. Andres, E. *et al.* (AMANDA collaboration), Search for Supernova Bursts with the AMANDA Detector, *Astroparticle Physics* **16**, 345 (2001).
8. † Kowalski, M., Tracing Tau Neutrinos from WIMP Annihilation, *Phys. Lett.* **B 511**, 119 (2001).
9. Andres, E. *et al.* (AMANDA collaboration), Observation of High-Energy Neutrinos using Cherenkov Detectors Embedded Deep in Antarctic Ice, *Nature* **410**, 6827 (2001).
10. Andres, E. *et al.* (AMANDA collaboration), The AMANDA Neutrino Telescope: Principle of Operation and First Results, *Astroparticle Physics* **13**, 1 (2000).

Conference Proceedings (selected)

1. Kowalski, M. *et al.* (AMANDA collaboration), Search for High Energy Neutrinos of All Flavors with AMANDA-II, in [93], pages 1301-1304.

2. Kowalski, M. and Gazizov, A., High Energy Neutrino Generator for Neutrino Telescopes, in [93], pages 1459-1462.

3. Kowalski, M. *et al.* (AMANDA collaboration), Search for Exotic Particles with AMANDA, to appear in the proceedings of Physics in Collision, Zeuthen, Germany (2003).

4. Kowalski, M. *et al.* (AMANDA collaboration), Search for Neutrino-Induced Cascades with the AMANDA-II Detector, in proceedings of the Neutrino 2002 conference, Munich, Germany, ed. F. von Feilitzsch and N. Schmitz., *Nuclear Physics B (Proc. Suppl.)* 118 (2003), page 513.

5. Kowalski, M. and Taboada, I., Cascade Reconstruction in AMANDA, in [172], pages 135-140.

6. Taboada, I., Kowalski, M. *et al.* (AMANDA collaboration), Search for Cascade-Like Events in the AMANDA-B10 Detector , in [78], HE 232, pages 1117-1120.

7. Kowalski, M. *et al.* (AMANDA collaboration), Physics Results from the AMANDA Neutrino Detector, in proceedings of the EPS International Conference on High Energy Physics, Budapest, Hungary (2001), ed. Horvath, D., Levai, P. and Patkos, A., *JHEP Proc. Section*, PrHEP-hep2001/207.